Inversed Open Granular Filters in Land Reclamation Structures

Modeling of the Interface Stability

G.F. (Floris) Boersma

Technische Universiteit Delft

Inversed Open Granular Filters in Land Reclamation Structures

Modeling of the Interface Stability

by

G.F. (Floris) Boersma

to obtain the degree of Master of Science
at the Delft University of Technology,
to be defended publicly on Thursday September 3, 2020 at 03:00 PM.

Student number:	4164326	
Project duration:	November 1, 2019 – September 3, 2020	
Thesis committee:	Dr. ir. B. Hofland	TU Delft, Supervisor, Chair
	Dr. ir. A. Antonini	TU Delft
	ir. G.M. Smith	TU Delft & Van Oord
	ir. D.C.P. van Kester	Van Oord, Daily supervisor

An electronic version of this thesis is available at `http://repository.tudelft.nl/`.

TU Delft Van Oord

Preface

This thesis report is written to conclude the master Hydraulic Engineering at the faculty Civil Engineering and Geo-sciences of Delft University of Technology (TU Delft). The study had a lead time of 10 months, from November 2019 till September 2020 and focused on the stability of inversed open granular filters in land reclamation structures. Both the TU Delft and Van Oord Dredging and Marine Contractors (Van Oord) supervised the project.

My sincere gratitude goes out to my thesis committee for their guidance and flexibility during unusual times. Bas Hofland for the confidence to invest a "small car" on the new physical model, Alessandro Antonini for the sharp remarks at the end of every virtual meeting, Greg Smith for – besides sharing his expertise – improving my English writing skills, and my daily supervisor Dennis van Kester for his enthusiastic and pragmatic guidance.

Next to my committee, I would like to thank Van Oord for the opportunity to get to know the company during this study. I also would like to thank the people at the Hydraulic Engineering Laboratory and DEMO for their assistance.

Finally, I want to thank my family and friends for the unconditional support and encouragement to concentrate on my own interests.

G.F. (Floris) Boersma
Rotterdam, August 2020

Abstract

This thesis is the third study of a research line that focuses on the interface stability of a rubble mound sand retaining structure. An schematic cross-section of such a land reclamation is shown in Figure 1. The type of interface considered in this study is a geometrically open granular filter (indicated in the same figure) because of its economical and constructional benefits.

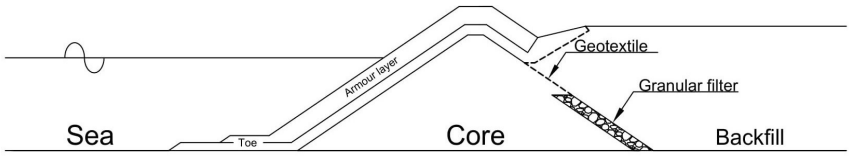

Figure 1: An example of a rubble mound sand retaining structure with geotextile and a granular open filter as interface between the core and backfill.

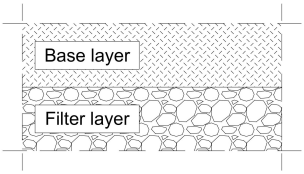

Figure 2: Horizontal leveled base-filter layer interface.

The stability of an open filter structure in which the base layer is located on top of the filter layer, as shown in Figure 2, was investigated by the use of physical modeling. The model used was the same waterproof elongated container as used by Van de Ven (2019), after some adjustments were made. Three compartments were allocated in this model, shown in Figure 3. In Compartment A, the water level was controlled by the use of a plunger. This caused water level differences between the compartments and therefore induced a hydraulic gradient (i) in the filter structure that was installed in Compartment B. The hydraulic gradient was considered as the main load parameter for erosion. The main strength parameter was the stability ratio (SR), defined as the sieve diameter for which 15% of the mass of the filter material is smaller divided by the sieve diameter for which 85% of the mass of the base material is smaller $\left(\frac{d_{15,f}}{d_{85,b}}\right)$. During testing, this hydraulic gradient was increased by the plunger until erosion was noted, defining the critical hydraulic gradient (i_{cr}) for the filter-base combination tested.

Two loading conditions were distinguished, namely the parallel and combined set-up, as shown in Figure 3. Besides the SR and these loading conditions, the influence of the characteristic grain size of the base material and the filter layer height on i_{cr} was studied.

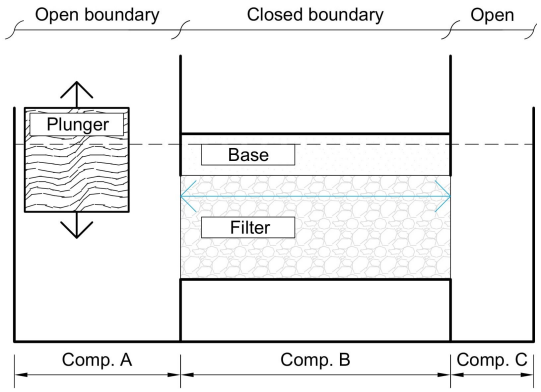

(a) Parallel configuration.

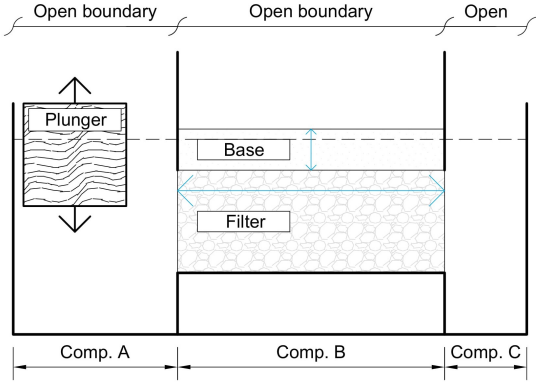

(b) Combined configuration.

Figure 3: A schematic representation of the loading conditions with corresponding open and closed model boundaries. The flow and hydraulic gradient orientation are illustrated in blue.

During this thesis, a new phenomenon influencing the i_{cr} was observed, which was not included in the research line yet. This was the initial sand saturation of the filter layer. Therefore, the physical model results were split up into unsaturated and partly saturated tests, shown in Figure 4. For the unsaturated parallel configuration, SR = 5.7, 6.7, 12.9 and 13.1 were tested. Results were found for the upper two values, $i_{\parallel,cr,SR=12.9}$ = 0.051 and $i_{\parallel,cr,SR=13.1}$ = 0.057. For the lower SR, no erosion was detected resulting in a bottom limit of i_{cr}. The partly saturated parallel tests resulted in a reduction of i_{cr} up to a minimum of 73%. Projecting this effect into reality could have a significant influence on the stability of an inversed open granular filter in land reclamation structures. However, further research is advised. All found i_{cr} in the parallel tests were higher compared to Van de Ven (2019). Besides, it was concluded that a larger characteristic grain size of the base layer and the filter layer thickness did not influence the i_{cr} significantly.

Furthermore, three unsaturated combined tests were conducted with SR = 6.7 and 12.9. No erosion was noted for SR = 6.7. Erosion was detected twice for SR = 12.9, once in the first test segment – resulting in an upper limit for (i_{cr}) – and once in the second test segment. The results of the combined tests are given in Figure 5 on the next page. The parallel component of the combined i_{cr} is also given in Figure 4. This figure shows a reduction of 93% for i_{cr} in the combined set-up compared to the unsaturated parallel set-up, implying that an additional load decreases the critical load for the considered filter structure. However, this could also be the results of model installation differences.

Lastly, a new physical model was designed and constructed to facilitate the study on the influence of the superimposed load and the filter inclination on the interface stability. A newly developed numerical model has been made to plot design graphs for this new model.

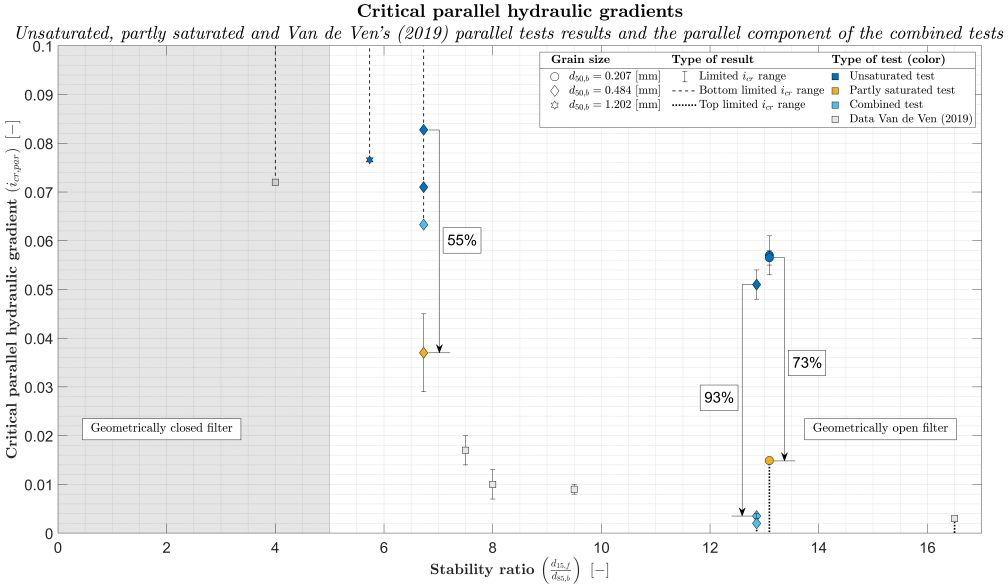

Figure 4: The results of the unsaturated and partly saturated parallel tests are plotted with the parallel component of the combined test results and the parallel test results of Van de Ven (2019).

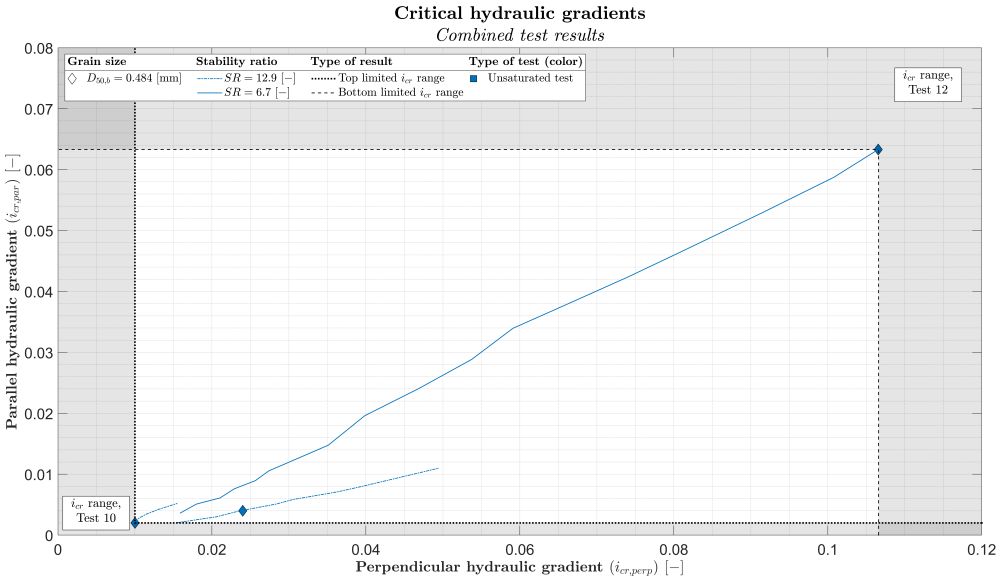

Figure 5: Parallel and perpendicular components of the hydraulic gradient in the combined tests. The markers indicate where erosion was first noted. Two different stability ratios were tested, one test did not result in erosion.

Contents

1

Introduction

Land reclamation projects are of all times. Around 500 B.C., Frisian settlements were built on artificial dwelling mounds. These terps, up to 15 meters high, gave protection against floods originating from sea and rivers. From the end of the medieval period, windmills were used to drain bodies of water and make the land suitable for development. With increasing technical development, it became possible to redraw a coastline. During the 1950's and 1960's, the Flevopolder and Noordoostpolder were drained, now forming the Dutch province Flevoland with a population of almost 450.000 (CBS, 2020). Nowadays, cities are extended to house a continuous growth of inhabitants (Figure 1.1a), harbors and airports are built in sea to maintain and strengthen economical positions (Figure 1.1b) and cities are transformed to attract tourists (Figure 1.1c).

(a) Malé, Maldives (source: Van Oord).

(b) Moín Container Terminal, Costa Rica (source: Van Oord).

(c) Palm Jumeirah, Dubai, United Arab Emirates (source: Van Oord).

Figure 1.1: Examples of land reclamation projects.

One way to create a land reclamation is to build a rubble mound breakwater and fill the lee side with sand. This hard rock structure forms the boundary between the sea and the backfill. Under wave attack, sand from the backfill may erode through the breakwater, leading to a settlement of the ground level. This is undesirable since it causes more maintenance work and could damage structures on top of the land reclamation. To reduce sand erosion through the breakwater, a filter is used between the sand and breakwater, as highlighted in blue in Figure 1.2. The focus of this study is on the filter in such a reclamation. In Paragraph 1.1, background information on filters is given.

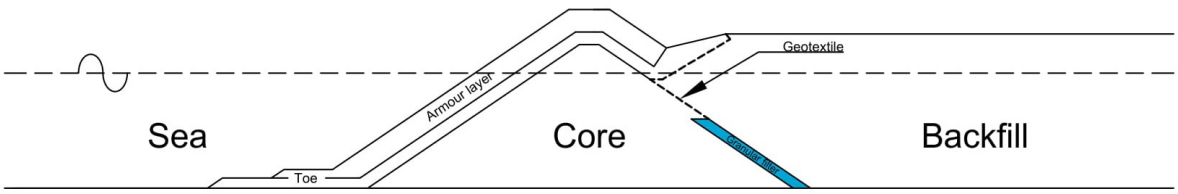

Figure 1.2: An example of a rubble mound sand retaining structure with geotextile and granular open filter. The granular filter is highlighted in blue.

1.1. Background information on filters

The main purpose of a filter is to prevent the washout of finer material due to hydraulic gradients. This means that the base material (the backfill in this study) should not pass through the pores of the adjacent layer. In order to do so, various possible types of filters can be applied. The most widely used are granular geometrically closed filters, granular geometrically open filters and geotextile filters. An example of a geotextile and granular filter combination with the corresponding base material, the backfill is given in Figure 1.3.

Granular filters consist of one or more layers of granular material of varying diameters. The design of a granular filter could be based on different criteria. Often it is based on the relation between the critical hydraulic gradient in the porous flow and a quotient of representative grain diameters (Schiereck and Verhagen, 2012). A distinction is made between geometrically closed, open and instable granular filters.

Geometrically closed filters ensure that no transport of base material is possible. This is because the size of the grains is determined such that the base material cannot physically pass through the grains of the filter. This often leads to a conservative design since there is no critical hydraulic gradient for the transition of the base and filter layer. Moreover, the placement of a closed filter is considered time consuming and expensive since it will consist of multiple layers, with every layer to have a minimum thickness (Schiereck and Verhagen, 2012).

A more economical design could be realized using a stable geometrically open filter, but hydrodynamically sand tight. In these type of filters, the grains of the filter layer are much larger than those of the base layer. This results in the possibility of base material to protrude into the filter layer. However, the hydraulic load is less than the threshold value for incipient motion. In other words, the hydraulic gradient in the structure is lower than the critical hydraulic gradient for erosion. The disadvantage, compared to the geometrically closed filter, is that detailed information on the loading gradients is necessary (Schiereck and Verhagen, 2012).

An instable geometrically open filter, or transport filter, is a filter where the hydraulic load is occasionally higher than the threshold value leading to even larger quotients of the filter and base material diameters. This filter could be applicable in a case where some loss of material is accepted within the limits of admissible settlements (Verheij et al. (2012) and Schiereck and Verhagen (2012)).

Furthermore, a geotextile could be applied on the interface to keep te base material in place. Because of the permeable characteristic of the fabric, no excessive water pressure is built up underneath a geotextile. Geotextiles come in sheets and rolls, resulting in inevitable transition areas. If an overlap of two adjacent geotextile fails, the whole filter structure is likely to fail. Therefore, a sound structure requires that close attention is being paid to the overlaps, especially if constructed under the water surface.

Besides these more traditional filters, almost unlimited combinations of granular material, geotextile, and reinforcements are available on the market. However, these specialized product are not economically attractive until used in very large quantities (Schiereck and Verhagen, 2012), which is considered not to be the case in this study.

1.2. Problem description

Open filters have both economical and construction benefits compared to other filter types, in particular when constructed at a certain depth. However, traditional literature mainly focus on open filter structure in which the filter layer is constructed on top of a base layer (usually sand), having gravity in their favor. An example of such a *standard* open filter is the bed protection of a storm surge barrier. In contrast to these open filters, the open filter considered in this study has the following characteristics:

- The base material is placed on top of the filter, resulting in an *inversed* open filter;
- The filter is inclined;
- A superimposed load exerts on the filter layer, resulting from the weight of the backfill material.

This study is part of a research line which focuses on the sand-core interface of rubble mound sand retaining structures, as illustrated in Figure 1.3. Tutein Nolthenius (2018) studied the shortening of a geotextile and the situation without a filter layer. That thesis justified the further exploration of abbreviating geotextiles at the considered interface. The thesis of Van de Ven (2019) focused on the erosion through an inversed geometrically open but hydraulically closed filter layer. The objective of that thesis is to determine whether or not it was possible to create a sand tight interface with the use of a single open filter layer. Van de Ven (2019) considered two flow directions, namely the parallel and perpendicular direction with respect to the filter interface, in accordance with De Graauw et al. (1983) (more information of the axis system is given in Paragraph 1.5). The pressure distribution inside a breakwater was determined in a numerical and empirical way in order to get an insight in the order of magnitude of the gradients. Afterwards, a physical model was used to determine the relationship between the stability ratio of a filter structure and the critical hydraulic gradients, shown in Figure 1.4.

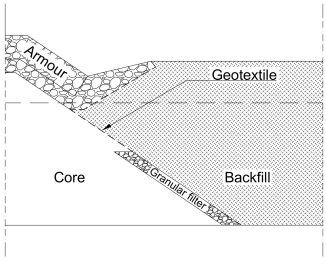

Figure 1.3: An example of a boundary between the breakwater and backfill. The upper part of the filter is constructed with geotextile, the lower part with an open granular filter layer. A granular filter is used at the lower part because the placement of a geotextile deeper than 5 meters is rather difficult and expensive. The focus of this study is on the stability of this inversed open granular filter.

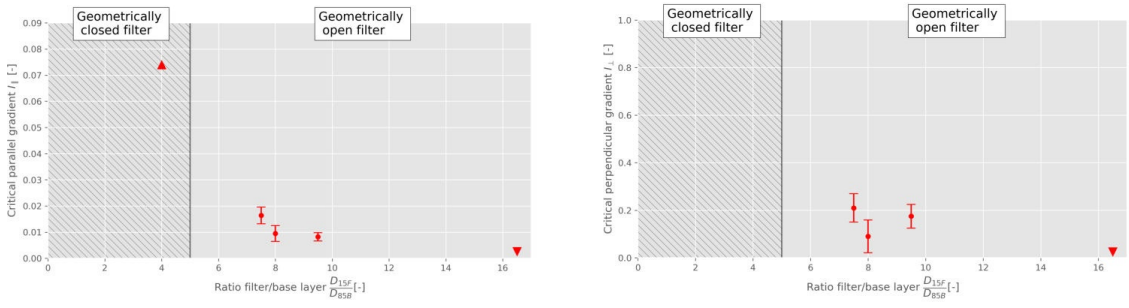

(a) Parallel gradient.

(b) Perpendicular gradient.

Figure 1.4: The relationship between the stability ratio and the critical hydraulic gradient (Van de Ven, 2019).

The focus of this study was on broadening the knowledge on such a filter. This was done by (1) physical modeling of other stability ratios that Van de Ven (2019) tested, (2) physical modeling of the combined configuration, (3) physical modeling using various characteristic base materials, (4) programming the model set-up numerically and (5) designing and constructing a new physical model that is able to test the influence of the superimposed load and inclined shape of a filter on the stability of the structure, as discussed in the next paragraph.

1.3. Objective

The objective of this thesis is to study the stability of an inversed geometrically open granular filter layer typically used at the lee side of rubble bunds retaining a sand-fill, based on the following research question:

"To what extent is an inversed geometrically open granular filter layer capable of preventing erosion of a land reclamation in rubble mound sand retaining structure?"

Since the stability of the filter structure depends on multiple factors, the research question is split-up into the following sub-questions:

- What is the influence of the stability ratio of the inversed geometrically open granular filter structure on the critical hydraulic gradient causing erosion?
- Does the characteristic grain size of the base material influence the critical hydraulic gradient if a constant ratio between the characteristic grain sizes of the filter and base material is taken, as proposed by De Graauw et al. (1983) for classical open granular filters?
- Does modeling the set-up with a combined flow regime influence the critical hydraulic gradient?
- How is it possible to test the influence of the superimposed load, resulting from the own weight of the reclamation, on the stability of an inversed geometrically open granular filter layer?

To create an understanding of the inversed geometrically open granular filter layer, Van de Ven (2019) constructed a physical model. This model is used to answer questions asked above. Moreover, a numerical model has been programmed to determine predict the hydraulic gradient in the physical model. This numerical model is used to design a new physical model that is able to cope with superimposed loads that correspond to a backfill with a height of 10 meters.

1.4. Hypothesis

It is expected that it is possible to create stable inversed geometrically open granular filter layer up to a certain extent. This means that the filter will be stable until a threshold value of the hydraulic gradient is reached. Filters with a lower stability ratio (SR), defined as the sieve diameter for which 15% of the mass of the filter material is smaller divided by the sieve diameter for which 85% of the mass of the base material is smaller $\left(\frac{d_{15,f}}{d_{85,b}}\right)$, will have a higher critical hydraulic gradient. Moreover, it is expected that the superimposed load has a stabilizing effect on the filter.

1.5. Axis system

The same axis system was used in this study as proposed by Van de Ven (2019), making the results comparable. Three gradients were distinguished in this system:

1. Longitudinal hydraulic gradient;
2. Parallel hydraulic gradient;
3. Perpendicular hydraulic gradient.

The longshore gradient was neglected since the study focuses on the 2-dimensional flow through the rubble mound breakwater, as illustrated in Figure 1.5. In Figure 1.6, a cut-out of the filter-base intersection (highlighted in blue in Figure 1.5) is given horizontally. By doing so, the inclined shape is neglected. Besides, the parallel and perpendicular hydraulic gradients are depicted in this figure.

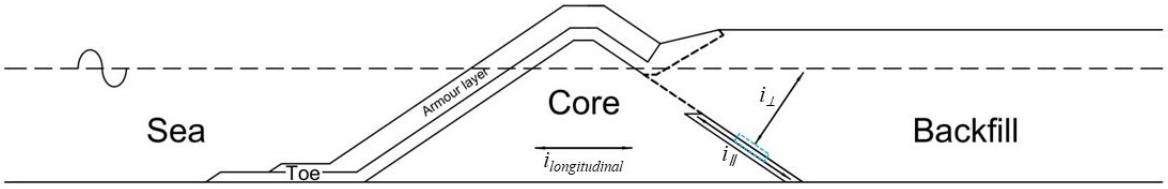

Figure 1.5: The three gradient distinguished in the axis system depicted in the cross section of a sand retaining rubble mound structure.

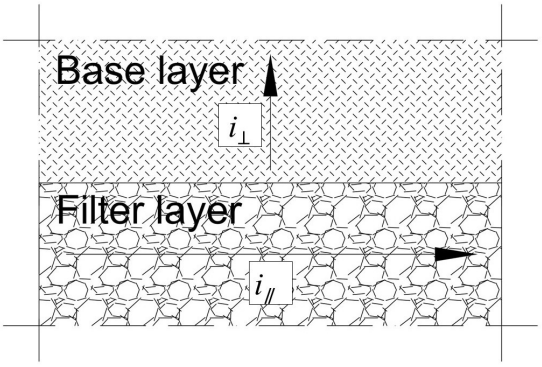

Figure 1.6: The parallel and perpendicular hydraulic gradient depicted in a cut-out of an inversed open granular filter.

1.6. Glossary

Base layer *The layer of a granular filter with the smallest grains.*

Critical hydraulic gradient *A threshold value of the hydraulic gradient above which erosion of the base layer occurs.*

Filter layer *The layer of a granular filter with the largest grains.*

Geometrically closed filter *A type of granular filter in which erosion is physically impossible.*

Geometrically open filter *A type of granular filter in which erosion is physically possible.*

Granular filter *An interface of granular material used to prevent or reduce erosion.*

Hydraulic gradient *The pressure difference between two points of interest divided by distance between between them.*

Inversed *Term used to mention that in a granular filter the base layer is placed on top of the filter layer, in contrast to the classical granular filters.*

Numerical model *A mathematical models that uses some sort of numerical time-stepping procedure to obtain the models behavior over time.*

Parallel hydraulic gradient *The component of the hydraulic gradient in the filter layer, parallel to the interface.*

Perpendicular hydraulic gradient *The component of the hydraulic gradient in the base layer, perpendicular to the interface.*

Physical model *A simplified representation of an object or phenomenon that needs to be investigated. The model can be used to simulate the physical conditions involved and to predict the particular constraints of the situation.*

Porous flow *Flow through a granular medium.*

Saturated filter layer *A fraction of the pore volume of the filter layer is occupied by base material.*

Soil arching *A phenomenon in which the shearing resistance tends to keep the yielding mass in its original position, reducing the pressure of the yielding part of the support and increasing the pressure on the adjoining stationary part.*

Stability ratio *The sieve diameter for which 15% of the mass of the filter material is smaller divided by the sieve diameter for which 85% of the mass of the base material is smaller* $\left(\frac{d_{15,f}}{d_{85,b}}\right)$.

Superimposed load *A vertical load exerted downwards on the filter interface.*

2

Literature study

In this chapter, the theoretical background and previously performed studies regarding the stability of filter structures are discussed. In order to design a certain structure, not restricted to hydraulic engineering projects, the strength of the structure should be sufficient enough to withstand the load exerted on it. The main load considered in this thesis was the flow through the breakwater towards the filter layer, which is discussed in Paragraph 2.1. Secondly, the grain size distributions of granular material is discussed in Paragraph 2.2. Thirdly, the current design criteria and literature on granular filters under different flow types are treated in Paragraph 2.3. Lastly, the phenomenon *soil arching* is discussed in Paragraph 2.4.

2.1. Flow through porous media

Porous flow is the expression used for a flow through a granular medium, like stones, pebbles, and sand. The flow is influenced by the porous medium in the form of friction. Because pressure and flow are related, this porous flow induces pressure differences over the filter. The hydraulic pressure difference over a certain distance is called the *hydraulic gradient*:

$$\rho_w g i = \frac{\partial p}{\partial x} \approx \frac{\Delta p}{\Delta x} \tag{2.1}$$

The motion of fluids could be described by the Navier-Stokes equations, which are based on the conservation of momentum (Newton's second law) and the conservation of mass. However, to apply this to a porous flow, every stone and every pore has to be taken into account. This is practically impossible (Schiereck and Verhagen, 2012) and could be avoided by using an average velocity though the porous medium, called the filter-velocity (u_f):

$$u_f = \frac{1}{A} \int \int_A u \, dA = n \cdot u \tag{2.2}$$

$$\text{With } n = \frac{V_P}{V_T}$$

2.1.1. (Extended) Forchheimer Equation and Darcy's Law

Forchheimer (1901) was one of the first to suggest that a course porous medium causes flow resistance that could be expressed with linear and quadratic terms. The first term could be seen as the laminar contribution to the resistance and the second term could be seen as the turbulent contribution to the resistance, as indicated in the Equation 2.3. Multiple (semi-) empirical formulae are composed for the coefficients a and b, which are dimensional (s/m and s^2/m^2 respectively) and contain several parameters (Van Gent, 1993), given in Table 2.1.

$$i = \underbrace{a u_f}_{\text{Laminar part}} + \underbrace{b|u_f|u_f}_{\text{Turbulent part}} \tag{2.3}$$

α_i	a_i	β_i	b_i	Source
150	$\alpha_{ERG} \cdot \frac{(1-n)^2}{n^3} \frac{\nu}{g \cdot d^2}$	1.75	$\beta_{ERG} \cdot \frac{1-n}{n^3} \frac{1}{g \cdot d}$	Ergun (1952)
780	$\alpha_{ENG} \cdot \frac{(1-n)^3}{n^2} \frac{\nu}{g \cdot d_{EQ}^2}$	1.8 – 3.6	$\beta_{ENG} \cdot \frac{1-n}{n^3} \frac{1}{g \cdot d_{EQ}}$	Engelund (1953)
290 (250 – 330)	$\alpha_K \cdot \frac{(1-n)^2}{n^3} \frac{\nu}{g \cdot d_{15}^2}$	1.4	$\beta_K \cdot \frac{1}{n^5} \frac{1}{g \cdot d_{15}}$	Koenders (1985)
160 (75 – 350)	$\alpha_{DA} \cdot \frac{(1-n)^2}{n^3} \frac{\nu}{g \cdot d_{15}^2}$	2.2 (0.9 – 5.3)	$\beta_{DA} \cdot \frac{1}{n^2} \frac{1}{g \cdot d_{15}}$	den Adel (1987)

Table 2.1: Formulae for coefficients α, a, β and b (Van Gent, 1993).

The non-dimensional coefficients α and β depend on several influences like grading, aspect ratio (maximum length devided by the length perpendicular to the direction of the maximum length) or shape of the grains, and must be determined using measurements.

Because the Forchheimer equation is only valid for steady flow situations, a time-dependent term is added to this equation by Polubarinova Kochina (1962) resulting in the extended Forchheimer Equation:

$$i = \underbrace{a u_f}_{\text{Laminar part}} + \underbrace{b|u_f|u_f}_{\text{Turbulent part}} + \underbrace{c\frac{\partial u_f}{\partial t}}_{\text{Inertial part}} \tag{2.4}$$

Similar to coefficients a and b, is c also a dimensional coefficient (s^2/m) containing several parameters. The relative importance of the three parts are discussed in Paragraph 2.1.3. Van Gent (1993) performed tests for oscillatory flow through coarse porous media and refers to the following expressions for the dimensional parameter c in the extended Forchheimer Equation (2.4):

$$c = \frac{1 + \gamma \frac{1-n}{n}}{ng} \tag{2.5}$$

The non-dimensional coefficient γ takes the phenomenon *added mass* into account. This is the extra momentum that is takes to accelerate a certain volume of water in a porous medium compared to a non-porous environment. This extra amount of momentum suggests that a larger volume of water has to be accelerated.

Besides, the relation between velocity and pressure gradient is sometimes written as follows:

$$u_f = k(i)^{\frac{1}{p}} \tag{2.6}$$

For laminar flow, $p = 1$, the Forchheimer Equation (2.3) reduces to Darcy's law (Equation 2.7 and 2.8) and the permeability (k) – discussed in Paragraph 2.1.2 – will be the inverse of parameter a.

$$Q = kA\frac{h_1 - h_2}{L} \tag{2.7}$$

This is equivalent to:

$$q = k\frac{\Delta h}{\Delta L} \tag{2.8}$$

2.1.2. Permeability

The permeability is a measure of the ability of a porous medium to allow fluids to pass through it. Besides the soil characteristics, the permeability also depends upon properties of the fluid. For thick fluids, the resistance is greater. This is expressed in the following formula:

$$k = \frac{\kappa \cdot \gamma_w}{\mu} \tag{2.9}$$

where μ is the dynamic viscosity of the fluid. The intrinsic permeability (κ) depends upon the geometry of the grains skeleton only. Kozeny-Carman gives a useful relation for the latter.

One could use a permeability test to determine the permeability of medium to high permeable soils, like the sand and gravels used in this study. Based on Darcy's law (Equation 2.8), the permeability can be determined if the specific discharge can be measured and the gradient $\left(\frac{\Delta h}{\Delta L}\right)$ is known. Such a test is shown in Figure A.1. In Table 2.2, indications of the permeability are given for various soil types (Verruijt, 1999).

Type of soil	Permeability (k) [m/s]
Gravel	$10^{-3} - 10^{-1}$
Sand	$10^{-6} - 10^{-3}$
Silt	$10^{-8} - 10^{-6}$
Clay	$10^{-10} - 10^{-8}$

Table 2.2: Indication of the permeability of various soil types (Verruijt, 1999) and CUR (2007).

Besides, according to CUR (2007), the Forchheimer Equation (Equation 2.3) could be used to determine the permeability of relatively granular material of interest by the use of the following equation:

$$k = \frac{1}{0.5 \cdot a_{ERG} + \sqrt{0.25 \cdot a_{ERG}^2 + b_{ERG} \cdot |i|}} \tag{2.10}$$

where $\alpha \approxeq 1000 - 2000$ and $\beta \approxeq 1.0 - 1.5$.

2.1.3. Laminar, turbulent and inertial resistance

The relative importance of the laminar, turbulent and inertial resistance, the three terms in the extended Forchheimer Equation (Equation 2.4), are estimated on the basis of two non-dimensional parameters. First of all, the magnitude of the turbulent resistance relative to the laminar resistance is determined using the Reynolds-number (Re), given in Equation 2.11. Secondly, the turbulent resistance relative to the inertial resistance is linear with the Keulegan-Carpenter number (KC), given in Equation 2.12. Last of all, the magnitude of the inertial resistance relative to the laminar resistance could be determined by comparing these two non-dimensional numbers, given in Equation 2.13. The regions with different dominant components are given in Figure 2.1 (Van Gent, 1993).

$$Re = \frac{Ud}{\nu} \tag{2.11}$$

$$KC = \frac{UT}{d} \tag{2.12}$$

$$\frac{Re}{KC} = \frac{d^2}{T\nu} \tag{2.13}$$

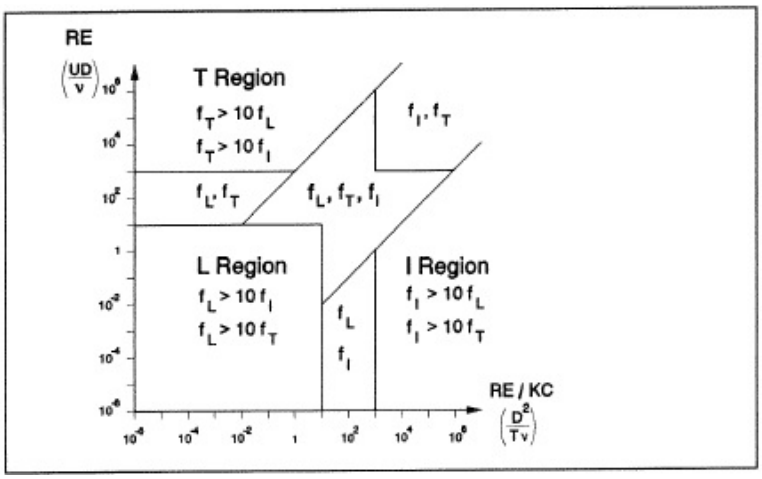

Figure 2.1: Regions with different dominant resistance components (Van Gent, 1993).

2.1.4. Flow propagation through a breakwater

Polidoro et al. (2015) examined the pressure distribution inside a breakwater for the abbreviation of geotextile by conducting tests with a breakwater having a watertight interface between the breakwater and the backfill. This close end can have a pressure difference over the rear end. The cross-section of the breakwater used by Polidoro et al. (2015) is given in Figure 2.2. The longitudinal hydraulic gradients through the breakwater core were determined. The gradients determined by probes near the rear end are given in Figure 2.3a. The gradients at the sea side are given in Figure 2.3b Moreover, the hydraulic gradients were depth dependent.

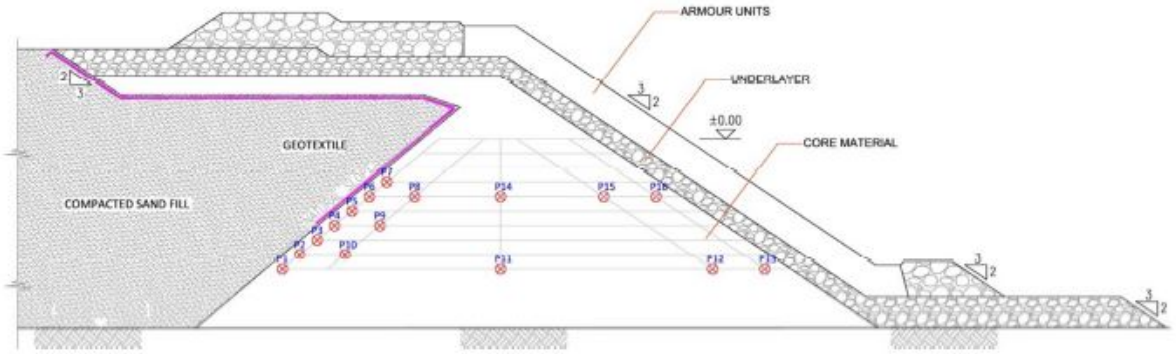

Figure 2.2: Cross-section of the breakwater used by Polidoro et al. (2015). Visible are the pressure sensors placed in a grid at the rear end of the breakwater to determine the hydraulic gradients.

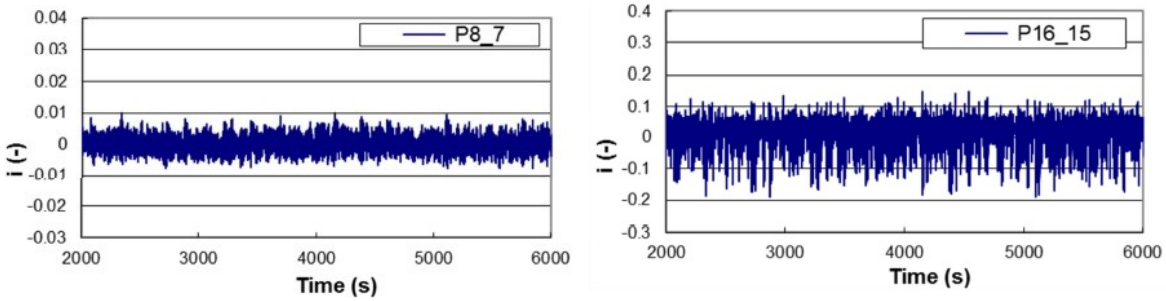

(a) Landward side.

(b) Seaward side.

Figure 2.3: Longitudinal hydraulic gradient determined by Polidoro et al. (2015).

Van de Ven (2019) made an estimation of the hydraulic gradients occurring in a breakwater by the use of OpenFOAM, an open source numerical model. It should be noted that this model is not yet scientifically verified, but used to give an estimation of the occurring pressures which could be compared to the physical model tests later on. In the thesis of Van de Ven (2019), the focus was on a parallel and a perpendicular hydraulic gradient, not the combination of both. The highest two percent of the hydraulic gradients through the granular filter layer are given in Figure 2.4.

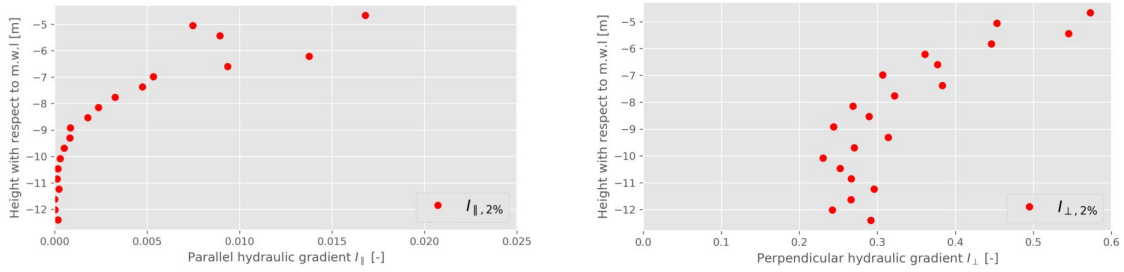

(a) Parallel gradient.

(b) Perpendicular gradient.

Figure 2.4: The 2% highest hydraulic gradients through the granular filter layer determined by Van de Ven (2019). The filter begins at -5 [m].

2.2. Grain size distribution

There are two main methods to determine the grain size distribution of a soil. The first method is to sieve the soil through multiple sieves with different mesh sizes. By weighing the residue of grains in every sieve, one could plot a sieve curve. This method is in particular applicable for sand. For larger soils, like gravel, blocking of the sieve openings could occur, stopping other grains to fall through the sieve. To determine a more precise sieve curve, a sample of the soil is taken and the weight of the individual stones are determined, resulting in a weight distribution. However, the grain diameter is used in the stability ratio, the main resistance parameter against erosion in this study. Therefore, the *nominal diameter* (d_n) is determined, which is by definition (Schiereck and Verhagen, 2012):

$$d_{n,50} = \sqrt[3]{\frac{W_{50}}{\rho_s}} \tag{2.14}$$

The relation between the grain diameter and the nominal diameter is described by the *shape factor* (F_s):

$$d_{n,50} = F_s \cdot d_{50} \tag{2.15}$$

Investigation of Laan (1981) has shown that in nearly all cases the F_s is between 0.7 and 0.9. The most common value used is 0.84 (Schiereck and Verhagen, 2012).

2.3. Granular filters

The definition of different type of filters is given in the Introduction. In this section, previous studies and design criteria of the stability of granular filters are discussed.

2.3.1. Geometrically closed granular filters

The traditional filter criteria are in fact criteria to design a geometrically closed filter. In order to do so, three different relations should be taken into account. First of all, the interface between the filter and the base layer should be stable. This means that there is no transport of subsoil material through the filter. Secondly, pressure build-up should be avoided. Finally, the soils should be internally stable in order to avoid internal erosion (CUR, 2010).

Stability Criterion

The idea behind a geometrically closed filter is that the space between the packed grains is much smaller than the grains themselves. In a filter layer of grains with varying diameter, the space between the grains is governed by the smaller grains. A general accepted size of these spaces is the $d_{15,f}$, which is the sieve diameter for which 15% of the mass of the filter particles is smaller. The largest grains of the base layer will get stuck in the pores of the filter layer and block the passage of all other grains of the base layer. These largest particle are often referred by $d_{85,b}$ (Schiereck and Verhagen, 2012). For nearly uniform graded filter material, Terzaghi and Peck (1948) came up with a relation. Heibaum (2004) came up with a relation for narrowly/standard graded sand and filter layer. For wide graded soil, the pores could be twice as small as normally graded filter materials, leading to a less conservative relationship (CUR, 2010). The relations are given below in, Equation 2.16.

$$\frac{d_{15,f}}{d_{85,b}} < \underbrace{4}_{\text{Uniform}} \text{ or } \underbrace{5}_{\text{Narrow graded}} \text{ or } \underbrace{10}_{\text{Wide graded}} \tag{2.16}$$

in which according to the EN-13383 European standard from CUR (2010):

Standard gradation	$\frac{d_{85}}{d_{15}} < 2.5$
(Wide) grade mixtures	$\frac{d_{85}}{d_{15}} > 2.5$

Permeability criterion
In order to prevent pressure build-up, the permeability of the filter layer should be larger than the permeability of the base layer. The permeability is governed by the smallest grains, resulting in a relation between the d_{15} of both layers (Schiereck and Verhagen, 2012). Again, Terzaghi and Peck (1948) came up with a relation for uniform filter and base layers. In Schiereck and Verhagen (2012), a somewhat less conservative relation is given. Both relations are given below in, Equation 2.17.

$$\frac{d_{15,f}}{d_{15,b}} > \underbrace{4}_{\text{Terzaghi and Peck (1948)}} \quad \text{or} \quad \underbrace{5}_{\text{Schiereck and Verhagen (2012)}} \tag{2.17}$$

Internal stability criterion
Suffusion or internal erosion occurs in filters that are internally unstable. However, internal erosion results in compaction and is less likely to lead to a rapid failure (CUR, 2010). The criteria for vertical flow in the direction of gravity are determined by Kenney and Lau (1985):

$$\frac{d_{10}}{d_5} < 4 \quad \text{and} \quad \frac{d_{20}}{d_{10}} < 4 \quad \text{and} \quad \frac{d_{30}}{d_{15}} < 4 \quad \text{and} \quad \frac{d_{40}}{d_{20}} < 4 \tag{2.18}$$

This corresponds to the relation given in Schiereck and Verhagen (2012):

$$\frac{d_{60}}{d_{10}} < 10 \tag{2.19}$$

Layer thickness
Geometrically closed filters should have a minimum thickness of at least 2-3 times the diameter of the larger particles in the base layer to be practically effective. For construction, especially by underwater placement, irregularities should be fully covered. Therefore, the thickness of the top layer should be at least 2-3 times the size of the larger particles used in the layer, with a minimum of 0.30 [m] (CUR, 2010).

2.3.2. Geometrically open granular filters

De Graauw et al. (1983) stated that the traditional design rules are of qualitative value, savings in terms of quantity could be achieved by reducing the number of filter layers. That study is based on the Eastern Scheldt Project and started by schematizing the flow situations as follows:

1. Steady and cyclic flow parallel to the interface;
2. Steady and cyclic flow perpendicular to the interface.

The study focused on measuring the critical hydraulic gradient (i_{cr}) in the filter layer and base material for the parallel and perpendicular situation respectively (Figure 2.5).

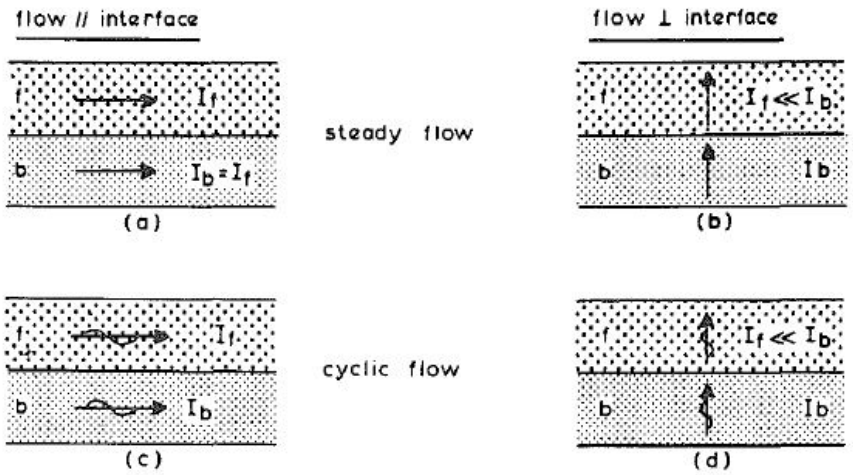

Figure 2.5: Flow situations considered by De Graauw et al. (1983)

Moreover, De Graauw et al. (1983) stated that i_{cr} is in general a function of:

1. The filter and base material characteristics: grain shapes, grain sizes, grading, density and packing.
2. The flow type, which may be characterized by the Reynolds number:

$$R = \frac{u_f \cdot D}{\nu} \tag{2.20}$$

$R < 4$: laminar flow
$R > 600 - 1000$: turbulent flow

In the case of a steady flow parallel to the interface and a constant ratio between the characteristic grain sizes of the filter and base material, the critical gradient is greater with fine base material then with coarse base material (Figure 2.6a). The following empirical relation was found by De Graauw et al. (1983) for this flow situation:

$$i_{cr} = \left(\frac{0.06}{n_f^3 \cdot d_{15,f}^{\frac{4}{3}}} + \frac{n_f^{\frac{5}{3}} \cdot d_{15,f}^{\frac{1}{3}}}{1000 \cdot d_{50,b}^{\frac{5}{3}}} \right) \cdot u_{*cr}^2 \tag{2.21}$$

in which (u_{*cr}):

$$u_{*cr}^2 = 1.3 \cdot d_{50,b}^{0.57} + 8.3 \cdot 10^{-8} \cdot d_{50,b}^{-1.2} \tag{2.22}$$

in which:

- $d_{15,f}$: filter stone diameter for which 15% of the mass of the paticles is smaller [m];
- $d_{50,b}$: filter stone diameter for which 50% of the mass of the paticles is smaller [m];
- u_{*cr}: critical shear velocity of base material, approximated from the Shield's diagram [m/s];
- n_f: porosity of filter material [-].

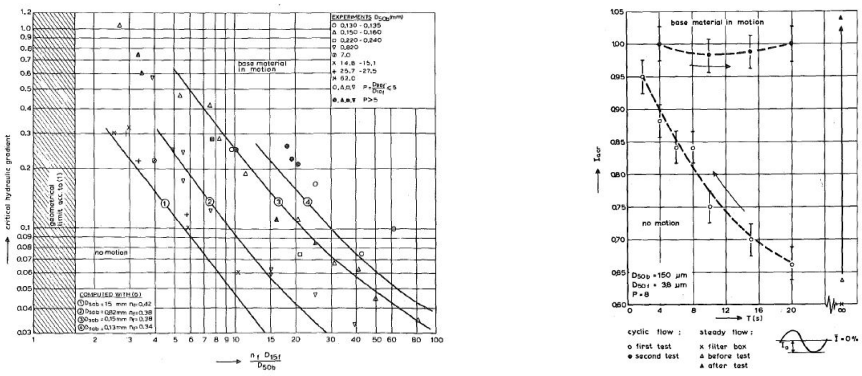

(a) Steady flow.

(b) Cyclic flow.

Figure 2.6: Critical hydraulic gradients for flow parallel to the interface (De Graauw et al., 1983).

For the parallel cyclic flow (Figure 2.6b), initially the critical amplitude of the hydraulic gradient increased with decreasing period. After compaction, it appeared that the critical hydraulic gradient was no longer depended on the period, not even for an infinite period (steady flow). Moreover, these tests indicated that the critical amplitude of the hydraulic gradient was of the same order of magnitude as with the steady flow. No figure is provided for a combined steady and cyclic flow parallel to the interface.

The other situation De Graauw et al. (1983) considered is the perpendicular flow through the interface. In the case of a steady flow situation, the trend with regard to the effect of the grain sizes is the same as with the parallel flow. The critical amplitudes of the hydraulic gradients under cyclic conditions are substantially lower than the ones in steady flow situation, both shown in Figure 2.7a. This is attributed to the formation of soil arches, which will be further elaborated on in Paragraph 2.4. For the combined situation of steady

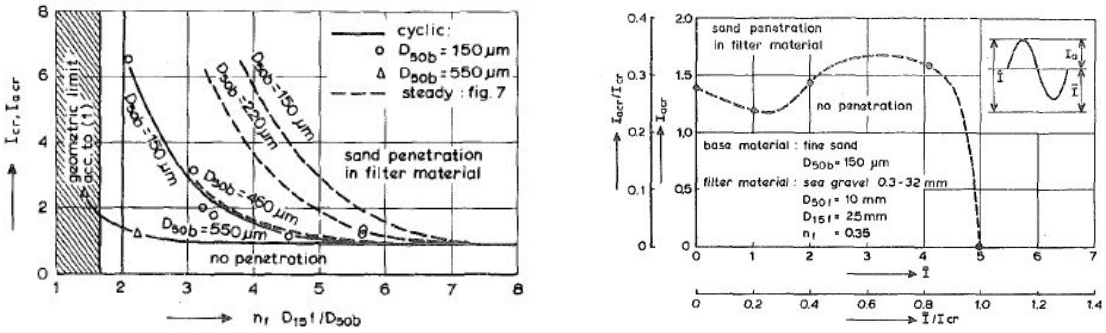

(a) Steady and cyclic flow comparison.

(b) Cyclic and steady flow combined.

Figure 2.7: Critical hydraulic gradients for flow perpendicular to the interface (De Graauw et al., 1983).

and cyclic flow perpendicular to the interface, it was found that for an increasing steady gradient, the critical amplitude of the hydraulic gradient is slightly reduced at first, then increases, and is suddenly reduced to zero when the steady gradient equals the steady flow critical gradient, as can be seen in Figure 2.7b.

CUR (2010) suggest to use a lower proportionality constant of 0.08 instead of 0.16 because the latter shows a rather high filter layer thickness for the cases with low turbulence.

Moreover, Klein Breteler (1989) conducted physical experiments with a horizontal stationary flow through a gravel filter layer on top of a sandy bed to determine the critical filter velocity ($u_{f,cr}$) and critical hydraulic gradient (i_{cr}) for sand transport. The results for both are compared to the following design formula for a horizontal interface without a vertical gradient:

$$u_{f,cr} = \left(\frac{n_f}{c} \left(\frac{d_{15,f}}{\nu} \right)^m \sqrt{\Psi \cdot \Delta_b \cdot g \cdot d_{50,b}} \right)^{\frac{1}{1-m}} \tag{2.23}$$

The measured critical values for the filter velocity and hydraulic gradient show a significant deviation to the calculated ones for two of the three test situations and a good similarity to the third test, tested in Klein Breteler (1989). The differences are considered unexplainable. Klein Breteler et al. (1992) formulated, together with Klein Breteler (1989), the following design formulae for steady flow, partly parallel and partly perpendicular to the interface. Please note that the main difference between Equation 2.23 and 2.24 is that the latter also includes the bed slope and the angle of repose of the base material.

$$u_{f,cr} = \left(\frac{n_f}{c} \left(\frac{d_{15,f}}{\nu_w} \right)^m \sqrt{\Psi \Delta g d_{50,b} \left(\frac{sin(\phi - \alpha)}{sin(\phi)} - \frac{i_\perp}{\Delta(1-n_b)} \right)} \right)^{\frac{1}{1-m}} \tag{2.24}$$

Equation 2.24 could be rewritten to an equation for the critical hydraulic gradient (i_{cr}) by for instance using the Forchheimer Equation (Equation 2.3):

$$i_{cr} = \frac{190\,(1-n_f)^2\,\nu}{g\,n_f^3\,d_{15,f}^2} u_{f,cr} + \frac{0.13}{n_f^5\,d_{15,f}\,g}\,u_{f,cr}^2 \tag{2.25}$$

Although verification indicated high variations, the tests results indicate that the critical velocity increases with an increasing slope. Moreover, the tests showed a reduced erosion development for sloped filter structures compared to flat ones. In practice, this means that the use of design guidelines for a horizontal interface would probably result in a conservative design when applied to sloped structures.

Bakker et al. (1994) proposed an optimum solution for the design of an granular open filter by making the filter layer as strong and the top layer, as a chain is as weak as it's weakest link. The following formula is presented using a Shields (1936) type of relationship:

$$\frac{d_{15,f}}{d_{85,b}} = \frac{2.2\psi_b\Delta_b}{C_0 e^2 \psi_t \Delta_t} \frac{R}{d_{50,t}} \tag{2.26}$$

This relationship is simplified in Equation 2.27 by assuming the following:

- $\Delta_b \approx \Delta_t$;
- The highest value of ψ_b/ψ_t has been takes as 0.4 based on the dependency of ψ on the Reynolds number;
- For a course base material, $d_{b,50} > 0.7$ [mm], e can be assumed to be a contact of approximately 0.24;
- $C_0 = 30$ for the situation of normal boundary layer turbulence.

$$\frac{d_{15,f}}{d_{50,b}} = 0.50\frac{R}{d_{50,t}} \tag{2.27}$$

This relationship implies that the bigger the hydraulic radius and the smaller the top-layer diameter, the higher the filter ratio. The smaller the hydraulic radius and the larger the top-layer diameter, the more the function approaches the geometrically closed criterion. Application of the relationship enables bed protections to be designed with one or two layers less than the traditional approach, especially if the diameter of the top layer is relatively small.

2.4. Soil arching

Shortly after the start of the Christian era, during the principate of Augustus, the aqueduct Pont du Gart was built by the Romans in order to carry water over the Gardon River. This bridge consists of three tiers of numerous arches of different sizes, shown in Figure 2.8 (Hauck, 1986). Pont du Gart is an ancient and good preserved example of a civil structure that relies on resolving forces of its own weight and superimposed load into compressive stresses, and therefore eliminating tensile stresses.

Figure 2.8: Pont du Gard, Vers-Pont-du-Gard, France.

This arch action also occurs in granular material (Figure 2.9), however, first a relative displacement needs to occur. This means that a part of the soil need to move more than the adjoining parts. This movement within the soil is opposed by a shearing resistance within the zone of contact between the yielding and the stationary masses. Since the shearing resistance tends to keep the yielding mass in its original position, it reduces the pressure of the yielding part of the support and increases the pressure on the adjoining stationary part, which is called *arching effect* (Terzaghi, 1943). Terzaghi (1943) investigated the soil arching phenomenon by the use of a trapdoor test, which is described in Appendix A.2.

(a) Box with gravel.

(b) Arch formed.

Figure 2.9: Trapdoor Test Performed by Ahmadi and Seyedi Hosseininia (2018).

Soil arching commonly exist when soil interacts with structure elements (stationary part). This arching effect has been widely studied in different domains of engineering, such as tunnels (Chen et al., 2011), piled embankments (Low et al., 1995), soil retaining walls (Paik and Salgado, 2003), hoppers (Enstad, 1975), (punctured) geotextiles (Chew et al., 2003), and less extensive in granular filters (De Graauw et al., 1983). Because of the applicability of the latter two on the filter situation considered in this thesis, they are elaborated on later in this paragraph.

2.4.1. Arching in filter structures

Arching in filter structures is studied in less extend than the domains discussed above. For a flow perpendicular to a gravel (on top of) sand interface, De Graauw et al. (1983) attributed the differences between the critical hydraulic gradients (at which erosion occurs) under cyclic and steady flow to the formation of arches of the base material particles between the grains of the filter layer, as illustrated in Figure 2.10a. Therefore, under steady flow conditions, the arching effect must be overcome by the gradient before transport is possible. However, these arches are not stable with cyclic flow causing the filter to be less stable. De Graauw et al. (1983) state that arching is strongly dependent on the ratio between the grain diameters of the base and filter material. The most hazardous situation occurs when the cyclic gradient (destructive force) amplitude is equal to the steady gradient component (transport capacity).

In the same study, it is presumed that the superimposed load only influences the critical hydraulic gradient in the case of a flow perpendicular to the interface. In the case that arching occurs $\left(\frac{n_f \cdot d_{15,f}}{d_{50,b}} = 1 \text{ to } 6\right)$, the arches may be subject to some kind of pre-stress due to increasing superimposed load, causing an increase of the gradient required to overcome the arching effect. However, when the ratio between the grain diameters of the filter and base material increases $\left(\frac{n_f \cdot d_{15,f}}{d_{50,b}} > 6\right)$, the gradient is less influenced by the superimposed load because of local fluidization. The influence of the superimposed load in both situations is illustrated in Figure 2.10c, in which arching is *filter A* and fluidization *filter B*.

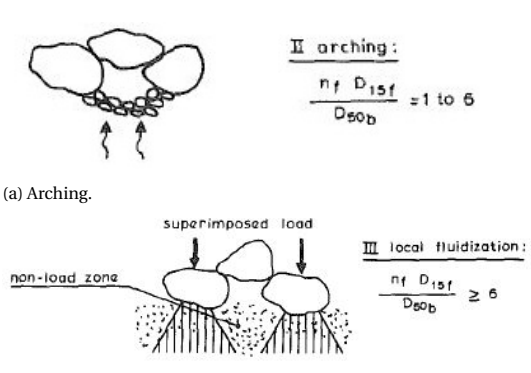

(a) Arching.

(b) Fluidization.

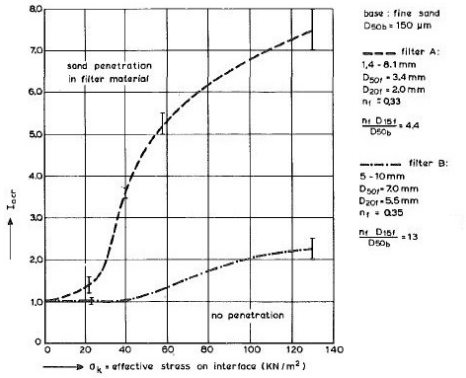

(c) The effect of superimposed load on the critical hydraulic gradient in the situation of perpendicular flow.

Figure 2.10: De Graauw et al. (1983)

Chew et al. (2003) investigated to the stability of punctured filters subjected to cyclic wave loading. Results show that a geotextile with a certain hole can still perform, if soil arching can be fully developed under certain cyclic wave load of a specific period. The latter is of influence because the hydraulic gradient across the interface is much larger in the case of shorter wave periods. Moreover, Chew et al. (2003) showed that the interface is more stable when greater superimposed load is applied. However, this effect of overburden load on the interface is limited up to a certain value of load. The reason for this is that a greater load implies denser soil packing and so more confinement exerted on the sand particles.

Even though soil arching is described as the main mechanism that influence the stability of the inversed open filter in Van de Ven (2019), the phenomena was beyond the scope of this thesis. This results in a gap of knowledge in the theory in which the filter structure could be more stable in reality then determined in Van de Ven (2019) because of too conservative critical hydraulic gradients.

2.5. Conclusion

Terzaghi and Peck (1948), Heibaum (2004) and CUR (2010) came up with criteria to determine whether a granular filter is open of closed. Moreover, Terzaghi and Peck (1948) and Schiereck and Verhagen (2012) came up with permeability criteria to avoid pressure build-up in a closed filter layer. The internal stability criteria of a closed filter is determined by CUR (2010) and Kenney and Lau (1985). The open granular filter structure was studied for multiple applications, all with different empirical relationships. However, it is unknown how these criteria hold for an inversed open granular filter structure.

Moreover, studies were preformed to determine the influence of the arching effect and the superimposed load on the stability of standard open filters (De Graauw et al., 1983) and punctured geotextiles (Chew et al., 2003). However, little is known about the influence of these effects on an inversed open filter while it is believed that arching is a governing phenomenon for resistance.

3

Physical model description

This chapter describes the physical model used to conduct tests on the inversed geometrically open granular filter structures. The model that was used, is the same container as used by Tutein Nolthenius (2018) and Van de Ven (2019). However, to make room for new instruments, some adjustments were made.

Firstly, the model layout is discussed together with the different configurations that were possible to test in the model and the components used to construct them. Furthermore, the test objective and the processes and parameters that influence the physical model tests are discussed. After the equipment is treated, the test rigs are given, including the location of the model components and instruments for the selected model set-ups.

Secondly, it is explained how the plunger induced the hydraulic gradient as the factor which causes the erosion. In addition, the granular material used and the stability ratios determined by combining the sand and gravel are discussed as main resistance parameter against erosion. How erosion was detected and the assumptions made in order to do so are discussed hereafter.

Finalizing this chapter, the installation of a test is given in a step-by-step approach, an overview of the tests conducted, the model effect, and how the output of the instruments were analyzed are discussed. The results of the tests discussed in this chapter are given in Chapter 4.

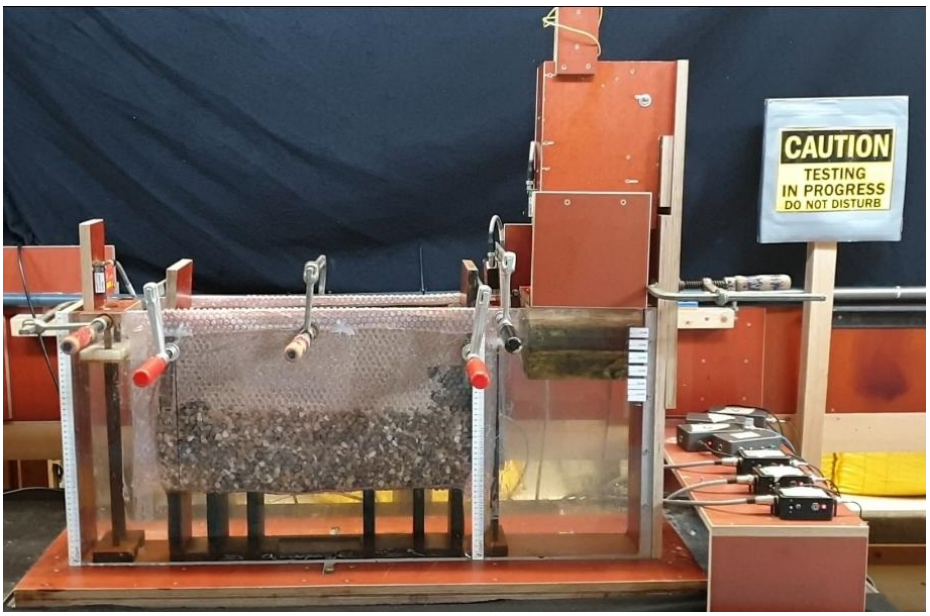

Figure 3.1: The model used to study the inversed granular open filter. In this photo, the parallel set-up is shown.

3.1. The model

The physical model that was used for the tests is the same container as used by Tutein Nolthenius (2018) and Van de Ven (2019). The outline of the model was a waterproof elongated container with transparent front and back. In this container, three compartments were allocated:

- Compartment A: in which the water level was controlled by the use of a plunger and measured;
- Compartment B: in which the base and filter layers were installed. In this compartment, the hydraulic gradient generated by the water level difference between compartment A and B was increased until erosion takes place;
- Compartment C: in which the water level was measured.

The compartments were separated with plywood for a watertight boundary and with wire mesh to keep the gravel in place while allowing water to pass. More information on the model components is given in Paragraph 3.1.2. The compartments are indicated in Figure 3.2.

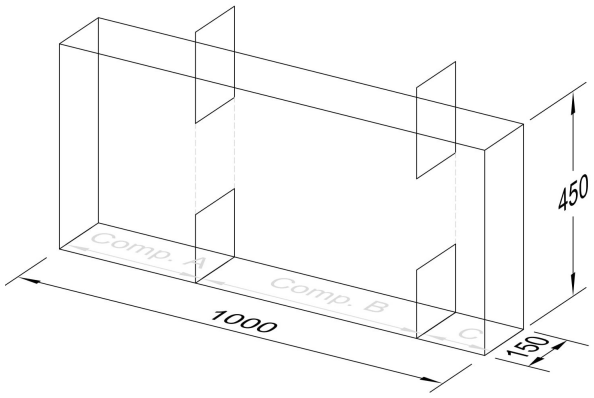

Figure 3.2: The outline of the physical model. The lengths of the compartments are 320, 520 and 160 [mm] in alphabetical order. All dimensions are given in millimeters.

3.1.1. Model configurations

There were three different configurations that could be tested in the model. The first configuration was the parallel set-up wherein the top of the sand layer in compartment B was closed air-tight. This forced the porous flow solely from Compartment A through the gravel filter layer to Compartment C and back. Therefore, the hydraulic pressures were measured by horizontally aligned pressure sensors in the filter layer and the water levels of the outer compartments. The parallel configuration is illustrated in Figure 3.3a.

Secondly, the perpendicular configuration could been set-up in the model, however, no perpendicular tests were conducted during this study. More information on the perpendicular configuration could be found in Appendix B.1.

Last of all, a combination of both porous flows was simulated whereby a vertical flow through the sand layer and a horizontal flow through the filter were considered, as indicated in Figure 3.3b. Both the parallel and perpendicular hydraulic gradients were measured in this set-up.

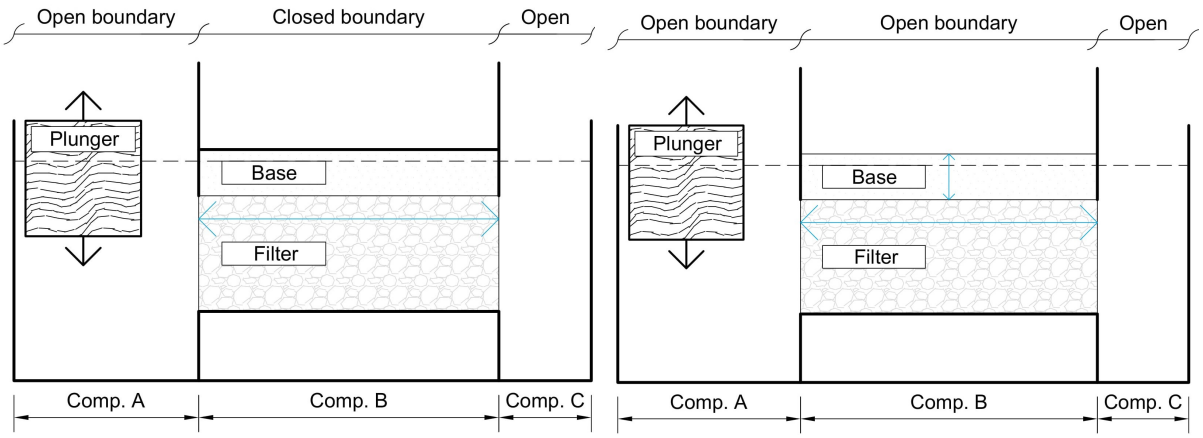

(a) Parallel configuration.

(b) Combined configuration.

Figure 3.3: Schematic representation of the used configurations with the open and closed boundaries. In blue, the flow and hydraulic gradient orientation are illustrated. The test rigs are given in Paragraph 3.3.

3.1.2. Model components

Multiple type of components were used during modeling and to convert the model between the parallel and combined set-up. First of all, a plunger was used in every test in combination with a stepper motor to induce water level fluctuations, shown in Figure 3.4a. Secondly, a set of bottom cells were used in every test, shown in Figure 3.4b. These cells were placed underneath the filter layer and provided room to make the erosion visible. Two division screens were mounted to the bottom cells to enclose Compartment B. These screens consisted of plywood to enclose the base layer water tight, a mesh grid to enclose the filter layer while allowing the water to flow through, and geotextile to avoid sand passing by the filter layer into Compartment A and C. Lastly, the seal that was used to close of Compartment B for the parallel set up is given in Figure 3.4d. The placement of the components in both set-ups are given in Paragraph 3.3.

(a) Plunger and motor.

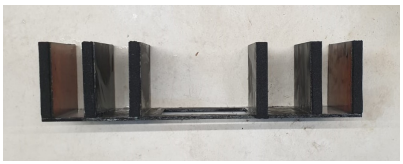

(b) Bottom cells.

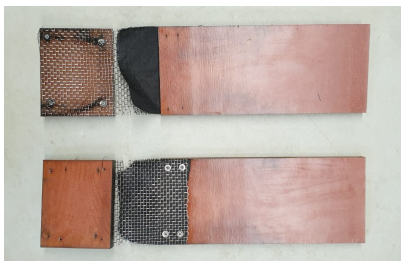

(c) Division screen.

(d) Top seal.

Figure 3.4: Model components.

3.1.3. Test objective

Van de Ven (2019) constructed and used the physical model in order to create an understanding of the relation between the forcing of - and the resistance against erosion of the inversed gravel-sand filter structure. The results were limited to parallel and perpendicular flows, characteristic grain sizes were compared but not for a constant stability ratio, and a small number of stability ratio's were tested. The goal of the tests in the same model were to broaden the knowledge in the understanding of the filter structure by taking the above into account.

3.1.4. Phenomena of interest

In order to create an optimized representation of the reality by physical modeling, important processes need to be kept in mind. It was expected that the following processes influence the inversed filter experiments the most:

- **Arching**
  Arching, as described in Paragraph 2.4, could influence the stability of the base layer on top of the filter layer. The influence of arching could be increased by a superimposed load. This phenomena was not tested in this study, but a new model is provided to conduct superimposed load tests in the following stage of the research line.

- **Hydraulic forcing**
  The plunger induced hydraulic forcing – quantified as hydraulic gradient – on the filter layer was the load responsible for the erosion. This force could break down the arching effect leading to erosion of the base layer through the filter layer. The way in which this hydraulic gradient was forced is described in Paragraph 3.5.

- **Saturation of the filter layer**
  The (initial) level of sediment saturation in the gravel pore space influenced the erosion detected in a test. By cleaning the gravel, one was sure that no sediments were trapped in the pores of the filter layer. This ensured that the erosion detected during the test originated from the base layer and made the various tests comparable.

3.1.5. Parameters of interest

Multiple parameters had an influence on the stability of the inversed filter structure. In this subsection, the parameters with the greatest influence on the resistance on the erosion and the main load parameter are explained. A list of parameters influencing the hydraulic gradient in the physical model is given in Appendix B.2.

- **Hydraulic gradient** ($i_{\parallel}$ and i_{combined})
  The hydraulic gradient is a dimensionless load parameter (equation 2.1) which was increased during a single test until erosion was detected, giving the critical hydraulic gradient (i_{cr}) for that particular set-up. The parameter was on itself a result of other parameters, including but not limited to:

  - Plunger period;
  - Plunger amplitude;
  - Permeability of the considered granular layers;
  - Filter height;
  - Dimensions of compartments in the model.

- **The stability ratio** $\left(\frac{d_{15,f}}{d_{85,b}}\right)$
  The stability ratio is by definition the sieve diameter for which 15% of the mass of the filter particles is smaller ($d_{15,f}$) divided by the the sieve diameter for which 85% of the mass of the base material particles is smaller ($d_{85,b}$). The $d_{15,f}$ corresponds to the space between the grains in the filter layer. The $d_{85,b}$ corresponds to the larger grains of the base material that will get stuck in the pores of the filter layer.

  This dimensionless resistance parameter was altered over the tests and plotted against the corresponding critical hydraulic gradient. The smaller the ratio, the closer the filter hence a larger critical hydraulic gradient was achieved.

- **The characteristic grain sizes**
  The critical gradient could be greater with fine base material then with coarse base material (De Graauw et al., 1983). By executing multiple tests in which the stability ratio remained equal but the characteristic grain sizes differed, the influence of the latter was examined.

- **The superimposed load (q_s)**
  It was expected that the critical hydraulic gradient increased when the filter is vertically loaded. This parameter was used to design the new model in Chapter 6, but is not physically tested in this study.

Besides the above mentioned stability ratio and hydraulic gradient, two other dimensionless parameters were of interest:

1. **Reynolds number (Re)**
   The magnitude of the turbulent resistance relative to the laminar resistance (equation 2.11).

2. **Keulegan-Carpenter number (KC)**
   The turbulent resistance relative to the inertial resistance (equation 2.12).

The laminar resistance was expected to be dominant for the perpendicular flow. For the parallel flow, a combination of laminar, turbulent and inertial resistance was expected.

3.2. Equipment

Multiple types of equipment were used in order to capture various variables during the physical model tests. The processing of the output of the equipment is explained in this paragraph. Furthermore, the characteristics and function of each type of instrument is described. Extra information about the equipment, is given in Appendix B.3.

3.2.1. Data processing

Every instrument used a 10 [V] instrumentation amplifier (Figure 3.5) as power supply. Moreover, the signal from the equipment was amplified 200, 400, 1000 or 3000 times before it was transmitted from the instrumentation amplifier to the data acquisition module (DAQ) (Figure 3.6). The DAQ converted the analog signals from the measurement devices into a digital signal where after transmitted the signal to a computer. The digital signals were analyzed and saved by the use of DASYlab, a data acquisition system.

Figure 3.5: Instrument amplifier.

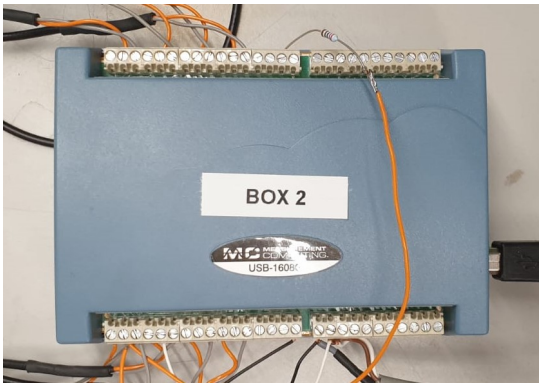

Figure 3.6: Data acquisition module.

3.2.2. Lasers

Three Micro-Epsilon lasers of the type optoNCDT 1302 (Figure B.2a) were used during the physical modeling. These type 2 lasers were used to measure the plunger position and the water level of the two outer compartments of the model continuously.

One laser was attached to the stationary part above the plunger and projected the light point on top of the plunger, as shown in Figure 3.7a. This top surface of the plunger was emerged at all times in order to achieve accurate output. The other two lasers were attached to custom designed floaters, shown in Figure B.2b. A light spot was projected on top of the floating styrofoam hence the water level fluctuations were measured, as can be seen in Figure 3.7b.

Because of the fixed position of the lasers, they were only calibrated once before the first test by plotting a regression line of the output versus the corresponding plunger position c.q. water levels (Figure B.2c).

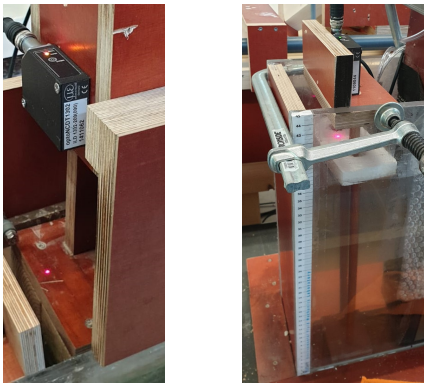

(a) Laser on plunger. (b) Laser on floater.

Figure 3.7: Placement of the lasers.

3.2.3. Differential pressure sensors

Differential pressure sensors (PS) measured the difference of two adjacent chambers by the use of a membrane. These two chambers were connected to the outer tubes in Figure 3.8a. To make this sensor suitable for the application, some adjustments were made, which are described in Appendix B.3.2.

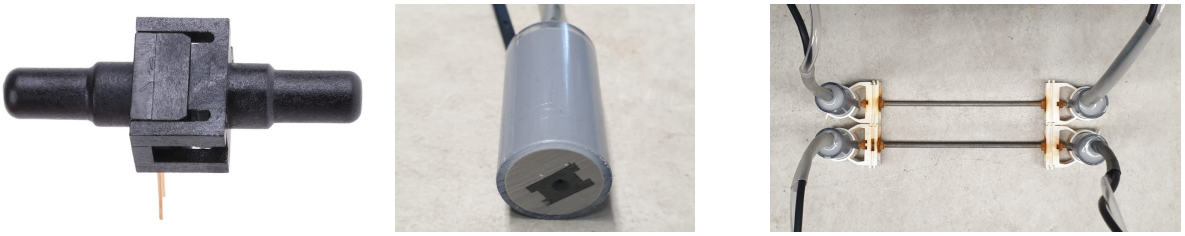

(a) Before modifications. (b) After modifications. (c) Fixed distance between the sensors by using a custom made bar.

Figure 3.8: The differential pressure sensors used during the testings.

The pressure sensors were used to determine the hydraulic gradients in the layer of placement during the tests. By measuring the water pressure at different locations in a filter layer and a known distance between the sensors, the gradient was calculated according Equation 2.1. The sensors were mounted in pairs to a bar, as shown in Figure 3.8c. Because of this, there were always two signals per location in case one sensor failed, and was ensured that the distances between the sensors was fixed during the test.

Before using the sensors in the model, every sensor was tested to determine if the sensors functions properly. This prior test calibration is described in Appendix B.3.2. Furthermore, a saturated calibration was done

prior and during every test for every pressure cell used in the set-up (Figure B.3c.). During the infill of water into the model, the output of the sensors were noted for every centimeter of water level increase. In addition, the sensors were re-calibrated every 3 hours, before the servo velocity was increased, by moving the plunger into three different levels for 10 minutes:

1. The plunger was raised out of the water;
2. The plunger was raised to the highest point of the plunger signal;
3. The plunger was lowered to the lowest point of the plunger signal;
4. Plunger signal was started.

The output signal of the pressure sensors were calibrated to the output of the lasers, as discussed in the previous paragraph, determining the water levels in the model by linear regression (Figure 3.9). More information on processing the data is given in Paragraph 3.10.

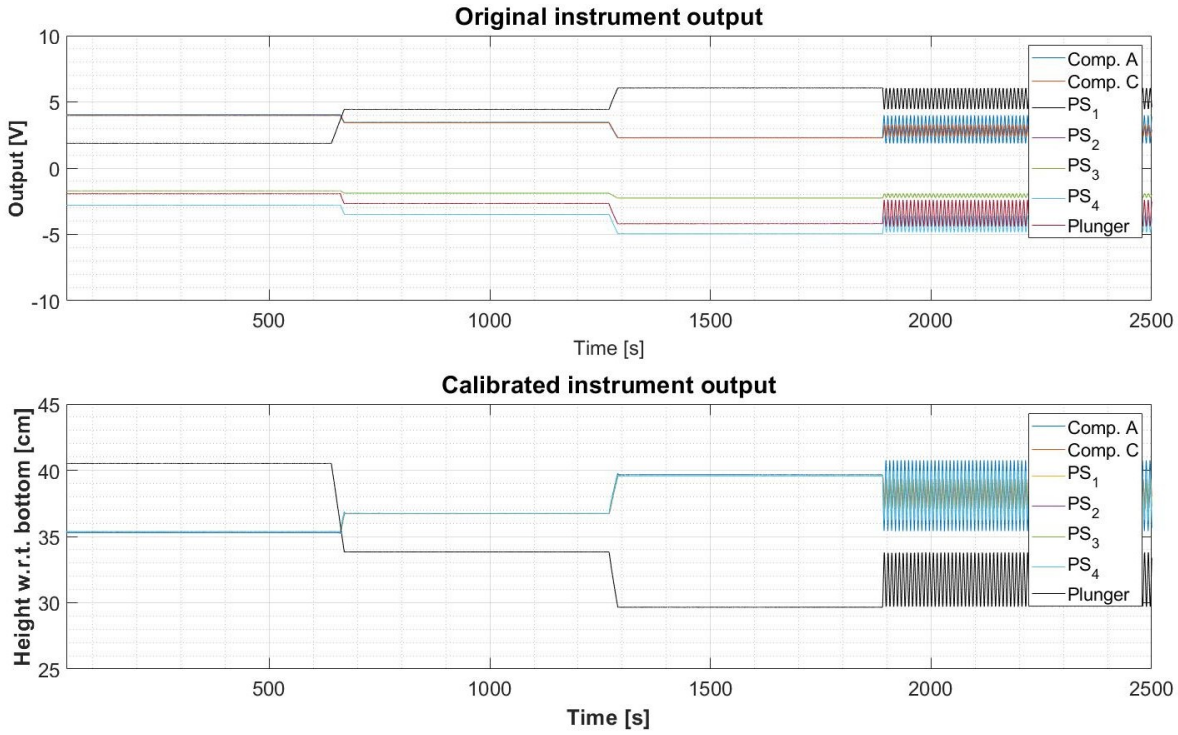

Figure 3.9: Calibration of the instrument output.

3.2.4. Servo

A step servo of the type 24Q-3RG was used. This servo was driven by the program Step-Servo Quick Tuner and used to drive the plunger in a computer controlled manner. The rotary movement of the servo was converted into a linear movement of the plunger by a slider-crank mechanism, as shown in Figure 3.10b. The servo was automatically calibrated at the beginning of each test.

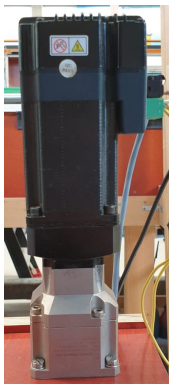

(a) Servo.

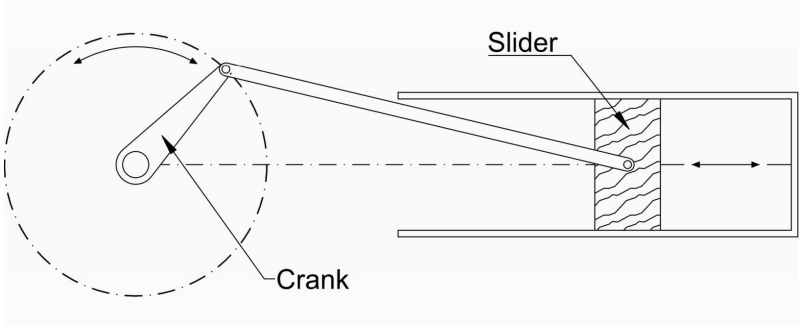

(b) The functioning of a slide-crank mechanism.

Figure 3.10: Plunger

3.2.5. Video camera

To analyze the erosion of the base material trough the filter layer, a webcam was used. The webcam was located in front of the bottom cells of the model, underneath the filter layer. In order to increase the visibility, two LED construction lights were placed behind the model. LED lights were a safer choice since they produced less heat. Moreover, increase of water temperature will have influenced the output of the pressure sensors.

Every segment of a test with a constant plunger velocity lasted approximately 3 hours and snapshots were taken every 10 minutes by the webcam. Base on these photos, it was possible the trace back in which segment the erosion was started.

3.2.6. Load cell

In the first few (concept) tests, a double bending beam load cell of the type UTICELL model 190i in combination with a custom made stand and scale was used in attempt to measure the erosion continuously. Unfortunately, despite the promising first outputs, the load cell broke down. More information on this cell is given in Appendix B.3.3.

3.3. Test rigs

In this paragraph, the previous threaded components and equipment are shown in the schematic parallel and combined test rigs. A photo of the parallel test rig is given in Figure 3.1.

3.3.1. Parallel configuration

In the parallel configuration, the filter structure – consisting of a 200, 100 or 80 [mm] filter layer underneath a base layer – was closed of with a top seal (Figure 3.4d) to induce a strictly parallel porous flow. The gravel layer was reduced over multiple tests in order to achieve higher hydraulic gradients.

Two pairs of pressure sensors were placed horizontally in the middle of gravel layer with a fixed and known distance. The pressure sensors and other equipment discussed in Paragraph 3.2 are illustrated in Figure 3.11.

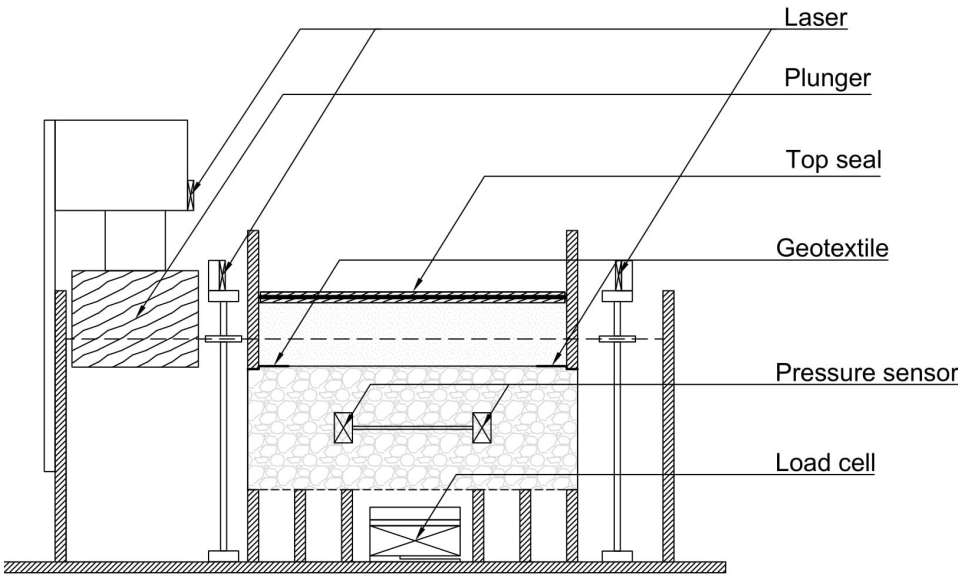

Figure 3.11: Test rig of the parallel configuration.

3.3.2. Combined configuration

In the combined configuration, no model boundaries were closed off. The filter layer height was 150 [mm] in order to make room for the vertical placed pressure sensors in the base layer. Like the horizontal placed pressure sensors, the vertical ones were mounted to a strip in order to fix the distance between them.

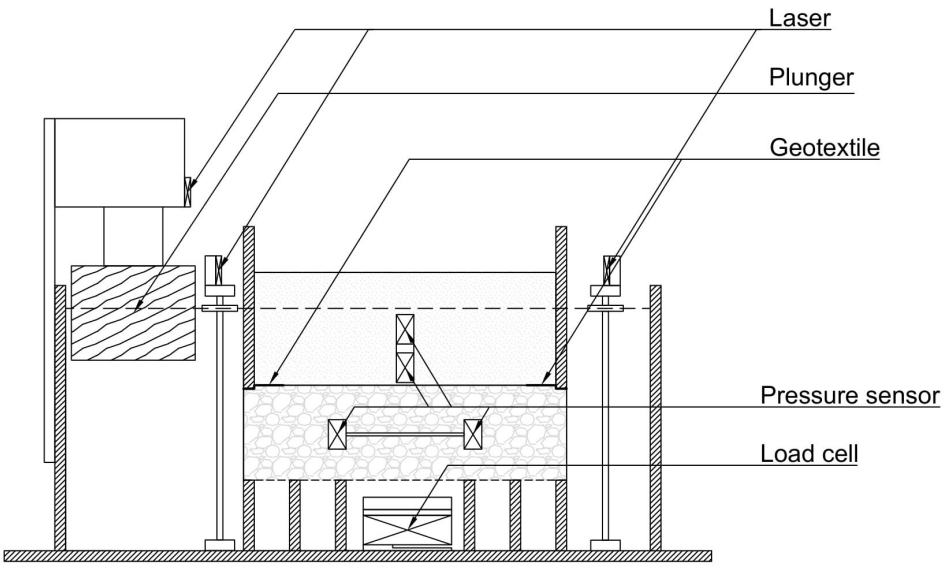

Figure 3.12: Test rig of the combined configuration.

3.4. Model effects

By executing physical model tests, one imitates a representation of the reality in order to achieve a certain goal. By simulating the reality in a model, the model could bring effects that influences the results. These model effects and the measures taken to minimize them are listed in this paragraph.

Because the filter structures tested in this study were a cut-out of the real structure, as illustrated in Figure 1.5 and 1.6, no scaling effect are applicable. By conducting physical model tests in the new and larger model, as designed in Chapter 6, this assumption could be reflected.

3.4.1. Initial saturation of the filter layer

The initial sediment saturation in the pore space of the filter layer influenced the point of erosion since it made it impossible to trace back the origin of the sand that erodes into the bottom cells. To minimize this effect, the gravel was washed extensively. To analyze this effect, tests were carried out with unsaturated and partly saturated filter layers. This model effect is also discussed in Paragraph 3.7.

3.4.2. Wall effects

In the model, a cut-out with a width of 15 [cm] of a granular filter was tested. This resulted in a border region between the perspex and gravel with larger pores compared the the gravel itself. Because of this, sand could by-pass the filter layer into the bottom cells. The wall effect was reduced by attaching bubble plastic to the front and back of the container. Geotextile was placed at the sides of the of the middle compartment to block the erosion of sand into the two outer compartments. The placement of bubble plastic is schematically shown in Figure 3.13.

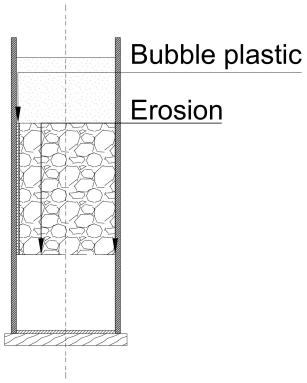

Figure 3.13: Schematic representation of the bubble plastic. On the left hand side, the bubble plastic is taped to the perspex resulting in a erosion through the filter layer. On the right hand side, no bubble plastic is used. This results in sand by-passing the filter layer into the bottom cells as indicated by the arrow.

3.4.3. Flow by-passing the bottom cells

The flow induced by the plunger could by-pass the filter layer by flowing along the bottom cells. To prevent this, foam tape was used on the side of the bottom cells. After the model tests were conducted, it was found that water also by-passed the filter layer in the space created by the mesh grids on top of the bottom cells, resulting in a lower average permeability for the filter layer.

3.4.4. Plunger vibrations

Two types of vibrations took place by oscillating the plunger. Firstly, the servo driving the plunger vibrated during rotating. Secondly, the plunger rubbed against the side of the model resulting is a shocking movement. The latter mainly took place during the lower servo velocities. The vibrations were filtered from the output signal, as is described in Paragraph 3.10.

3.4.5. Inflow and outflow effects

During a test, the water flowed from open water into a porous medium and into open water again. By doing so, in and outflow effects took place that will not happen in reality. Therefore, the pressure sensors were

placed 130 [mm] away from each outer compartment (a quarter of the length of Compartment B). Moreover, the mesh used to maintain the gravel in the filter layer blocked the flow. The blockage rate by the grid was significantly lower than the porosity of the gravel, whereby this effect could be neglected.

3.5. Movement of the plunger

In this paragraph, the movement of the plunger and the corresponding hydraulic gradient is discussed. During a single test, the hydraulic gradient was increased until erosion was detected. The hydraulic gradient is by definition a pressure difference over a distance, meaning for the parallel test rig a water level difference between the two outer compartments over the length of the filter layer. The water level difference was induced by a plunger: a 220 x 140 x 160 [mm] wooden block connected to a computer controlled servo, as shown in Figure 3.4a and described in Paragraph 3.2.4 respectively.

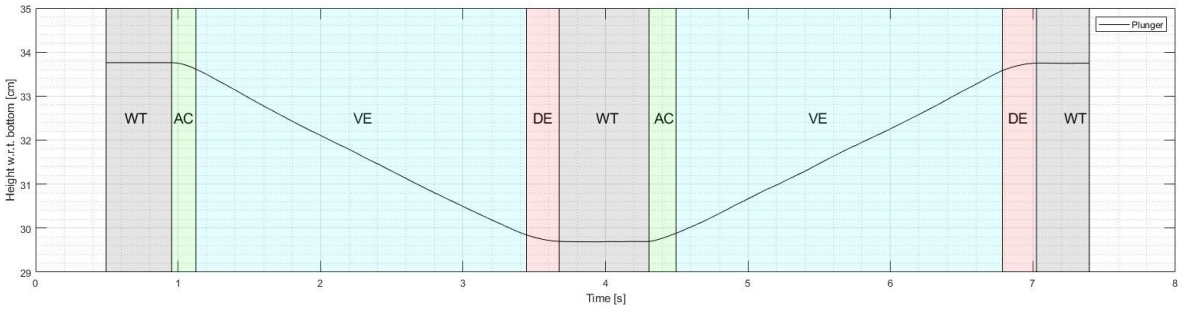

Figure 3.14: Plunger signal with markers indicating servo commands.

In Figure 3.14, an example of a plunger signal is given. The areas highlighted indicate the below listed commands used to program the movement of the servo and therefore the plunger. More information about the type of plunger signal is given in Paragraph 5.2. Deviations of the plunger signal compared to the command occurred.

- **Waiting time** (WT) [s]:
  Every plunger period was paused by a waiting time. During this moment of standstill, the water levels in the two outer compartments equalized. This was necessary in order to let the same amount of water flow through the filter layer, regardless the granular material used in the set-up. This made the tests comparable to each other. If a plunger signal without waiting time was used, the discharge through a filter layer with a lower permeability would be less if the flow reversed before the water in the two compartment were equal.

- **Acceleration** (AC) [r/s/s]
  The plunger was accelerated until the programmed velocity is reached.

- **Velocity** (VE) [r/s]
  The velocity is the speed that the plunger had for the largest part of the signal. A constant plunger velocity resulted in a constant porous flow and hydraulic gradient. By increasing the velocity, higher hydraulic gradient were achieved.

- **Deceleration** (DE) [r/s/s]
  The deceleration was the phase between the velocity and the waiting time. Just like the acceleration, a high value resulted in a longer period of constant velocity while a low value resulted in a smoother signal and less waves in the model.

3.6. Granular material

Since the stability ratio was the main load parameter, this ratio was altered over the tests in order to determine the influence of it. Multiple types of sand and gravel were analyzed and combined to achieve the stability ratios of interest. The sand was sieved by the use of multiple test sieves in a sieve shaker (). To analyze the gravel, approximately 1000 single grains were weighted per type. This was more precise compared to sieving because blockage of openings could occur during sieving, obstructing smaller grains to pass through the sieve. The mass of the grains were converted into grain diameters by calculating the nominal diameter and using a shape factor (F_s) of 0.84, as discussed in Paragraph 2.2. However, this value could vary between 0.7 and 0.9, depending on the grain characteristics. Decreasing F_s leads to higher SR-values. In Figure 3.15, the sieve curves of the selected granular materials are given.

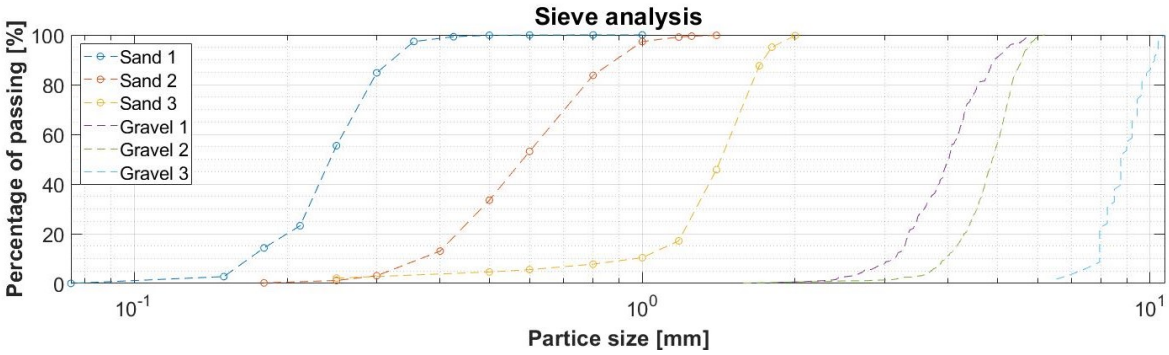

Figure 3.15: Sieve analysis of the granular material.

In Table 3.1, the d_{15} and d_{85} of the materials are given to determine the gradation of the material. All type of material used in this study had a standard gradation conform CUR (2010) ($\frac{d_{85}}{d_{15}} < 2.5$) leading to a geometrically closed filter criterion if $SR = \frac{d_{15,f}}{d_{85,b}} < 5$, as mentioned in Paragraph 2.3.1. The d_{50}-value is a good single classification of the material.

	Sand 1	**Sand 2**	**Sand 3**	**Gravel 1**	**Gravel 2**	**Gravel 3**	
d_{15}	0.15	0.31	0.94	3.29	4.16	7.95	[mm]
d_{50}	0.21	0.48	1.20	4.02	4.89	8.75	[mm]
d_{85}	0.25	0.62	1.39	4.80	5.44	9.83	[mm]
$\frac{d_{85}}{d_{15}}$	1.65	2.00	1.48	1.46	1.31	1.24	[-]

Table 3.1: Overview of characteristic grain sizes of the granular material.

In Table 3.2, the possible stability ratios are given. The stability ratios tested in this study are indicated in bold. These ratios were not tested by Van de Ven (2019) and are therefore seen as an addition to the research line.

	Sand 1	Sand 2	Sand 3
Gravel 1	**13.09**	5.31	2.37
Gravel 2	16.58	**6.73**	3.00
Gravel 3	31.68	**12.86**	**5.74**

Table 3.2: Stability ratios combinations possible by the selected granular material. The tested ratios are indicated in bold.

3.7. Detecting point of erosion

The definition of erosion was set to be the point of sand moving out of the base layer into the filter layer. In reality this means that, due to gravity, the sand will not return into the base layer and is lost from the system. However, it was not possible to detect the erosion at this border visually since the gravel and bubble plastic was blocking the view. Therefore, if the sand entered one of the bottom cells for the first time after the test had started, was chosen to be the point of erosion. By setting up the model, discussed in detail in Paragraph 3.8, the gravel was washed extensively to ensure an unsaturated filter layer. This made it certain that all the erosion captured in the bottom cells originated from the base layer. In tests with relatively high stability ratios, initial infall was detected in a low degree. Generally, the erosion did not continue until multiple ascending plunger velocity segments were executed, indicating a clear difference between initial erosion and plunger induced erosion. An example of two snapshot between which erosion took place is given in Figure 3.16. After the moment of erosion of a test was determined, the instrument output of that segment and the previous one was analyzed in order to capture the corresponding critical hydraulic gradient range. This is discussed in Paragraph 3.10. Erosion was found in both the beginning of a test segment as later on in the segment.

(a) A snapshot of the bottom cells inclusive initial infall before erosion was detected.

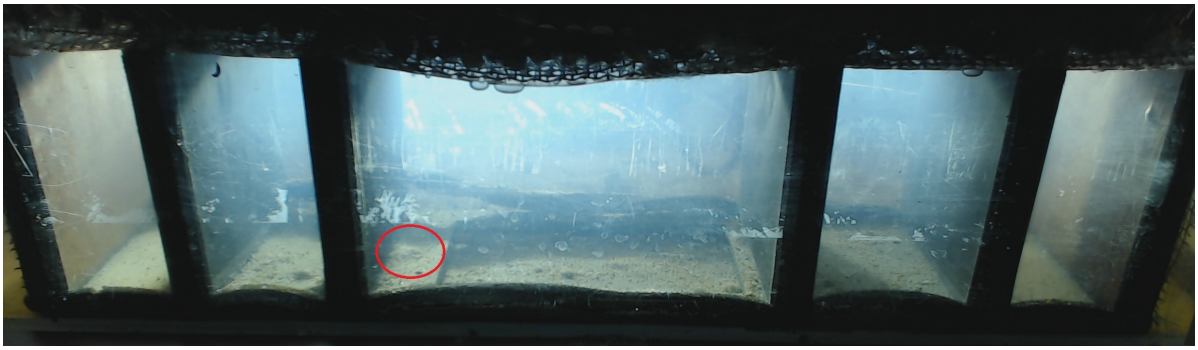

(b) A snapshot of the bottom cells in which erosion was detected, highlighted in the red circle.

Figure 3.16: Detecting erosion visually.

3.8. Installation phase

In order to achieve accurate measurements and make various tests comparable, every test was conducted in the same manner. This paragraph describes the process of setting up a test in a chronological manner. Please note that step 3, 4, 6 and 8 were only valid before the load cell broke down. Photos corresponding to the steps are given in Appendix B.4. On average, it took 4 hours to set up a test.

1. The gravel was washed to ensure an unsaturated filter layer;
2. The bottom cells were placed into the model;
3. The load cell was placed into the bottom cells;
4. The cable of the load cell was guided along the back of Compartment B;

5. Bubble plastic was attached to the front and back of Compartment B to reduce wall effects;
6. The load cell was calibrated in a dry environment;
7. The model was filled with water till the top of the bottom cells;
8. The load cell was calibrated submerged;
9. Two mesh grids were placed on top of the bottom cells;
10. The cables and air hoses of the four pressure sensors were routed through the mesh grids of the division screen;
11. The half of the filter layer was placed;
12. The model was fully filled with water;
13. The pressure sensors were injected with water by the use of a needle while being submerged and fasted to the bar;
14. The filter layer was finished;
15. The model was drained until the water level was equal to the top of the filter;
16. The base layer was placed together with the vertical pressure sensors in case of a combined set-up;
17. The floaters were placed;
18. The model was filled with water while the sensors were calibrated;
19. The top seal was placed in case of a parallel set-up;
20. The recording of the video camera was started;
21. DASYlab was started to capture the output signal;
22. The program of the servo was started;
23. After the tests was finished, the model was cleaned.

3.9. Conducted tests

As discussed before, two types of tests were conducted, namely the parallel and combined tests. Between tests of the same configuration, different parameters were altered to determine the influence of it. This paragraph discusses the test schedule and lists up the alterations over the tests.

After a test was set-up, as explained in Paragraph 3.8, the servo was turned on at the lowest velocity of 0.05 [r/s] for 1 hour. When the initial erosion was settled (if any), the servo was programmed to increase the velocity every 3 hours. The relation between the servo velocity and the plunger period is given in Figure 3.17. The number of cycles per servo velocity is given in Figure 3.18. The velocity segments with corresponding acceleration and deceleration are given in Table 3.3. In every test performed in this study, the plunger was set to each of the settings given in this table until erosion was observed. By increasing the velocity, the water level in Compartment A rose quicker resulting in a larger head difference between the two outer compartments. However, there was a limit to the gradient that could be induced by the plunger. On one hand, the servo had a speed limit. On the other hand, by increasing the plunger velocity waves were induced in de model, which was undesirable for keen measurements.

It was however possible to increase the parallel hydraulic gradient by reducing the filter height. Because of a reduced filter, the discharge $[m^3/s]$ through the filter reduced and a larger head difference was created between the outer compartments. Another reason the decrease the filter height was to make room for the pressure sensors to be aligned vertically in the base layer for the combined set-up.

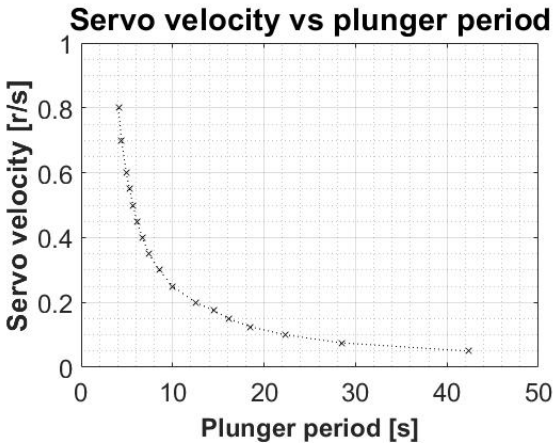

Figure 3.17: The relation between the servo velocity and the plunger period, including a waiting time of 0.5 [s] for a plunger amplitude of 20 [mm].

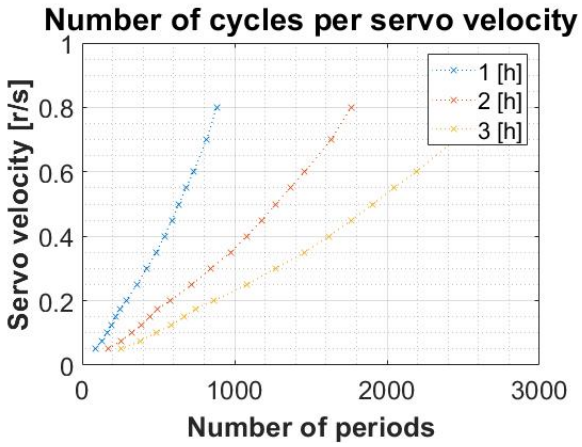

Figure 3.18: Number of cycles per servo velocity, based on the plunger periods given in Figure 3.17. The test were carried out with 2 and 3 [hour] test segments.

Test code	VE_005	VE_010	VE_0125	VE_0150	VE_0175	VE_020	VE_025	VE_030
Velocity [r/s]	0.05	0.01	0.0125	0.015	0.0175	0.02	0.025	0.03
Acceleration [r/s^2]	0.167	0.167	0.167	0.167	0.333	0.5	0.5	0.667
Waiting time [s]	1	0.5	0.5	0.5	0.5	0.5	0.5	0.5

Test code	VE_035	VE_040	VE_045	VE_050	VE_055	VE_060	VE_070	VE_080
Velocity [r/s]	0.035	0.04	0.045	0.05	0.055	0.06	0.07	0.08
Acceleration [r/s^2]	1	1.167	1.333	1.5	1.667	2.	2.5	2.8
Waiting time [s]	1	0.5	0.5	0.5	0.5	0.5	0.5	0.5

Table 3.3: The velocity segments used during the tests.

Furthermore, the stability ratio was altered over the tests by installing various combinations of gravel and sand, as discussed in Paragraph 3.6. The last parameter altered was the degree of initial saturation of base material in the filter layer. An overview of the test conducted is given in Table 3.4.

Test number	**Model configuration**	**Base material**	**Filter material**	**Stability ratio**	**Filter height**	**Degree of saturation**	**Note**
1	Parallel	Sand 2	Gravel 2	6.7	200	Unsaturated	Failed test
2	Parallel	Sand 2	Gravel 2	6.7	200	Unsaturated	Failed test
3	Parallel	Sand 2	Gravel 2	6.7	100	Unsaturated	
4	Parallel	Sand 1	Gravel 1	13.1	100	Unsaturated	
5	Parallel	Sand 1	Gravel 1	13.1	200	Partly saturated	Failed test
6	Parallel	Sand 1	Gravel 1	13.1	200	Partly saturated	
7	Parallel	Sand 2	Gravel 2	6.7	200	Partly saturated	
8	Parallel	Sand 1	Gravel 1	13.1	200	Unsaturated	
9	Parallel	Sand 2	Gravel 3	12.9	200	Unsaturated	
10	Combined	Sand 2	Gravel 3	12.9	150	Unsaturated	
11	Combined	Sand 2	Gravel 3	12.9	150	Unsaturated	
12	Combined	Sand 2	Gravel 2	6.7	150	Unsaturated	
13	Parallel	Sand 3	Gravel 3	5.7	150	Unsaturated	
14	Parallel	Sand 2	Gravel 2	6.7	80	Unsaturated	

Table 3.4: Overview of the tests conducted in this study.

3.10. Analyzing the instrument output

The output of the instruments was analyzed by the use of MATLAB. This paragraph discusses the way the data was analyzed in order to determine the hydraulic gradients.

3.10.1. Filtering the signals

The output of the pressure sensors were filtered to reduce the noise and vibration induced by the plunger and amplifiers. This was done by a Savitzky-Golay filtering, a type of filtering that smooths the signal by convolution. In the top plot of Figure 3.19, an original and filtered pressure sensor output is shown. In the bottom plot, the corresponding frequency spectra are given. It is clearly visible that the two noise and vibration peaks at a frequency of 8.33 and 30.05 [Hz], higher than the plunger frequency of about 0.1 [Hz], were filtered out.

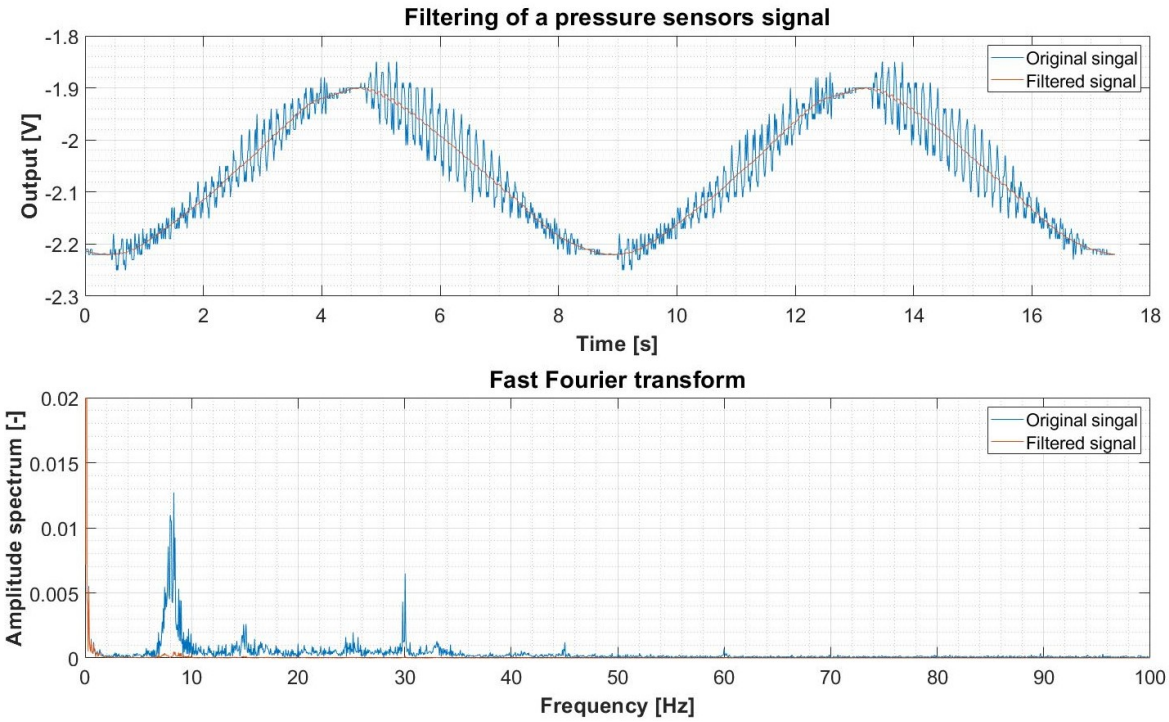

Figure 3.19: A pressure sensor signal before and after filtering. The original signal had peak frequencies at 0.10, 8.33 and 30.05 [Hz].

3.10.2. Calibration

After the output signal was filtered, the signal was calibrated based on the output of the lasers attached of the floaters, as discussed in Paragraph 3.2.

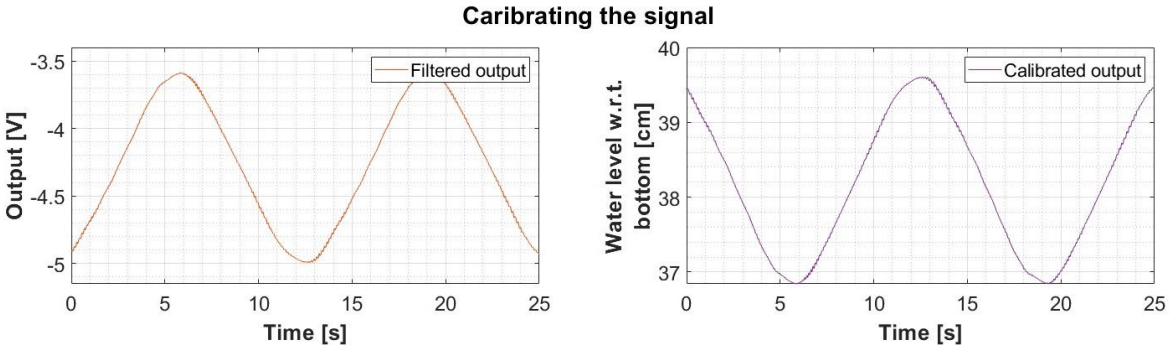

Figure 3.20: A pressure sensor signal before and after calibrating.

3.10.3. De-trending

Although the tests were carried out in a closed environment, namely the Hydraulic Engineering Laboratory of the TU Delft, the model was still exposed to various elements. Because a test took several days, temperature differences, evaporation and even leakage affected the model and instrument outputs. To cope with these effects and to make the results comparable, the calibrated signal was de-trended by subtracting the best-fit line from the data. An example of de-trending is given in Figure 3.21. The calibrated signal (purple) slowly descends over time, best visible in the right bottom part of the graph. The mean of the de-trended signal (blue) is constant.

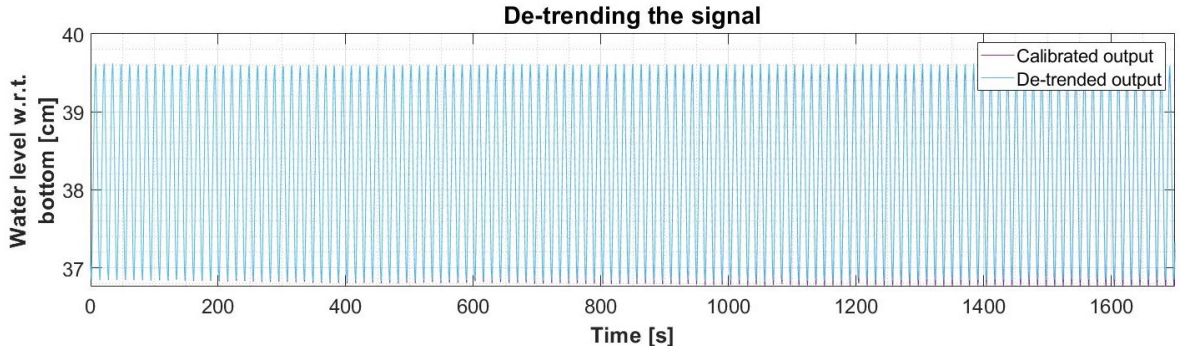

Figure 3.21: A pressure sensor signal before and after de-trending.

3.10.4. Determining the hydraulic gradient

The processed data was used to determine the hydraulic gradients according to Equation 2.1. The parallel gradient was determined by the horizontal aligned pressure sensors and the floaters. The perpendicular gradient was determined by the vertically aligned sensors. A schematically representation of the distances used to determine the gradients is given in Figure 3.22. In Figure 3.23, the location of the used pressure sensor (PS) 1, 2, 3 and 4 is shown.

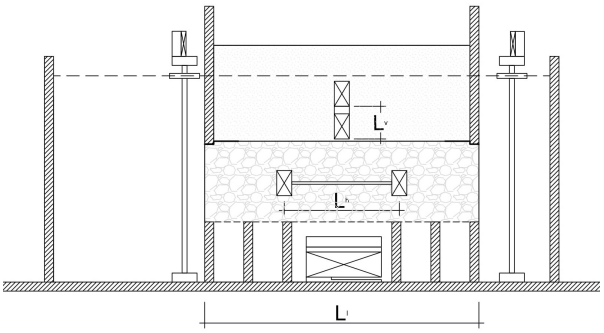

Figure 3.22: A schematically front-view of the distances used to determine the hydraulic gradients.

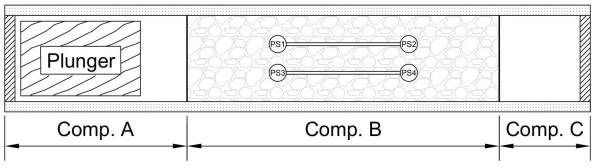

Figure 3.23: A schematically top-view indicating the location of pressure senors 1, 2, 3 and 4 in the filter layer of Compartment B.

In Figure 3.24, an example of the parallel hydraulic gradients are given. As could be seen from this figure is that i_{floater} and $i_{\text{PS3 and PS4}}$ match very well while $i_{\text{PS1 and PS2}}$ has lower peaks. This could be due to the instrument amplifier used for PS1, which was preset to a lower value, resulting in a less accurate signal. This was fixed after noting. Based on comparing the gradient signals, it was manually chosen per test segment which gradient signal was the normative one.

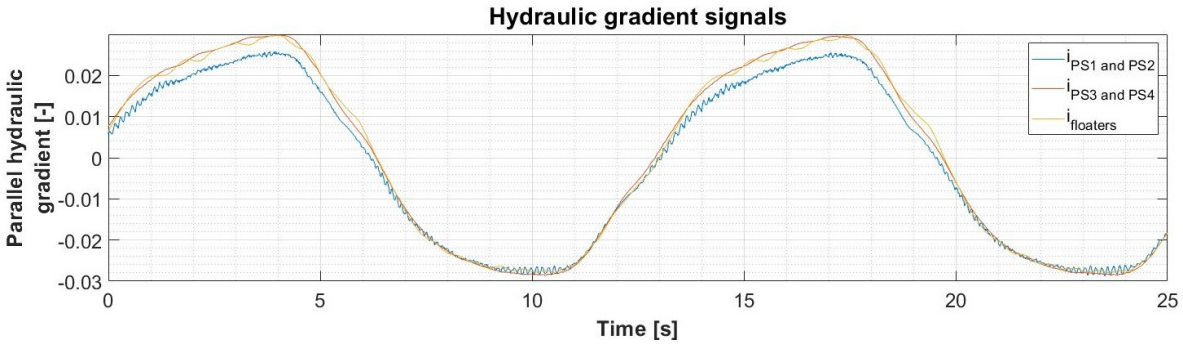

Figure 3.24: Parallel hydraulic gradient determined after calibrating and de-trending the output signals. i_{floater} was determined using the lasers attached to the floaters. $i_{\text{PS1 and PS2}}$ and $i_{\text{PS3 and PS4}}$ were determined based on the pressure signal outputs.

3.10.5. Consistency of the hydraulic gradient

The gradient that was chosen to be normative in the previous section, was analyzed on consistency and quantified. In Figure 3.25, a histogram of the maximum (blue) and minimum (red) hydraulic gradient per plunger period is given. Five bins were used in this histogram. The consistency inversely proportional to the width of the bins. Meaning is this case, that the negative hydraulic gradient was more consistent than the positive one. However, both signal were considered as consistent.

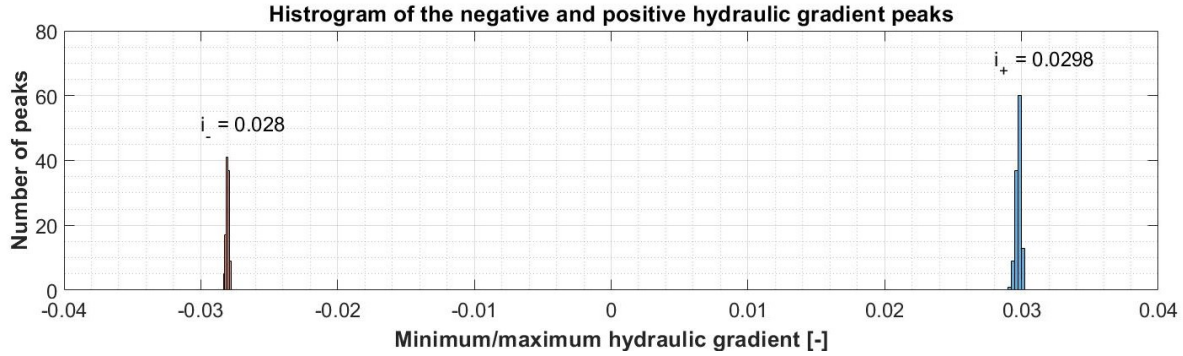

Figure 3.25: A histogram is plotted to determine the consistency of the hydraulic gradient.

3.10.6. Determining the critical hydraulic gradient

To determine the critical hydraulic gradient for a certain test set-up, the signal output of the segment in which erosion occurred was analyzed together with the previous one. The critical hydraulic gradient was defined to be in the range between these values.

4

Test results of the small physical model

In this chapter, the results of the physical model tests are presented and the relationship between the stability ratio and the critical hydraulic gradient is analyzed. In total fourteen tests were conducted, eleven of which were carried out in the parallel set-up and three in the combined set-up. Three tests were performed with a partly sand saturated filter layer, all in the parallel set-up. All other tests were set-up with an unsaturated filter layer. Seven tests were performed with a stability ratio between 6 and 7, the other seven tests had a stability ratio of approximately 13. Erosion was visible in seven tests, no erosion was found in four tests and three tests failed. Besides, tests were conducted with the same stability ratio while using different granular material. This was done to investigate the influence of the characteristic grain size of the base layer on the stability of the total filter layer. An overview of the conducted tests is given in Figure 4.1. In this figure, the number of tests per characteristic is given between brackets. An overview of all tests performed is given in Table 4.1.

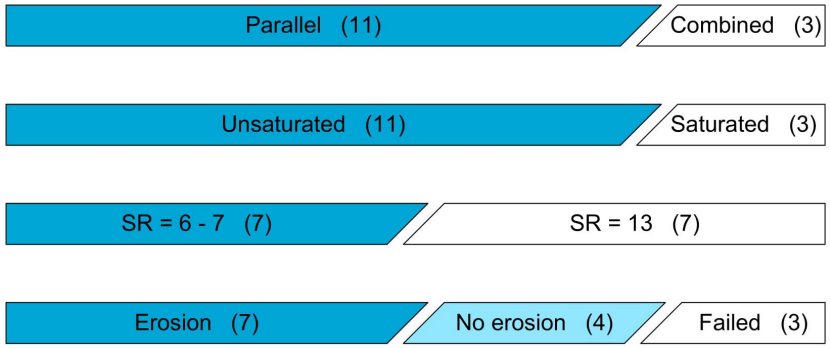

Figure 4.1: A schematic overview of the performed tests. The number of test per characteristic is given between brackets.

The first section of this chapter is about analyzing the induced hydraulic gradient signal. The erosion and corresponding critical hydraulic gradients are discussed hereafter. Lastly, the results are analyzed and compared to each other and the study of Van de Ven (2019).

4.1. Analysis of the hydraulic gradients

In this section, the hydraulic gradients generated by the plunger are analyzed. First, a selection has been made between the parallel hydraulic gradients determined by the pressure sensors and the floaters. Secondly, the phase lag between the plunger and the instrument output is discussed for the parallel and combined configurations. Lastly, the gradients of various tests are compared to each other.

4.1.1. Hydraulic gradients of the pressure sensors and floaters

In the first couple tests, pressure sensors and floaters were used in the parallel set-up. The pressure sensors were more sensitive for external influences, like blockage by sand and temperature differences. Therefore, the output signals of the sensors and floaters were compared to determine the possibility of omitting the pressure sensors in the parallel set-up. Please note that the pressure sensors determining the perpendicular hydraulic gradient could not have been left out of the test rig.

In Figure 4.2, the parallel hydraulic gradients are plotted for 3 plunger signal periods. The gradient signal calculated by the output of the floaters, determined with the original Compartment B length of 52 [cm], gives a slightly higher absolute gradient compared to the pressure sensors. However, by increasing this length to 56 [cm], which was the length of the middle of the compartment due to the bend out of the division screens as illustrated in Figure 5.15, the signal corresponded good to the pressure sensor signal. Therefore, the parallel hydraulic gradients were determined with the value of 56 [cm]. In Figure 4.3 the maximum gradients are plotted against the servo velocities in *Test 6*, showing that the signals were equivalent over the test. Because of this, and because the floaters were more user-friendly, the parallel hydraulic gradients determined by the floaters were used in this chapter. Other small deviations between the pressure sensor and floater signals were probably due to in and out flow effects of Compartment B.

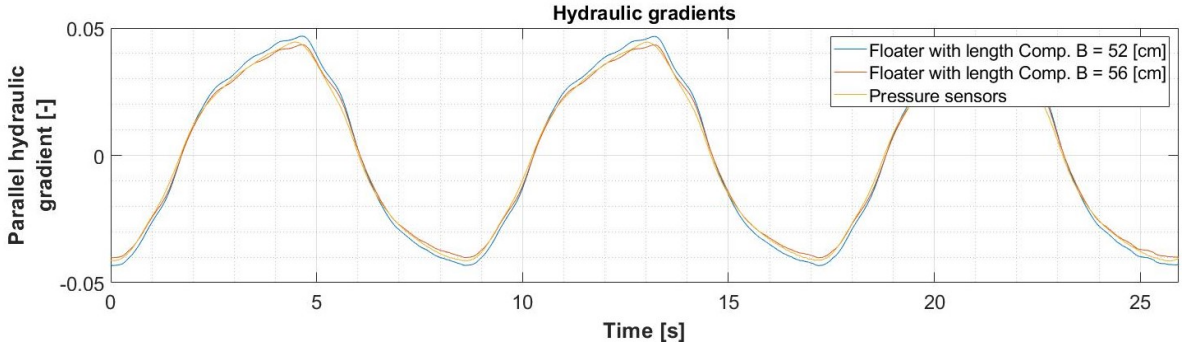

Figure 4.2: Parallel hydraulic gradient signals for Test 6 (SR = 13.1 [-], $d_{50,f}$ = 4.02 [mm] and $d_{50,b}$ = 0.21 [mm]) with VE = 0.30 [r/s].

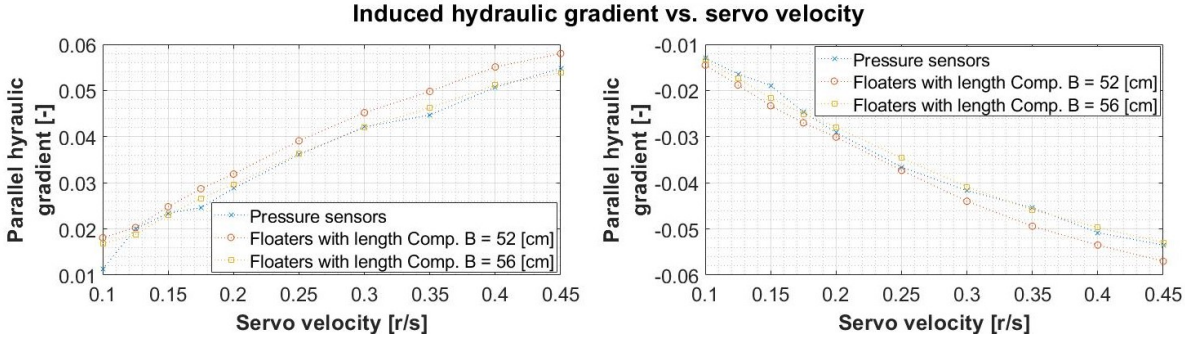

Figure 4.3: Positive and negative parallel hydraulic gradient signals for Test 6 (SR = 13.1 [-], $d_{50,f}$ = 4.02 [mm] and $d_{50,b}$ = 0.21 [mm]) for all servo velocities.

4.1.2. Phase lag between the plunger and the instrument output

As discussed in Chapter 3, the plunger induced water level fluctuations in Compartment A. The water levels in the other compartments of the model followed these fluctuations delayed. The phase lag was due to the laminar, turbulent and inertial resistance the water experienced ny flowing through the granular layer. By increasing the servo velocity, these resistance parameters enlarged as well. In this paragraph, the plunger signal, corresponding water levels and hydraulic gradients are plotted for a parallel and a combined test. Of both test, a low and high servo velocity was used to capture the difference in the water level signals. A constant hydraulic gradient was reached if the pressure change of time ($\frac{\partial P}{\partial t}$) was equal for the compartments of interest, assuming that the distance was set constant. The consistency of the hydraulic signal was discussed in Paragraph 3.10.5.

In Figure 4.4, the output of parallel *Test 8* with VE = 0.1 [r/s] is shown for three plunger signal periods. In Figure 4.5, the same test is shown with VE = 0.6 [r/s]. Next to the graphs, schematic figures corresponding to the signals are shown. One could see that by increasing the plunger velocity, the amplitude of the water level fluctuations in Compartment C was decreased. This is according expectations because of the increased resistance of the flow through the filter layer. This decrease caused a larger pressure differences over the filter layer and so a higher gradient. Furthermore, it is visible that the lower velocity induced a constant gradient while the gradient signal for VE = 0.6 [r/s] was more peaky. This was caused by the fact that the flow reversed before a constant porous flow was achieved. Ideally, the plunger amplitude should be enlarged to reach constant gradients. However, this was not possible due to the dimensions of the model.

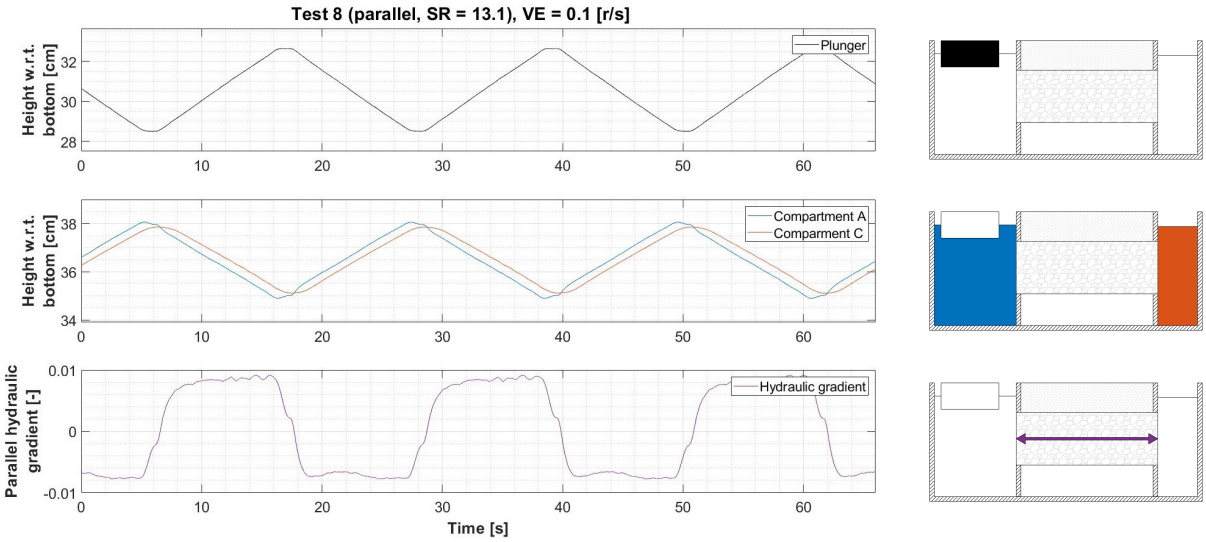

Figure 4.4: Three periods of the plunger, water levels and parallel hydraulic gradient signals of Test 8 (SR = 13.1 [-], $d_{50,f}$ = 4.02 [mm] and $d_{50,b}$ = 0.21 [mm]) with VE = 0.1 [r/s].

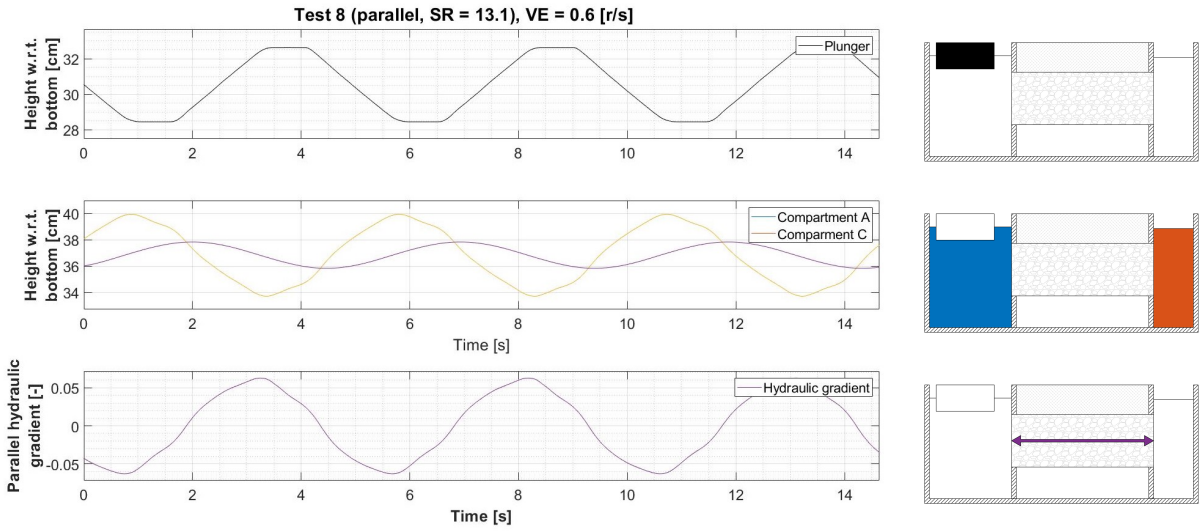

Figure 4.5: Three periods of the plunger, water levels and parallel hydraulic gradient of Test 8 (SR = 13.1 [-], $d_{50,f}$ = 4.02 [mm] and $d_{50,b}$ = 0.21 [mm]) with VE = 0.6 [r/s]

In Figure 4.6 and 4.7, the same type of graphs are plotted for the combined *Test 12*. Similar to the parallel set-up, the induced hydraulic gradients were constant during the plunger movement for the lower servo velocity. By increasing the velocity, higher and more peaky gradients were achieved. Because of the longer waiting time of the plunger signal in the combined set-up, the porous flow stopped and the water levels equalized before the plunger started to move again.

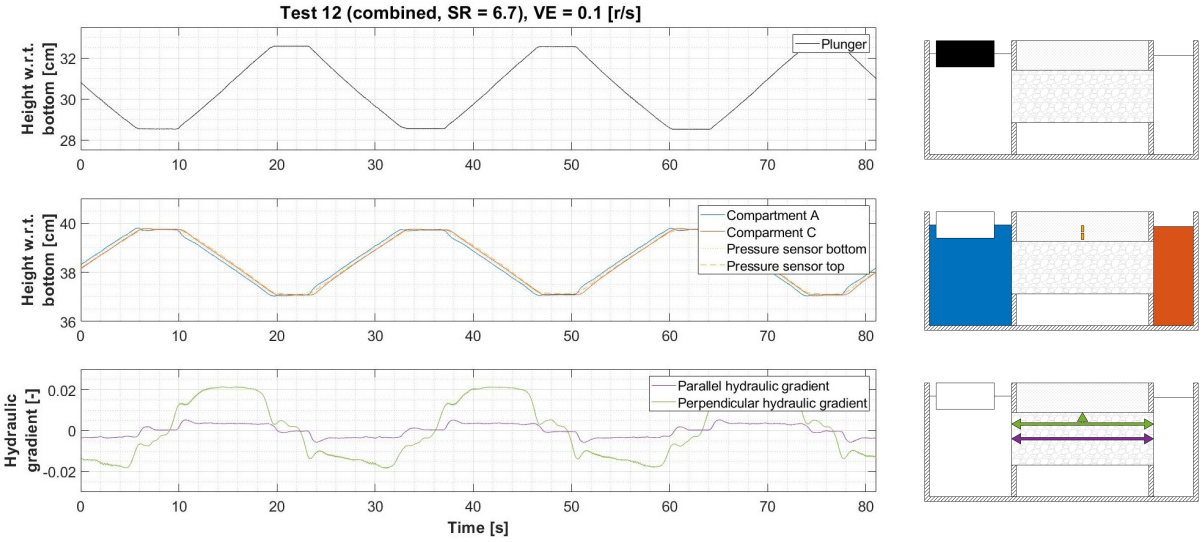

Figure 4.6: Three periods of the plunger, water levels and parallel hydraulic gradient of Test 12 (SR = 6.7 [-], $d_{50,f}$ = 4.89 [mm] and $d_{50,b}$ = 0.48 [mm]) with VE = 0.1 [r/s]

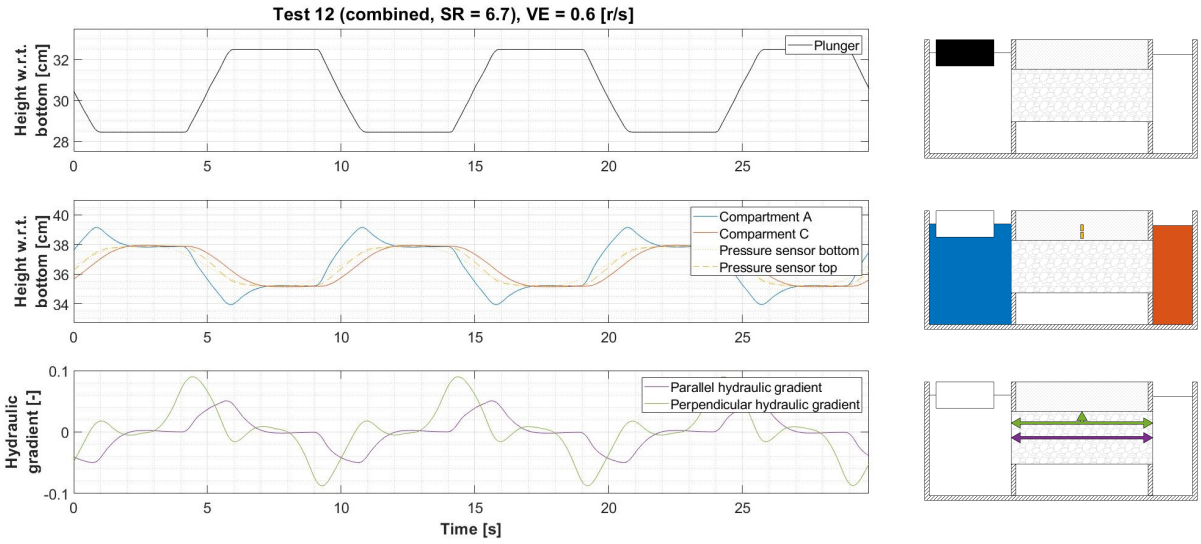

Figure 4.7: Three periods of the plunger, water levels and parallel hydraulic gradient signal of Test 12 (SR = 6.7 [-], $d_{50,f}$ = 4.89 [mm] and $d_{50,b}$ = 0.48 [mm]) with VE = 0.6 [r/s].

4.1.3. Servo velocity and the forced hydraulic gradients

Due to various parameters of the filter installed in the model, the same servo velocity induced different hydraulic gradients. The parameters that were mainly of interest are:

- The permeability of the filter layer (parallel gradient) and the base layer (perpendicular gradient). The permeability was mainly influenced by:
  - The d_{50} of the layer of interest;
  - The saturation of sand in the pores of the filter layer (parallel gradient);
  - Porosity.
- Filter height (parallel gradient).

In Figure 4.8, the servo velocities and the corresponding hydraulic gradients are plotted for 3 parallel tests. These tests were selected because of the different gravel used while having a constant filter height of 200 [mm]. Visible is that in the test with the largest $d_{50,f}$, *Test 9*, the lowest hydraulic gradient was induced. This is according expectations since larger grains have a higher permeability. Despite a lower $d_{50,f}$ was used in *Test 8* compared to *Test 7*, a higher gradient was reached during the latter. This is due to the fact that the filter layer in *Test 7* was partly saturated, what resulted in a lower permeability. Moreover, it is visible that the gradients in *Test 8* (SR = 13.1) increased quicker compared to the other two. This could be due to the change of model characteristics while running the test. Settlement of the granular material and erosion of the base layer into the filter layer influenced the generated gradients.

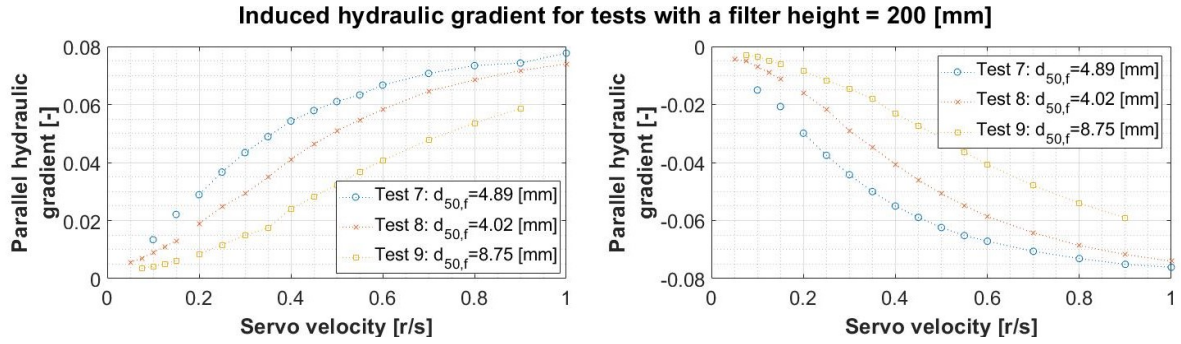

Figure 4.8: Parallel hydraulic gradient versus the servo velocity for 3 tests with a filter height of 200 [mm].

In Figure 4.9, two parallel tests are plotted with a different filter height. Higher gradients were reached in the test with the smaller filter height, as expected.

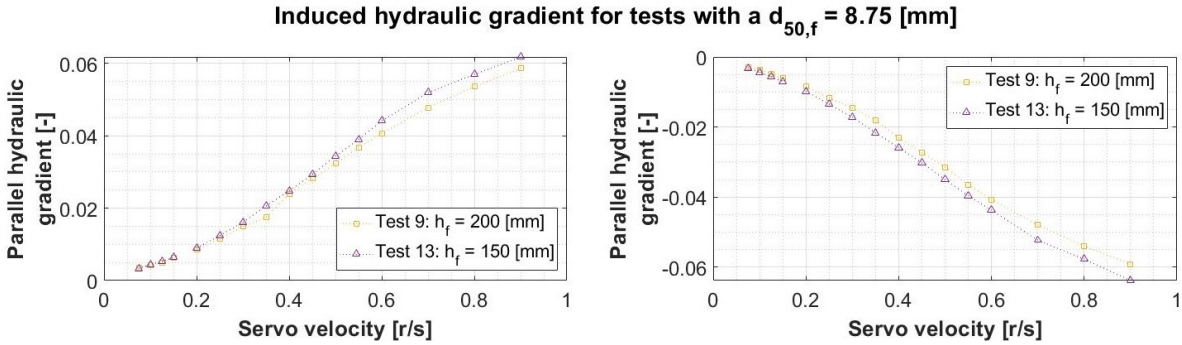

Figure 4.9: Parallel hydraulic gradient versus the servo velocity for 2 tests with $d_{50,f}$ = 8.75 [mm] and a filter height (h_f) of 200 and 150 [mm].

In Figure 4.10, two combined tests are plotted. In the left graph, the parallel gradients are shown. Visible is that the use of larger gravel resulted in lower parallel hydraulic gradients. In the right graph, the perpendicular gradients are shown. However both set-ups had the same sand in the base layer, the perpendicular gradients induced were different. This was probably due to the placement and settlement of the base layer, influencing the permeability.

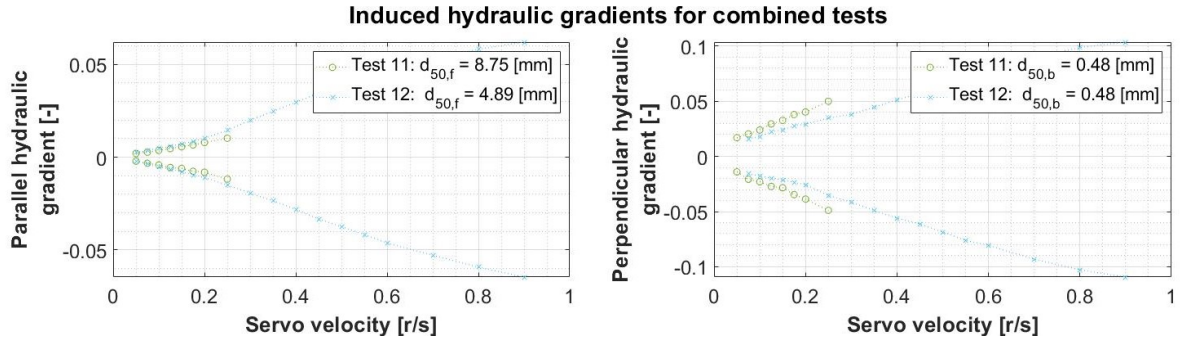

Figure 4.10: Parallel and perpendicular hydraulic gradient versus the servo velocity for 2 combined tests.

4.2. Erosion and corresponding critical hydraulic gradients

Erosion was detected visually by the use of a video camera in front of the bottom cells, as described in Paragraph 3.7. Because blind-spots were formed by the bottom cells, it was manually checked if no erosion was missed by the camera. Moreover, it was checked if erosion occurred during moments without plunger movement. This could have happened after a segment was finished, but before a new segment was started. No erosion was detected during these periods. Furthermore, no channel effects were observed as was described by Van de Ven (2019).

Not every test resulted in erosion. Some tests failed because sand infiltrated the outer compartments, despite the use of geotextile (Figure 4.11). For other tests the hydraulic gradient induced was not sufficient to cause erosion. For the tests with erosion, the hydraulic gradient was determined for the segment in which the erosion occurred ($i_{cr,\parallel+}$ and $i_{cr,\perp+}$) and the segment prior to it ($i_{cr,\parallel-}$ and $i_{cr,\perp-}$). The critical hydraulic gradient was defined as the range between these values. For the tests without erosion, the hydraulic gradient induced by the highest servo velocity was determined ($i_{cr,\parallel-}$ and/or $i_{cr,\perp-}$) forming a lower limit of the critical hydraulic gradient. The results are given in Table 4.1. In the next section, the results are analyzed and compared to each other and a previous study of Van de Ven (2019).

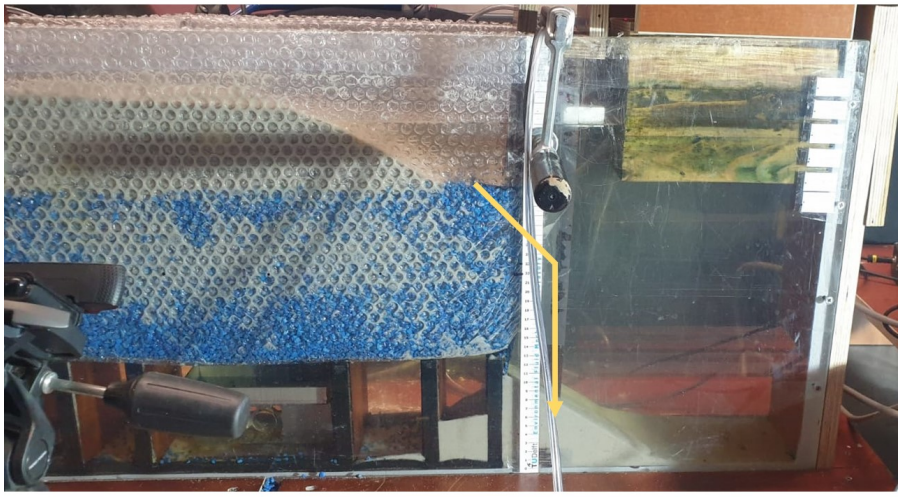

Figure 4.11: A failed test in which sand eroded through the division screen into Compartment A.

Test number	Configuration	Stability ratio	$i_{cr,\parallel-}$	$i_{cr,\parallel+}$	$i_{cr,\perp-}$	$i_{cr,\perp+}$	Note
1	Parallel	6.73	N.a.	N.a.	N.a.	N.a.	Failed test
2	Parallel	6.73	N.a.	N.a.	N.a.	N.a.	Failed test
3	Parallel	6.73	0.071	N.a.	N.a.	N.a.	No erosion
4	Parallel	13.09	0.053	0.061	N.a.	N.a.	Erosion at VE = 0.4
5	Parallel	13.09	N.a.	N.a.	N.a.	N.a.	Failed test
6	Parallel	13.09	0.000	0.015	N.a.	N.a.	Erosion in first segment: VE = 0.1
7	Parallel	6.73	0.029	0.045	N.a.	N.a.	Erosion at VE = 0.3
8	Parallel	13.09	0.055	0.058	N.a.	N.a.	Erosion at VE = 0.6
9	Parallel	12.86	0.048	0.054	N.a.	N.a.	Erosion at VE = 0.8
10	Combined	12.86	0.000	0.002	0.000	0.010	Erosion in first segment: VE = 0.05
11	Combined	12.86	0.003	0.004	0.021	0.024	Erosion at VE = 0.1
12	Combined	6.73	0.063	N.a.	0.107	N.a.	No erosion
13	Parallel	6.73	0.077	N.a.	N.a.	N.a.	No erosion
14	Parallel	5.74	0.083	N.a.	N.a.	N.a.	No erosion

Table 4.1: Overview of the critical hydraulic gradients per test.

4.3. Stability ratio versus the critical hydraulic gradient

To broaden the knowledge on inversed geometrically open granular filters, a correlation between the main factor causing erosion, the critical hydraulic gradient (i_{cr}), and the main resistance parameter, the stability ratio $\left(\frac{d_{15,f}}{d_{85,b}}\right)$ was analyzed. Firstly, the unsaturated parallel test results are discussed. Secondly, the partly saturated parallel test results are discussed. Thirdly, the combined tests are discussed and the parallel component of the combined tests are compared to the parallel test results. Lastly, the results of this study are compared to the previous results of the research line.

4.3.1. Unsaturated parallel test results

The unsaturated parallel test results are plotted in Figure 4.12. In this plot, the test characteristics are noted as following:

- The unsaturated parallel tests 3, 4, 8, 9, 13 and 14 are plotted in blue;
- The grain size of the base material used in a test is marked by a circle, diamond or hexagon, as listed in the legend under *Grain size*;
- The type of results that was reached in a test is illustrated by the use of a range bar (indicating the range of i_{cr}) or dashed line (indicating the bottom limit of i_{cr}), as listed in the legend under *Type of result*.

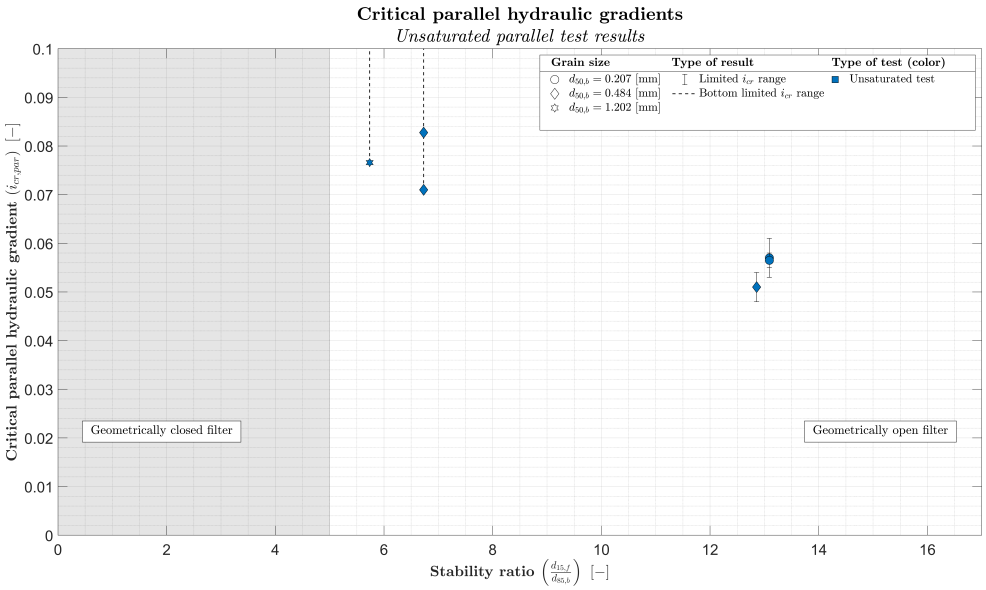

Figure 4.12: The relation between the stability ratio and the critical hydraulic gradient of the unsaturated parallel tests.

As could be seen by the blue markers in Figure 4.12, three tests resulted in erosion and for three tests the parallel hydraulic gradient induced was insufficient to cause erosion. Therefore, the results are inadequate to compose an empirical formula to determine a stable stability ratio for a known hydraulic gradient. The following observations were made based on the unsaturated parallel tests:

- **Erosion**
  The model was unable to induce hydraulic gradients sufficient enough to cause erosion for the stability ratios (SR) between 6 and 7. For $SR \approx 13$, results were found for $i_{cr,\parallel} = 0.048 - 0.061$, being the outer limit of the range bars.

- **Filter height**
  In the second parallel test that was performed with $SR = 6.73$, the filter height was reduced in order to achieve higher gradients. As can be seen in Figure 4.12, the maximum induced parallel hydraulic gradient increased from 0.071 to 0.083. One could argue that reducing the filter height influenced the detection of erosion since the distance for the sand eroding through the filter layer into the bottom cells is decreased. Therefore, two tests were carried out with $SR = 13.1$, each with different filter heights. *Test 4* was conducted with a filter height of 100 [mm]. *Test 8* was conducted with a filter height of 200 [mm]. As can be seen from Figure 4.12, both tests give about the same critical hydraulic gradient and the markers are in each others range bars. It is recommended to perform more tests to fully exclude the effect of the filter height on the erosion detection. However, in the scope of this study it seemed that the filter height did not influence the critical hydraulic gradient determined.

- **Characteristic grain size of the base material**
  De Graauw et al. (1983) stated that the grain size of the base material influences the critical gradient if a constant stability ratio is taken, as discussed in Paragraph 2.3.2. Therefore, tests were conducted with an approximately equal SR while using different granular materials:

$$\frac{d_{15,b}}{d_{85,f}} = \frac{4.16}{0.62} = 6.73 \qquad \frac{d_{15,b}}{d_{85,f}} = \frac{3.29}{0.25} = 13.1$$

$$\frac{d_{15,b}}{d_{85,f}} = \frac{7.95}{1.39} = 5.74 \qquad \frac{d_{15,b}}{d_{85,f}} = \frac{7.95}{0.62} = 12.9$$

  Based on the parallel tests with a SR between 6 and 7, not many conclusions could be drawn since the point of erosion was not found. For $SR \approx 13$, erosion was found during three tests. Two of which were performed with $d_{50,b} = 0.207$ [mm] and one with $d_{50,b} = 0.484$ [mm]. The range bars of the determined critical hydraulic gradients overlap each other in Figure 4.12. Based on this, it is concluded that the grain size of the base material did not (significantly) influence the critical hydraulic gradient if a constant stability ratio was taken. However, it is recommended to perform more tests to determine the influence of $d_{50,b}$ on i_{cr}.

4.3.2. Partly saturated parallel test results

The partly saturated parallel test results are plotted with the unsaturated results, as discussed above, in Figure 4.13. In this plot, additional test characteristics are noted as following:

- The partly saturated parallel test 6 and 7 are noted in yellow;
- The type of results that indicates an upper limit of the hydraulic gradient is illustrated with a dotted line, as listed in the legend under *Type of result*.

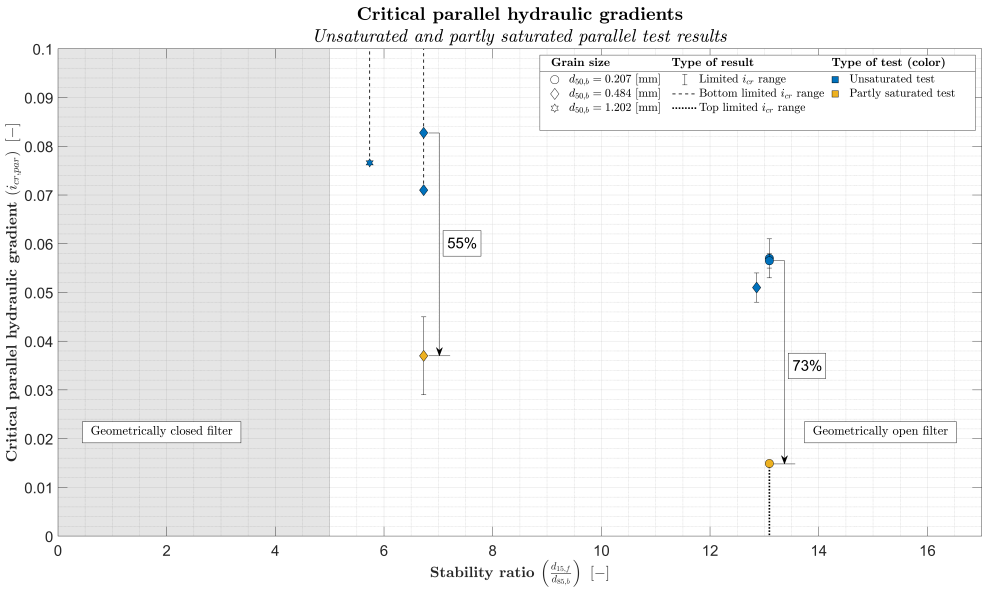

Figure 4.13: The relation between the stability ratio and the critical hydraulic gradient of the unsaturated and partly saturated parallel tests.

During testing, it was noted that the re-use of filter material in a new test set-up – without washing the sand out of the gravel – resulted in lower critical hydraulic gradients. Three parallel tests with partially sand saturated filter layers were conducted. Two tests had erosion and one test failed. Out of the two test with erosion, one test had erosion in the first segment, resulting in a top limited i_{cr}. A lower critical parallel hydraulic gradient was found for both partially saturated tests compared to the unsaturated tests:

- For $SR = 6.7$, the i_{cr} reduced from a minimum of 0.083, the bottom value of i_{cr} in the unsaturated tests, to $i_{cr} = 0.037$, the middle of the range bars in the partly saturated parallel test. This is a minimum reduction of 55%;
- For $SR = 13.1$, the i_{cr} reduced from 0.057, the middle of the range bar in the unsaturated tests, to maximum i_{cr} 0.015, the upper limit of i_{cr} in the partly saturated parallel test. This is a minimum reduction of 73%.

An explanation for this reduction is that the erosion detected in the bottom cells, strictly consisted of sand grains that were initially present in the filter layer and had a lower critical gradient to erode into the bottom cells compared to sand originating from the base layer. A larger critical gradient of the latter could be explained by an arching effect increasing the stability of the filter structure as discussed in Paragraph 2.4. Morover, a difference in packing of the sand could have resulted in a different i_{cr}. A test with a known volume of sand mixed into the filter layer is recommended, which was due to a lack of time not possible to conduct during this study. One could gradually increase the hydraulic gradient until erosion is detected. By comparing the volume of sand in the bottom cells at the end of the test with the known sand volume initially present in the filter layer, the statement could be examined.

Another explanation is that the sand that is present in the filter layer reduced the critical hydraulic gradient of the total inversed granular filter structure, by forming channels in the filter layer for the base material

to erode through, as discussed by Van de Ven (2019). This statement could be examined by the use of an unsaturated test. The plunger period should be decreased until erosion in visible. Now the filter layer is partially saturated, one could increase the plunger period again, resulting in a lower hydraulic gradient. If the erosion continues, one could conclude that the critical hydraulic gradient for a saturated filter is smaller compared to an unsaturated filter.

Projecting this reduction of i_{cr} for partly saturated granular filters to the stability of structures built in reality, could mean that:

1. Assuming that the construction of the real structure causes more initial saturation compared to physical modeling, due to the use of larger equipment and volumes, a lower stability of such a structure compared to the unsaturated parallel tests could be expected.

2. The stability of the real structure could reduce over time. If a storm occurs with $i_{storm} > i_{cr}$, base material could erode into the filter layer, saturating the latter. This could reduce the stability of the structure, meaning that erosion could occur for smaller storms from now.

4.3.3. Unsaturated combined test results

In Figure 4.14, de results of the combined tests 10, 11 and 12 are given together with the path of the induced hydraulic gradient during the tests. The markers indicate where erosion was first noted. In the first combined test, erosion was detected in the first segment. This resulted in an upper limit of the i_{cr}, which will be located in the dotted outlined gray area. In the second test, erosion was detected. In the last test, no erosion was visible and therefore a lower limit of the i_{cr} was found, which is allocated in the dashed outlined area.

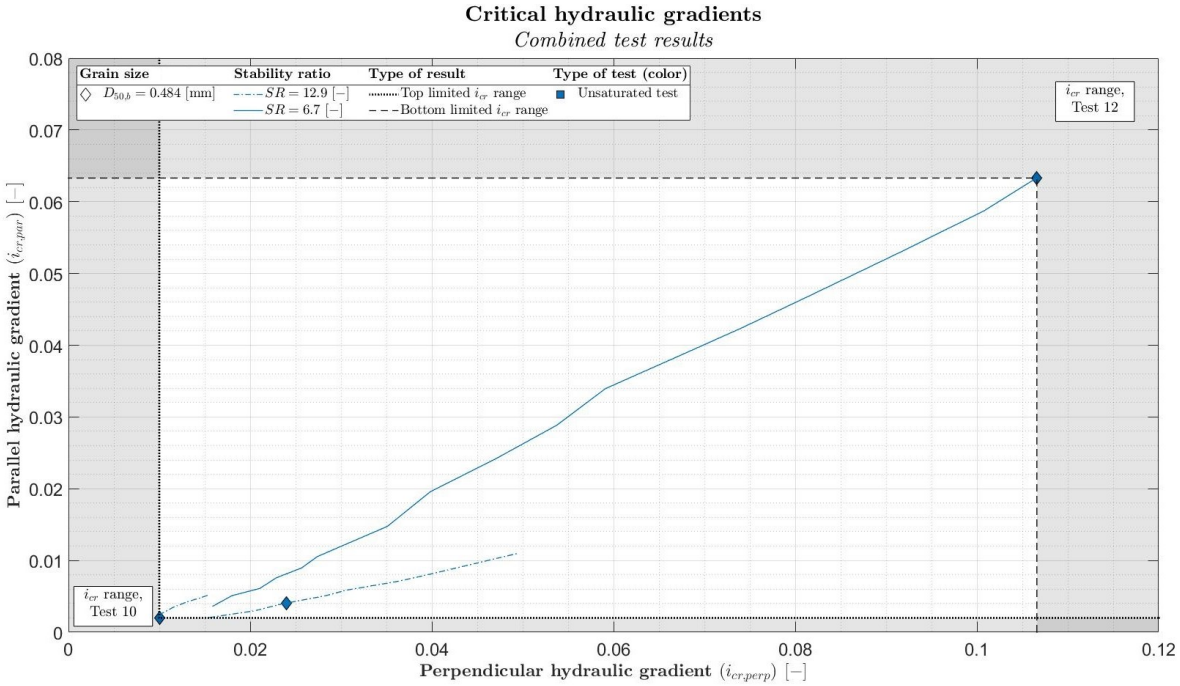

Figure 4.14: Parallel and perpendicular components of the hydraulic gradient of the combined tests. The markers indicate where erosion was first noted. Two different stability ratios were tested, one test did not result in erosion.

In order to put the combined test results into perspective, the parallel components of i_{cr} are plotted in light blue markers – together with the results of the parallel tests – in Figure 4.15. Lower critical hydraulic gradients were found in the combined tests compared to the parallel tests:

- For SR = 12.9, the i_{cr} reduced from 0.051, the middle of the range bars in the unsaturated test, to i_{cr} = 0.0035, the middle of the range bars of the combined test in which erosion was not found in the first segment. This is a reduction of 93%.

The decrease of i_{cr} could have been due to the difference in flow pattern between the two configurations, resulting in a lower i_{cr} by breaking the arching effect. In addition, the way the combined model was set-up could have resulted in a lower critical gradient. In contrast to the parallel test, pressure sensors were placed in the base layer. The sensors needed to be submerged for calibration, resulting in that the base layer was placed in wet conditions. This could have caused more initial infall compared to the parallel test, resulting on their turn in a lower critical hydraulic gradient, as discussed above.

In reality, the structure is subject to a combination of parallel and perpendicular gradients. Therefore, if the combined loading condition leads to a reduced i_{cr}, smaller i_{cr} are expected for these filter structure in reality compared to the unsaturated parallel tests.

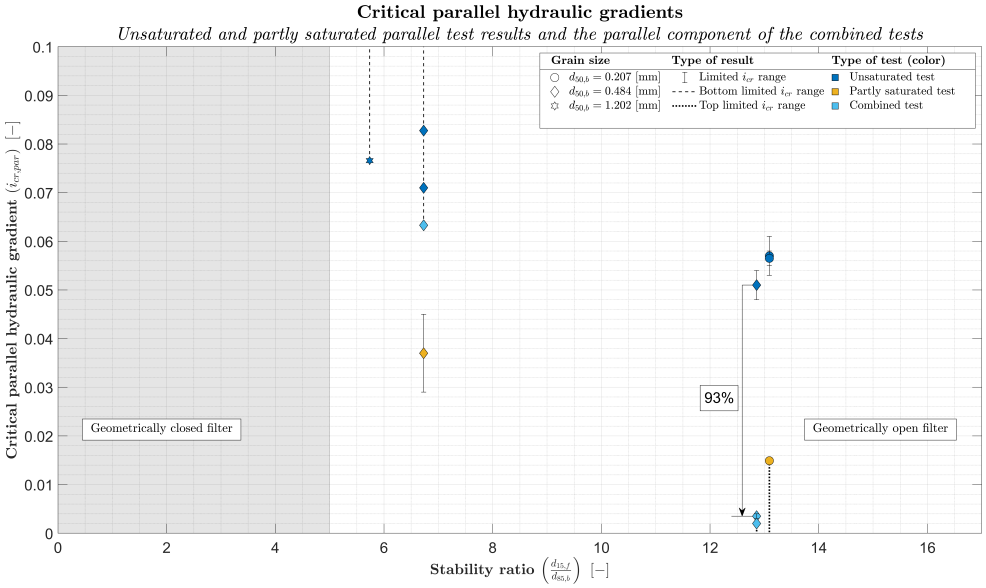

Figure 4.15: The parallel component of the critical hydraulic gradients of the combined tests are plotted together with the results of the unsaturated and partly saturated parallel tests. Visible is that the parallel critical gradient of the combined tests were lower compared to the parallel tests.

4.4. Comparison of the results to previous research

The parallel test results, as discussed above, are plotted together with the parallel test results of Van de Ven (2019) – marked in light gray – in Figure 4.16. The perpendicular results of the same study are plotted together with the perpendicular components of the combined tests in Figure 4.17.

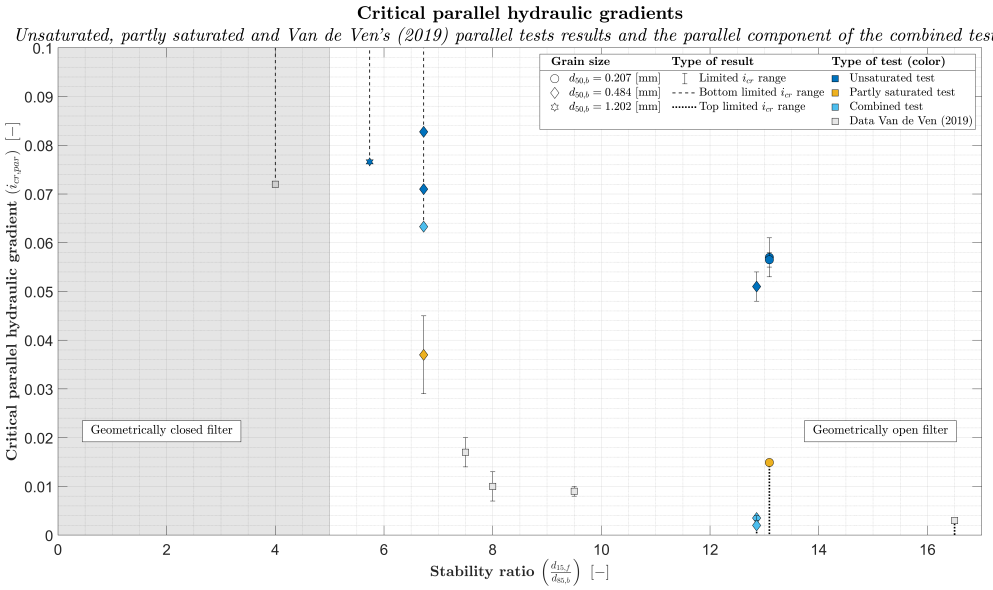

Figure 4.16: The results of the unsaturated and partly saturated parallel tests are plotted with the parallel component of the combined test results and the parallel test results of Van de Ven (2019).

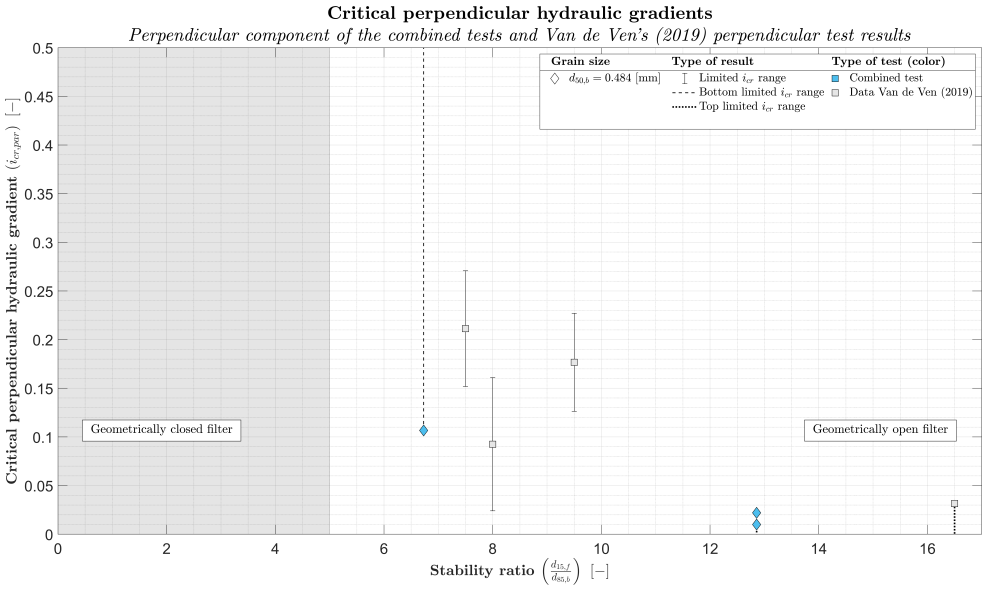

Figure 4.17: The perpendicular component of the combined test results are plotted together with the perpendicular test results of Van de Ven (2019).

In Figure 4.16, it is clearly visible that the critical parallel hydraulic gradients found in the unsaturated and partly saturated tests of this study were significantly higher compared to the results of Van de Ven (2019). The parallel and perpendicular components of the combined tests were more in line with the results of Van de Ven. The difference between the results of the two studies, both using the same model, could have been due to:

- **Determination of the gravel grading curves**
  In this study, the grading of the gravel was determined by weighing about 1000 grains per type of gravel. This eliminated the need for multiple sieves to determine an accurate grading curve. Moreover, the curve created was continuously since the data was not determined based on certain mesh width intervals, as was the case with sieving. The difference in method could have lead to different stability ratios for the same type of gravel. However, the effect of this on the results was expected to be minimal.
- **Initial sand saturation of the filter layer**
  Initial saturated filter layers resulted in lower critical hydraulic gradients, as shown in Figure 4.13. An explanation for the difference between the results of Van de Ven (2019) and this study, could be that the filter layers of Van de Ven were more saturated. This could have been a result of:
  - **Cleaning of the gravel**
    Before setting up a test, it was made sure that the gravel was sand free by washing the grains extensively. To which extend the gravel was sand free could differ between Van de Ven (2019) and this study.
  - **Initial infall of the base material**
    A large difference was found in the initial infall of base material into the bottom cells between the tests of Van de Ven (2019) and this study. An example of the initial infall of Van de Ven (2019) is given in Figure 4.18a and the initial infall of *Test 9* of this study in Figure 4.18b. As can be seen in Figure 4.18a is that no bubble plastic is visible at the bottom of Van de Ven's filter layer. The absence of bubble plastic along the lower part of the filter layer could be the reason of the initial infall differences. Furthermore, the size and grading of the filter layer affects the reduction of wall effects along the model.
- **Top seal**
  As discussed in Paragraph 4.3.3, the combination between a parallel and perpendicular gradient could lower the i_{cr} of the filter structure. If the seal used by Van de Ven on top of the base material did not fully close off Compartment B, a perpendicular gradient could have occurred, lowering the determined critical parallel hydraulic gradient.

(a) Initial infall of *Test Ref_8.0_4* by Van de Ven (2019).

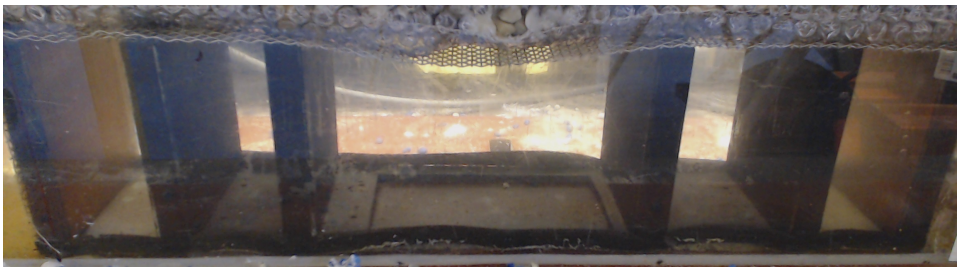

(b) Initial infall of *Test 9*.

Figure 4.18: Initial infall differences between Van de Ven (2019) and this study.

4.5. Putting the critical hydraulic gradients into perspective

Van de Ven (2019) made an estimation of the hydraulic gradient occurring in a breakwater by using the numerical model OpenFOAM, as discussed in Paragraph 2.1.4. It should be noted that this model is not yet scientifically verified, but was used to give an estimation of the occurring pressures. In this paragraph, the achieved results are compared to hydraulic gradients occurring in a breakwater according to Van de Ven (2019).

The critical hydraulic gradients of the parallel tests and the parallel component of the critical hydraulic gradients of the combined tests are given in Figure 4.19. On the x-axis, the critical hydraulic gradient is given. On the y-axis, the depth of the filter with respect to mean sea level is shown. The 2% highest gradients of the OpenFOAM model are marked by red dots. One could see that the gradients occurring in the filter decrease with increasing depth. According the OpenFOAM data, all parallel tests and the combined Test 12 form a stable system. Test 10 and 11 could be stable, depending on the depth of the filter.

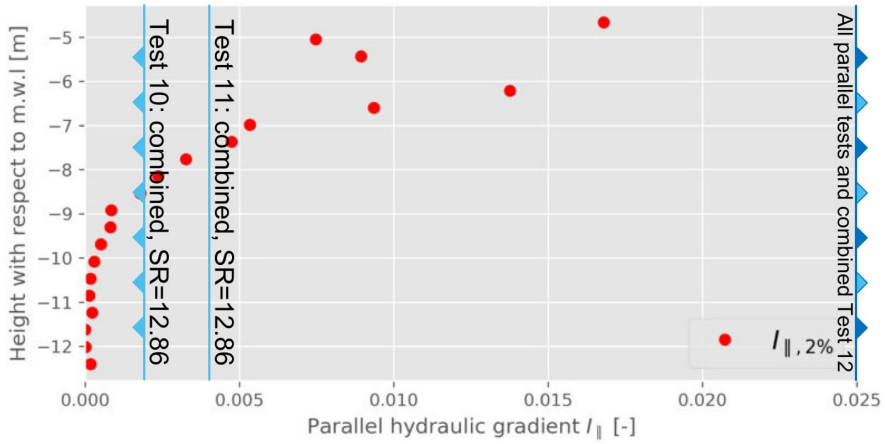

Figure 4.19: The critical parallel hydraulic gradients of the parallel tests (dark blue) and the parallel component of critical gradient the combined tests (light blue), determined in this study compared to the gradient occurring in a breakwater, estimated by Van de Ven (2019) in OpenFOAM.

In Figure 4.20, the perpendicular component of the critical hydraulic gradients of the combined tests are given. The perpendicular components determined by physical modeling were always lower compared to the OpenFOAM data. This means that there was never a stable situation.

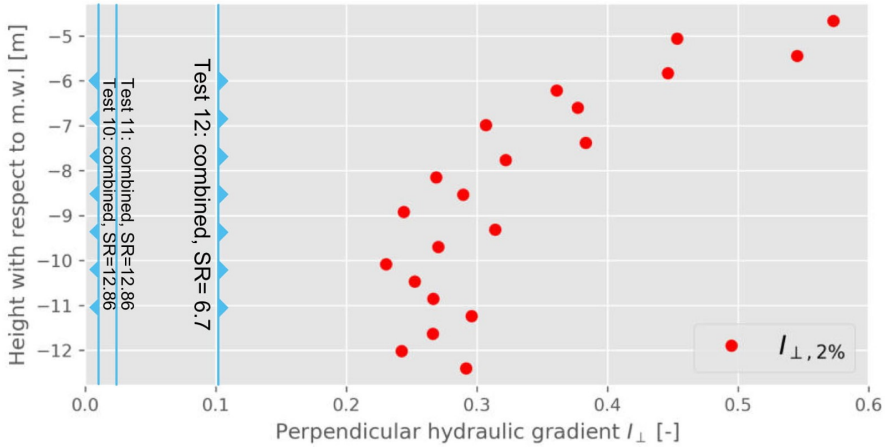

Figure 4.20: The perpendicular component of the critical parallel hydraulic gradients determined by the combined tests in this study compared to the gradient occurring in a breakwater, estimated by Van de Ven (2019) in OpenFOAM.

4.6. Conclusion

In this paragraph, the conclusions of the physical model test results are listed.

- The floaters, custom designed to measure the water levels of Compartment A and C continuously, functioned properly and were therefore used to determine the parallel hydraulic gradients of the parallel and combined configuration;
- The hydraulic gradients generated by low velocity plunger signals were consistent, reliable and constant during constant movement of the plunger for both the parallel and the combined set-up. The hydraulic gradient signals induced by short plunger periods were more peaky shaped but nevertheless consistent and reliable;
- For tests with a stability ratio between 6 and 7, the model and plunger were not capable of causing erosion and therefore no critical hydraulic gradient was determined. For tests with $SR \approx 13$, erosion was detected and critical hydraulic gradients were determined;
- It seemed that the filter height used in a test did not influence the critical hydraulic gradient of a particular filter structure;
- It seemed that a larger characteristic grain size of the base layer did not (significantly) lower the critical hydraulic gradient of a filter structure;
- Initial saturation of the filter layer by base material reduced the critical hydraulic gradient of the filter structure. This could be due to (1) initial infall was observed or that (2) the saturation reduced the overall stability of the filter structure;
- The unsaturated and partly saturated parallel test results were higher compared to the combined tests and the results of Van de Ven (2019);
- The majority of filter tested in this study were stable for the parallel hydraulic gradients occurring in a breakwater determined by Van de Ven (2019) in OpenFOAM. For the perpendicular gradient, no stable situation was found.

5

Numerical model

As stated in Chapter 2, the inversed open filter could be more stable when a superimposed load is applied. Therefore, it would result in a conservative design if the influence of the superimposed load is neglected. In order to gain more knowledge about this phenomenon, a goal of this thesis was to design and construct a physical model that could cope with the superimposed load of 10 meters sand column. In order to design the new model in Chapter 6, the test rig was modeled numerically. The design of Van de Ven (2019), as described in Chapter 3, was taken as starting point. It was chosen to keep the principle of this type of model since the parallel and perpendicular (and therefore combined) set-ups could be tested in the same model by closing off certain boundaries.

Firstly, the parameters that were used to describe the model numerically are given in a schematic representation of the model. Secondly, a description of how the model was programmed numerically is given in a step-by-step approach. As starting point, the movement of the plunger is described according to Paragraph 3.5, whereafter the water level of the compartment in which the plunger is attached is discussed. Using a porous flow through the model, the water level in Compartment C and ground water level in Compartment B are described. Finally, the calibration and validation of the numerical model based on physical model tests conducted in this study is discussed.

5.1. Numerical model description

The main goal of the numerical model is to provide a base to design the new physical model in Chapter 6. The numerical model was programmed 2-dimensionally. The parameters used to describe the model are given in Figure 5.1 and listed below.

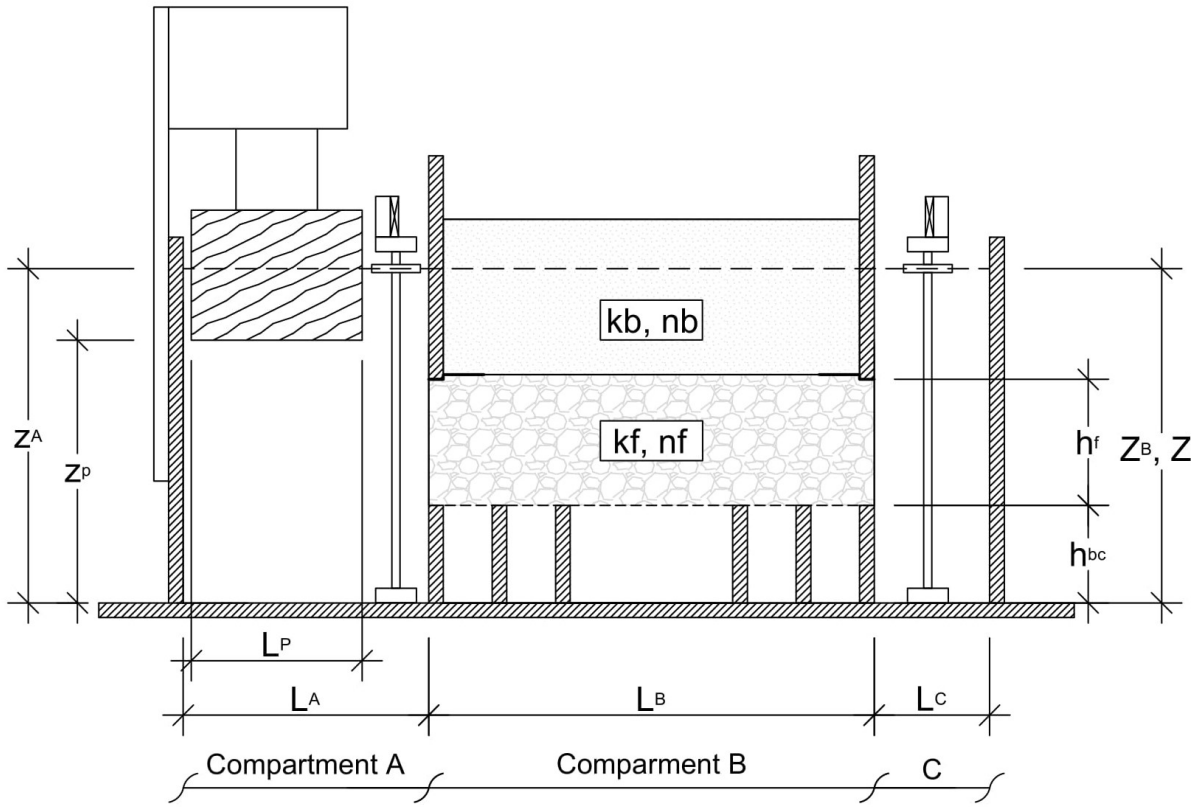

Figure 5.1: Parameters used to describe the model numerically.

in which:

- z_A: Water level in compartment A [mm]
- z_B: Groundwater level in compartment B [mm]
- z_C: Water level in compartment C [mm]
- z_p: Distance between the bottom of the plunger and the bottom of the model [mm]
- h_f: Filter height [mm]
- h_bc: Bottom cells height [mm]
- L_A: Length of compartment A [mm]
- L_B: Length of compartment B [mm]
- L_C: Length of compartment C [mm]
- L_p: Length of the plunger (converted to 2D by using the 3D blocking rate in Comp. A) [mm]
- k_b: Permeability of the base layer [m/s]
- n_b: Porosity of the base layer [-]
- k_f: Permeability of the filter layer [m/s]
- n_f: Porosity of the filter layer [-]

5.2. Movement of the plunger

All of the three model configurations – parallel, perpendicular and combined – started by the movement of the plunger which induced the porous flow through the filter layer. The plunger signal was set to a saw-tooth shape, corresponding to the computer controlled movement of the servo, as described in Paragraph 5.2. The acceleration and deceleration were neglected for simplicity reasons. By doing so, the plunger signal, and therefore the water level signals, were shaped more angular. The signal was described by the following parameters:

- T: Period [s]
- t_w: Waiting time [s]
- $z_{p,0}$: Initial height [mm]
- A_p: Amplitude [mm]

The plunger signal used in the physical model tests depended on the model configuration and the materials used in the filter and base layer. For granular material with a high permeability, a constant gradient was achieved if the plunger had a constant velocity. Hence, the plunger signal had a short waiting time (t_w), like the solid line in Figure 3.5. For (very) low permeable materials, the opposite is true. In this case, the water level of compartment B did not adapt quickly to the water level fluctuations in Compartment A. Therefore, a constant gradient occurred during the waiting time of the plunger. A longer t_w like the dotted line in Figure 5.2 resulted in a semi-constant hydraulic gradient. The combined configuration of the model was modeled with an in between type of signal, like the dashed line in Figure 5.2. The plunger amplitude depended on the capacity of the servo and slide-crank mechanism.

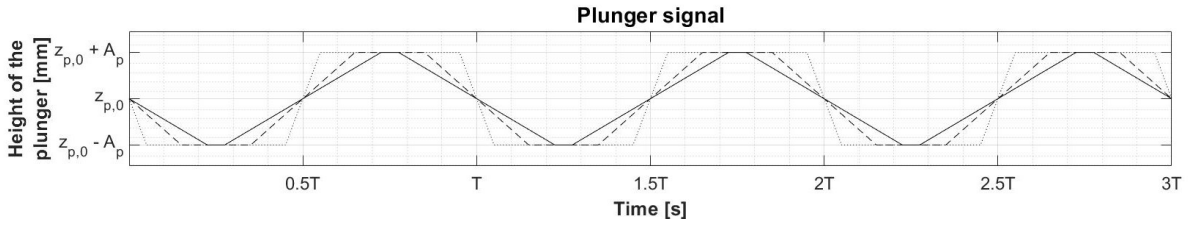

Figure 5.2: Plunger signal with the descriptive parameters.

5.3. Water level in Compartment A

By oscillating the plunger in compartment A, the water level of compartment A was influenced in an inversely proportional manner. The positive direction for the plunger movement was set to be upwards. The influence of this movement was quantified by the use of Archimedes' Principle. In other words, the water volume displaced by the plunger was divided over the difference in width of Compartment A and the plunger. The latter was converted into a 2-dimensional parameter. This resulted in the following equation for the water level of the compartment in which the plunger was fastened (z_A):

$$z_A(t+1) = z_A(t) - \frac{\frac{\partial}{\partial t} z_p \cdot L_p}{L_A - L_p} \tag{5.1}$$

The following assumptions were made by moving the plunger:

1. The plunger did not touch the bottom of the model;
2. The plunger did not fully emerge out of the water and/or submerge in the water;
3. The influence of the plunger was limited to the water level in the compartment in which the plunger is fastened.

5.4. Porous flow through the model

The movement of the plunger resulted in a head difference between Compartment A and the other two compartments. This caused the water to flow through the pores of the granular material of the filter structure. The positive direction of this flow was set from Compartment A to C. The porous flows were determined in a laminar manner by the use of Darcy's Law (Equation 2.7) and a mass balance was made every time step to determine the water levels of each compartment in the treated configuration. By modeling the flow laminar, the turbulent and inertial factor of the extended Forchheimer equation are neglected. This simplification is justified later on in Paragraph 5.6 by the Reynolds and Keulegan–Carpenter number, as discussed in Paragraph 2.1.3.

5.4.1. Parallel flow

In the parallel configuration, the water flowed between Compartment A and C of the model, as indicated by the blue arrow in Figure 3.3a. The permeability of the filter layer (k_f) influenced the specific discharge ($q_\parallel$). The head difference between the outer compartments was divided over the length of Compartment B in order to determine the hydraulic gradient. This resulted in the following equation:

$$q_\parallel(t+1) = -k_f \cdot h_f \cdot i_\parallel(t) \tag{5.2}$$

where:

$$i_\parallel(t) = \frac{z_C(t) - z_A(t)}{L_B} \tag{5.3}$$

Based on this specific discharge, the water level of Compartment C was given by:

$$z_C(t+1) = z_C(t) + \frac{q_\parallel \cdot \Delta t}{L_C} \tag{5.4}$$

The water level alterations in Compartment C influenced on their turn the water level in Compartment A. Therefore, an expanded version of Equation 5.1 for the parallel flow reads:

$$z_{A,\parallel}(t+1) = z_A(t) - \frac{\frac{\partial}{\partial t} z_P \cdot L_p + q_\parallel \cdot \Delta t}{L_A - L_p} \tag{5.5}$$

5.4.2. Perpendicular flow

Even though the perpendicular configuration was not tested in this study, the numerical description is given for comprehensive reasons. In the perpendicular configuration, the head difference inducing the porous flow was between the water level in Compartment A and the groundwater level in Compartment B, as indicated by the blue arrow in Figure B.1. Assumed was that the influence of the permeability of the filter layer on the porous flow is negligible since it is in the order of 1000 smaller compared to the permeability of the sand layer (k_s) (Verruijt, 1999). The length over which the head difference was divided, in accordance with Darcy's Law, was the ground water level in compartment B minus the height of the bottom model cells (h_s) and the filter layer thickness (h_f) (see Figure 5.1). In addition, the ground level fluctuation in Compartment B depended on the porosity of the sand layer (n_s). The equations used to describe the perpendicular set-up were the following:

$$q_\perp(t+1) = -k_s \cdot L_B \cdot i_\perp(t) \tag{5.6}$$

where:

$$i_\perp(t) = \frac{z_B(t) - z_A(t)}{z_B(t) - h_f - h_c} \tag{5.7}$$

The water level of Compartment B was given by:

$$z_B(t+1) = z_B(t) + \frac{q_\perp \cdot \Delta t}{L_B} \cdot \frac{1}{n_s} \tag{5.8}$$

Logically, the water level in Compartment A was also influenced. Therefore, an expanded version of Equation 5.1 for the perpendicular flow reads:

$$z_{A,\perp}(t+1) = z_A(t) - \frac{\frac{\partial}{\partial t} z_P \cdot L_p + q_\perp \cdot \Delta t}{L_A - L_p} \tag{5.9}$$

5.4.3. Combined flow

The combined situation consisted of the parallel and the perpendicular flow, as discussed in Paragraph 3.1.1. The flow is indicated by the blue arrow in Figure 3.3b. Just as the perpendicular model, the flow induced by the head differences between the outer compartments and the center of the model was considered as going through the sand layer only. The parallel specific discharge was:

$$q_{\parallel}(t+1) = -k_f \cdot h_f \cdot i_{\parallel}(t)$$

The perpendicular specific discharge consisted of two components. Namely, one for the flow between compartment A and B ($q_{A,\perp}$) and the other for the flow between compartment C and B ($q_{C,\perp}$):

$$q_{A,\perp}(t+1) = -k_s \cdot L_B \cdot i_{A,\perp}(t) \tag{5.10}$$

$$q_{C,\perp}(t+1) = -k_s \cdot L_B \cdot i_{C\perp}(t) \tag{5.11}$$

in which:

$$i_{A,\perp}(t) = \frac{z_B(t) - z_A(t)}{z_B(t) - h_f - h_c}$$

$$i_{C,\perp} = \frac{z_B(t) - z_C(t)}{z_B(t) - h_f - h_c}$$

The water levels of the compartments were given by:

$$z_{A,\parallel\&\perp}(t+1) = z_{A\parallel\&\perp}(t) - \frac{\frac{\partial}{\partial t} z_P \cdot L_p + q_{(\parallel} + q_{A,\perp}) \cdot \Delta t}{L_A - L_p} \tag{5.12}$$

$$z_{B,\parallel\&\perp}(t+1) = z_{B\parallel\&\perp}(t) + \frac{(q_{A,\perp} - q_{C,\perp}) \cdot \Delta t}{L_B} \cdot \frac{1}{n_s} \tag{5.13}$$

$$z_{C,\parallel\&\perp}(t+1) = z_{C\parallel\&\perp}(t) + \frac{(q_{\parallel} + q_{C,\perp}) \cdot \Delta t}{L_C} \tag{5.14}$$

In Figure 5.3, the flows in and out of each compartment are schematized for the combined set-up.

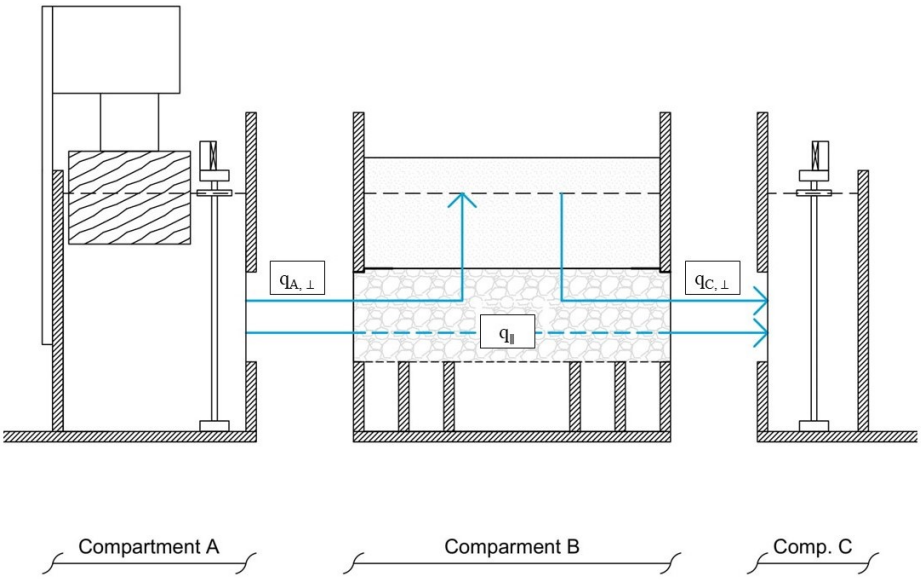

Figure 5.3: The positive porous flows per compartment by which through mass balances the water levels were determined.

In Figure 5.4, an example of the (ground)water levels for three plunger periods is given for every configuration. The parameters used for these plot were estimated and are given in the figure labels.

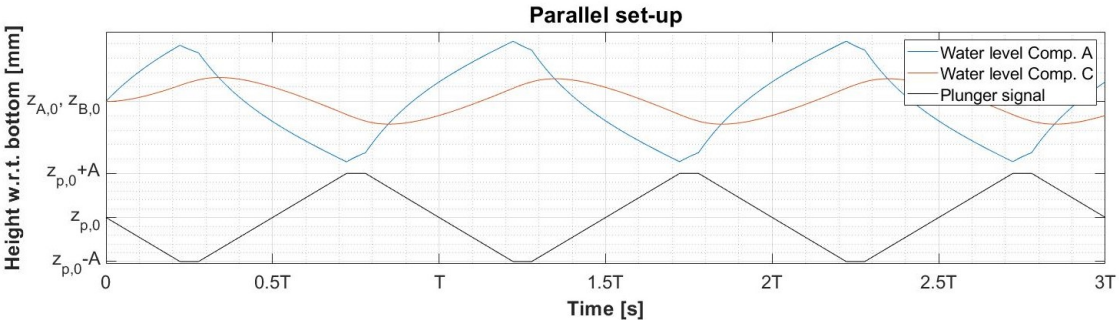

(a) An example of the water level elevations in the different compartments for the parallel configuration. To plot this graph, the following parameters were used: $T = 9$ [s], $t_w = 0.5$ [s], $A = 20$ [mm] $D_{50,f} = 6$ [mm], $n_f = 0.35$ [-] and $k_f = 0.135$ [m/s].

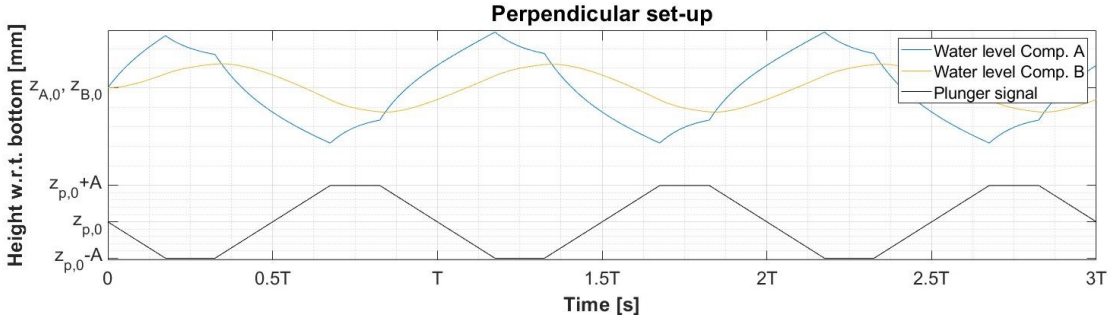

(b) An example of the water level elevations in the different compartments for the perpendicular configuration. To plot this graph, the following parameters were used: $T = 33$ [s], $t_w = 3$ [s], $A = 20$ [mm], $D_{50,s} = 0.5$ [mm], $n_s = 0.4$ [-] and $k_s = 3 \cdot 10^{-3}$ [m/s].

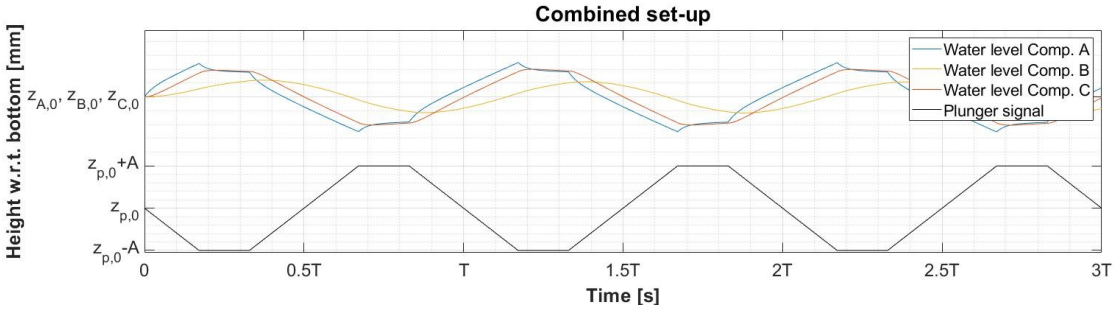

(c) An example of the water level elevations in the different compartments for the combined configuration. To plot this graph, the following parameters were used: $T = 19$ [s], $t_w = 3$ [s], $A = 20$ [mm], $D_{50,f} = 6$ [mm], $D_{50,s} = 0.5$ [mm], $n_f = 0.35$ [-], $n_s = 0.4$ [-], $k_f = 0.135$ [m/s] and $k_s = 3 \cdot 10^{-3}$ [m/s].

Figure 5.4: Examples of the water level elevations in the different compartments for the parallel, perpendicular and combined configuration.

5.5. Hydraulic gradients

Examples of the numerically determined hydraulic gradients, as discussed in Paragraph 5.4, are plotted as a solid line in Figure 5.5, 5.6 and 5.7 for the parallel, perpendicular and combined set-up respectively. Moreover, the hydraulic gradients determined by the use of the parameters of Ergun (1952), Engelund (1953), Koenders (1985) and den Adel (1987) in the Forchheimer Equation (2.3), as given in Table 2.1, are plotted. The parameters used to plot the graphs and the achieved *Re* and *KC*-values are given in the figure labels. Visible in all of the three plots is that the hydraulic gradients determined by the use of Ergun and den Adels parameters matches great with the gradients determined by the numerical model. However, this is very depending of the soil characteristics used.

In Figure 5.8, the *Re* is plotted against $\frac{Re}{KC}$ for the three configurations. Based on these dimensionless parameters, the parallel porous flow in Figure 5.5 and 5.7 are located in the transition region between laminar and turbulent with a bit of inertia resistance. For the perpendicular flow in Figure 5.6 and 5.7, the laminar resistance is dominant.

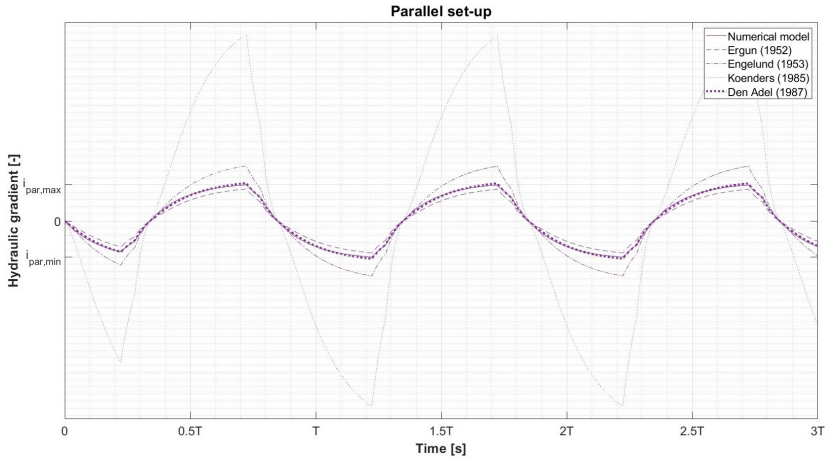

Figure 5.5: Parallel configuration using a saw-tooth plunger signal. To plot this graph, the following parameters are used: $T = 9$ [s], $t_w = 0.5$ [s], $A = 20$ [mm] $D_{50,f} = 6$ [mm], $D_{15,f} = 5.2$ [mm], $D_{EQ,f} = 5.1$ [mm], $n_f = 0.35$ [-] and $k_f = 0.135$ [m/s]. The maximum achieved dimensionless numbers for the numerical model are: $Re = 31.6$ [-] and $KC = 7.9$ [-].

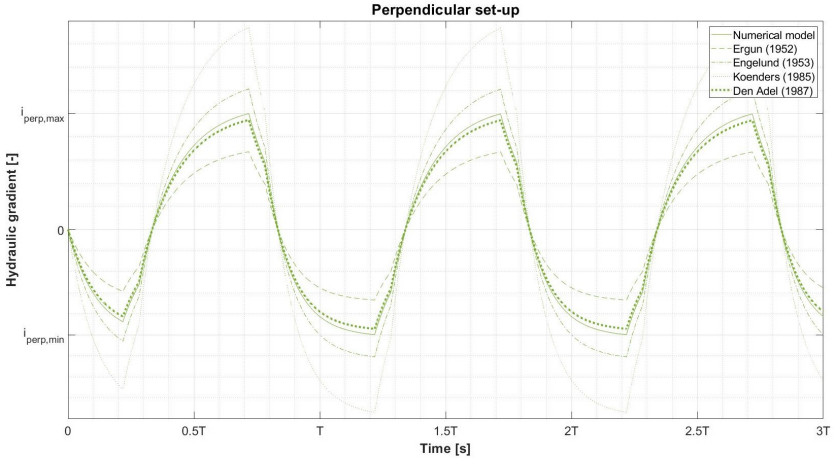

Figure 5.6: Perpendicular configuration using a semi block-type plunger signal. To plot this graph, the following parameters are used: $T = 33$ [s], $t_w = 3$ [s], $A = 20$ [mm], $D_{50,s} = 0.5$ [mm], $D_{15,s} = 0.43$ [mm], $D_{EQ,s} = 0.42$ [mm], $n_s = 0.4$ [-] and $k_s = 3 \cdot 10^{-3}$ [m/s]. The maximum achieved dimensionless numbers for the numerical model are: $Re = 0.3$ [-] and $KC = 41.3$ [-].

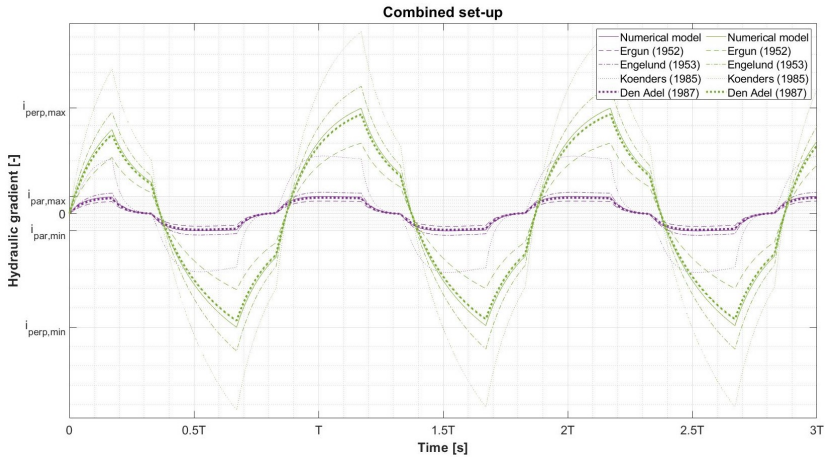

Figure 5.7: Combined configuration using a combined plunger signal. To plot this graph, the following parameters are used: $T = 19$ [s], $t_w = 3$ [s], $A = 20$ [mm], $D_{50,f} = 6$ [mm], $D_{15,f} = 5.2$ [mm], $D_{EQ,f} = 5.1$ [mm], $D_{50,s} = 0.5$ [mm], $D_{15,s} = 0.43$ [mm], $D_{EQ,s} = 0.42$ [mm], $n_f = 0.35$ [-], $n_s = 0.4$ [-], $k_f = 0.135$ [m/s] and $k_s = 3 \cdot 10^{-3}$ [m/s]. The maximum achieved dimensionless numbers for the numerical model are: $Re_{par} = 16.6$ [-], $Re_{perp} = 0.22$ [-], $KC_{par} = 8.8$ [-] and $KC_{perp} = 16.7$ [-].

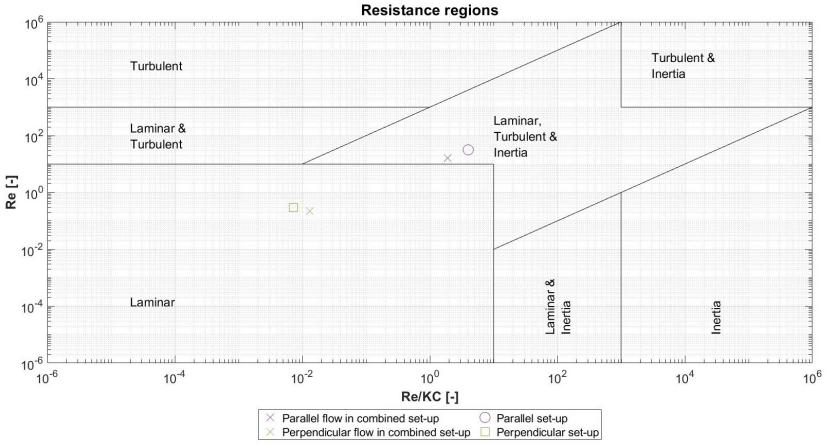

Figure 5.8: Regions with different dominant resistance components.

5.6. Validation and calibration of the numerical model

The numerical model was calibrated and validated by comparing the output to the physical model results. The parallel numerical model is compared to *Test 6*, the combined model is compared to *Test 11*. By comparing these models, one should bear in mind that the physical model had irregularities and may deviate to the numerical model to a certain extend, for instance in model dimensions. The perpendicular numerical model was not calibrated since no tests were conducted with this configuration in this study. The following parameters are used in the numerical model:

• Initial water level in Compartments A, B & C	$z_{A,0} = z_{B,0} = z_{C,0}$:	383.5	[mm]
• Initial level of the plunger	$z_{p,0}$:	317.5	[mm]
• Height of the filter layer	h_f:	200	[mm]
• Height of the bottom cells	h_c:	180	[mm]
• Length of Compartment A	L_A:	320	[mm]
• Length of Compartment B	L_B:	520	[mm]
• Length of Compartment C	L_C:	160	[mm]
• Length of the plunger converted to 2D	L_p:	205	[mm]
• Permeability filter layer	k_f:	*To be calibrated*	[m/s]
• Permeability base layer	k_s:	*To be calibrated*	[m/s]
• porosity filter layer	n_f:	*To be calibrated*	[-]
• Porosity base layer	n_s:	*To be calibrated*	[-]

5.6.1. Parallel calibration

The results of *Test 6* (SR = 13.1 [-] and $D_{50,f}$ = 4.02 [mm]) was used to validate and calibrate the numerical model of the parallel set-up. The parameter determined by the parallel calibration was the permeability of the filter layer ($k_{f,cal}$). The output of the numerical and physical model is given in Figure 5.9.

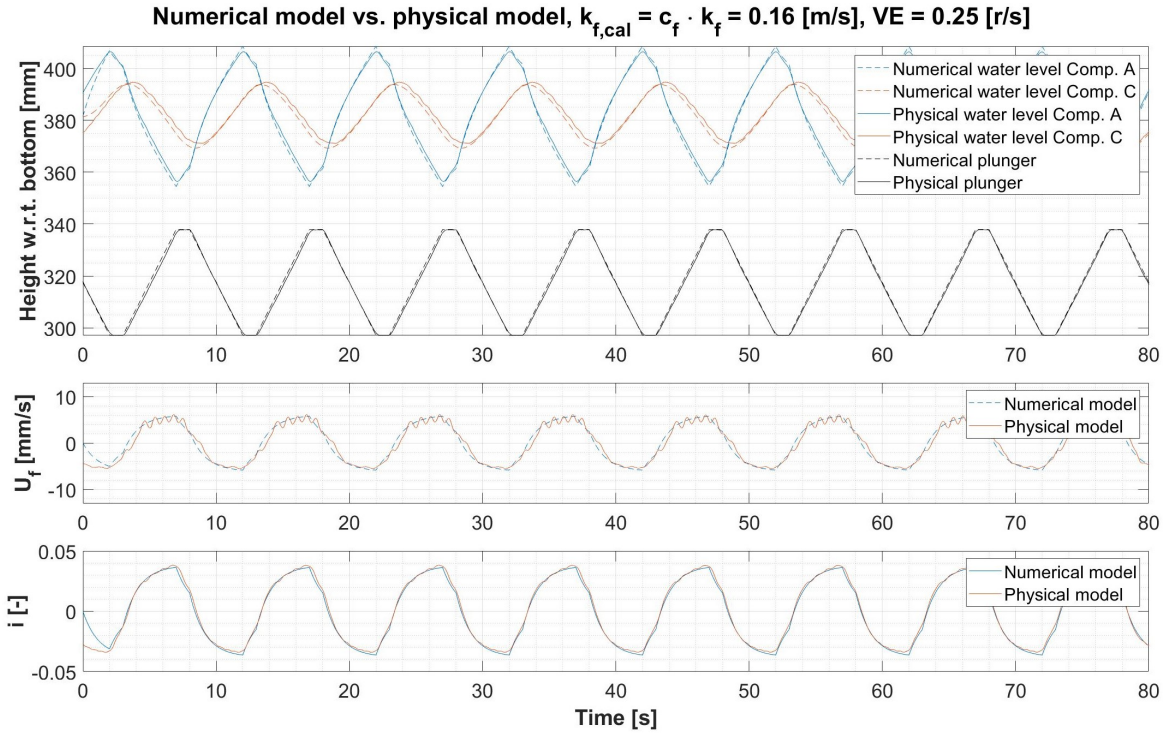

Figure 5.9: Comparison of the numerical model and the physical model results of *Test 6* for about 8 plunger periods. In the top graph, the plunger movement and water levels are plotted. In the middle plot, the filter velocities are compared. In the bottommost graph, the parallel hydraulic gradients are shown.

Filter layer permeability

In this figure, the servo velocity was set to 0.25 [r/s], a parameter discussed in Paragraph 3.2. In the top graph, the vertical oscillation of the plunger is given with the corresponding water levels in the two outer compartments. As could be seen from this figure, the numerical determined water levels correspond to the physical measured water levels in the test when $k_{f,cal} = 0.16$ [m/s] is used. As discussed in Paragraph 2.1.2, $k_{\text{gravel}} = 0.001 - 0.1$. Besides, the filter layer permeability could be estimated by the use of Equation 2.10, as discussed in Paragraph 2.1.2. The variables in this equation are n_f, α and β-value. In Table 5.1, 5.2 and 5.3, the range of k_f is determined for $n_f = 0.40$, 0.50 and 0.60 respectively. The dominance of the α-value of the k_f indicates that the laminar resistance is dominant, like assumed in Paragraph 5.4 . The $k_{f,cal}$ is achieved by Equation 2.10 if $0.50 < n_f < 0.60$. In Appendix C, the porosity of gravel 3 – not the one used in this test but nevertheless used as an estimation – was determined to be 0.45. This means that the porosity is rather high, as expected since the gravel was not compacted during the set-up of the test. Furthermore, this means that the $k_{f,cal}$ is higher compared to the real k_f of the gravel layer. To cope with this, a model factor for the parallel set-up c_f was introduced, defined as:

$$c_f = \frac{k_{f,cal}}{k_f} \tag{5.15}$$

If $n_f = 0.45$ is taken with an average α and β-value of 1500 and 1.25 respectively, $k_f = 0.0316$ [m/s]. This gives:

$$c_f = \frac{0.16}{0.03} = 5.3$$

The difference between $k_{f,cal}$ and k_f was probably due to water bypassing the filter layer when flowing between the two outer compartments, increasing the average permeability of the layer. A place where this could have happened, is along the front and back of the model, however, bubble plastic was placed to avoid larger pores in this area. Another location is underneath the filter layer, as indicated by the blue arrow in Figure 5.10. At this location, two mesh grids were placed to block the infall of gravel into the bottom cells. Because of small bends of these mesh grid, as visible in Figure 3.16, water could have flowed through this area. Embedding the filter layer slightly into the bottom cells, or heightening of the two outer bottom cell walls , will decrease this effect for future tests.

Figure 5.10: Location where water could bypass the granular filter layer.

$n_f = 0.4$	$\beta_{ERG} = 1.0$	$\beta_{ERG} = 1.5$
$\alpha_{ERG} = 1000$	$k_f = 0.0280$ [m/s]	$k_f = 0.0279$ [m/s]
$\alpha_{ERG} = 2000$	$k_f = 0.0141$ [m/s]	$k_f = 0.0141$ [m/s]

Table 5.1: Estimation of k_f [m/s] with $n_f = 0.4$

$n_f = 0.5$	$\beta_{ERG} = 1.0$	$\beta_{ERG} = 1.5$
$\alpha_{ERG} = 1000$	$k_f = 0.0776$ [m/s]	$k_f = 0.0769$ [m/s]
$\alpha_{ERG} = 2000$	$k_f = 0.03941$ [m/s]	$k_f = 0.0393$ [m/s]

Table 5.2: Estimation of k_f [m/s] with $n_f = 0.5$

$n_f = 0.60$	$\beta_{ERG} = 1.0$	$\beta_{ERG} = 1.5$
$\alpha_{ERG} = 1000$	$k_f = 0.2002$ [m/s]	$k_f = 0.1945$ [m/s]
$\alpha_{ERG} = 2000$	$k_f = 0.1051$ [m/s]	$k_f = 0.1042$ [m/s]

Table 5.3: Estimation of k_f [m/s] with $n_f = 0.60$

Other remarks

In the upper plot, the movement of the numerical plunger is, in contrast to the physical plunger, more angular since no acceleration and deceleration was used to describe the plunger signal. This resulted in slightly greater amplitudes of the water levels, in particular for the compartment in which the plunger is fastened. In the second plot, the filter velocities (u_f) are compared. Visible in this graph is that the positive filter velocity had an osculating movement. This was due to the styrofoam of the floater in Compartment C rubbing against the model during water level decrease.

Comparison of the calibration to the full test

The calibration in this paragraph was based on a single servo velocity ($VE = 0.25$ [r/s]). To check if the determined $k_{f,cal}$ is also valid for faster and slower velocities during the test, every maximum parallel hydraulic gradient of *Test 6* is plotted together with the numerical determined maxima in Figure 5.11. As can be seen from this figure, is that the numerical and physical maximum hydraulic gradient match very well. The numerical model slightly over estimates the gradients for the lower plunger periods and under estimates the gradients for the higher plunger periods.

In Figure 5.12, the Re-number versus $\frac{Re}{KC}$ is plotted on a logarithmic scale for every test segment executed in during the physical test. For the smallest servo velocity ($VE = 0.10$ [r/s]), the laminar resistance is dominant. By increasing the servo velocity, and therefore increasing the hydraulic gradient, the markers move upward into the combined region, but still nearby the laminar region border. This means that the simplification to model the parallel porous flow strictly laminar does not fully agree with reality, but nevertheless estimates the gradients satisfactory since the influence of the turbulent and inertial part is limited.

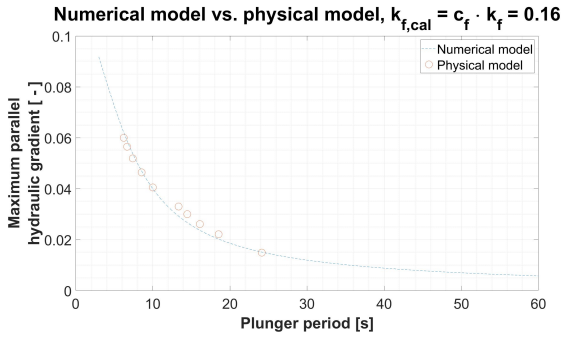

Figure 5.11: The maximum parallel hydraulic gradients measured in the physical model test are plotted with the numerical determined ones. The gradients are plotted against the plunger period, the parameter altered during the test to increase the gradient.

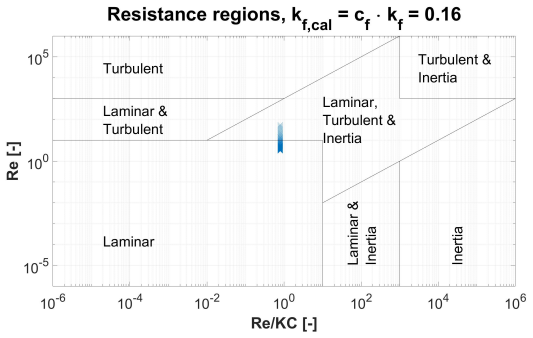

Figure 5.12: The influence of the laminar, turbulent and inertial resistance on the hydraulic gradient. The markers are moving upward when decreasing the plunger period wherefore increasing hydraulic gradient.

5.6.2. Combined configuration

Test 11 (SR = 13.1 [-], $D_{50,f}$ = 8.75 [mm] and $D_{50,s}$ = 0.48 [mm]) was used to calibrate and validate the combined set-up. The parameter of interest in order to calibrate the model were k_f, n_f, k_s and n_s. The numerical model was calibrated to achieve the same hydraulic gradients as the physical model, given in Figure 5.13.

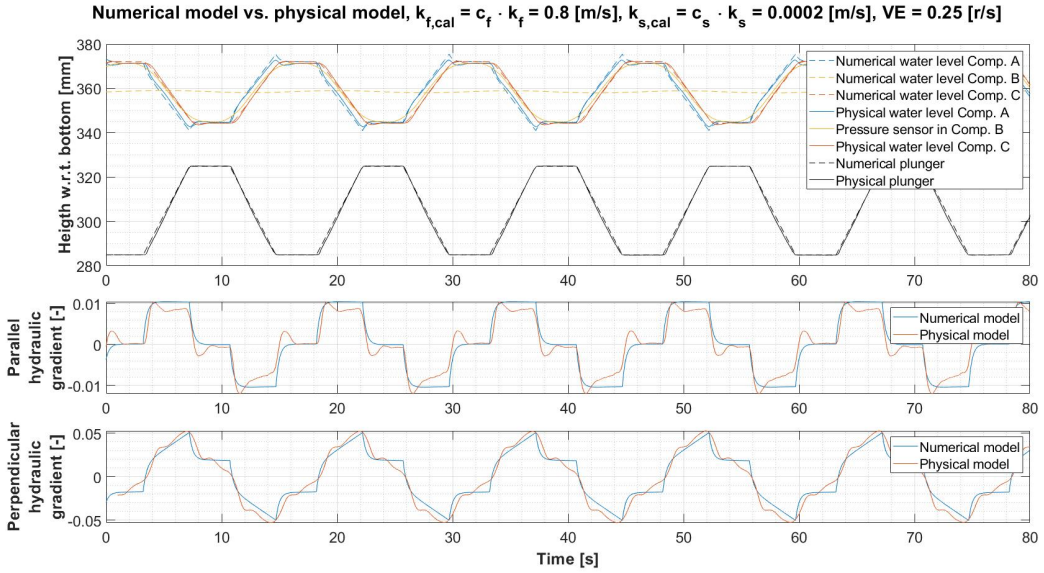

Figure 5.13: A comparison of the numerical and the physical model results of *Test 11* for about 5 plunger periods. In the top graph, the plunger movement and water levels are plotted. In the middle plot, the parallel hydraulic gradients are shown. In the bottom graph, the perpendicular hydraulic gradient are given.

Filter and base layer permeability

Like the parallel set-up, the servo velocity was set to 0.25 [r/s]. The numerical model was calibrated to the physical model using $k_{f,cal}$ = 0.80 [m/s] and $k_{s,cal} = 2.6 \cdot 10^{-4}$ [m/s]. The $k_{s,cal}$ is in the expected range for permeability, namely $10^{-6} - 10^{-3}$ [m/s]. The k-values according to Equation 2.10, using α = 1500, β = 1.25, n_f = 0.45 (as determined in Appendix C for the gravel used in this this) and n_s = 0.40 are:

$$k_f = 0.15 \text{ [m/s]}$$
$$k_s = 2.6 \cdot 10^{-4} \text{ [m/s]}$$

This gives:

$$c_f = 5.4 \text{ [-]}$$
$$c_s = 0.8 \text{ [-]}$$

The c_f matches the calibration of the parallel set-up. The c_s value indicates that the calibrated perpendicular hydraulic gradient corresponds to the measured one in the physical model.

Other remarks

In the upper graph of Figure 5.13, a clear difference is visible between the two yellow lines. The dashed line is the numerical groundwater level in Compartment B which was determined by in- and outflow of water of Compartment B, as discussed in Paragraph 5.4.3 and shown in Figure 5.3. The solid line is the output of a pressure sensor in the physical model. The signal output of the pressure sensors were calibrated to the water levels in Compartment A and B, as discussed in Paragraph 3.2.3. Moreover, the perpendicular hydraulic gradient was determined differently for the numerical and physical model. The numerical perpendicular hydraulic gradient was determined by the head difference between the outer compartments and the groundwater level in Compartment B. It was not possible to measure the groundwater level during physical modeling. Therefore, the physical perpendicular hydraulic gradient was determined by two vertical placed pressure sensors, as discussed in Paragraph 3.3 and shown in Figure 3.12.

Comparison of the calibration to the full test

The calibrated numerical model is compared to all the results of Test 11. In Figure 5.14a, the maximum parallel hydraulic gradients of the physical model are plotted with the numerical model using $k_{f,cal}$ = 0.8 [m/s], showing great similarities. In Figure 5.14b, the same is done for the perpendicular hydraulic gradient. For the shorter plunger periods, the calibrated numerical and physical model match very well. For the longer plunger periods, the numerical model overestimates the hydraulic gradient. This could be due to that the test was performed by decreasing the plunger period every 3 hours. In other words, Test 11 started with the red circle on the right hand side of the plot, moving a marker to the left every 3 hours. The base material was not compacted after installation. Therefore, the permeability of the base material could been decreased during the test by rearrangement of the grains, which on their turn could have happened because of erosion of the sand into the filter layer.

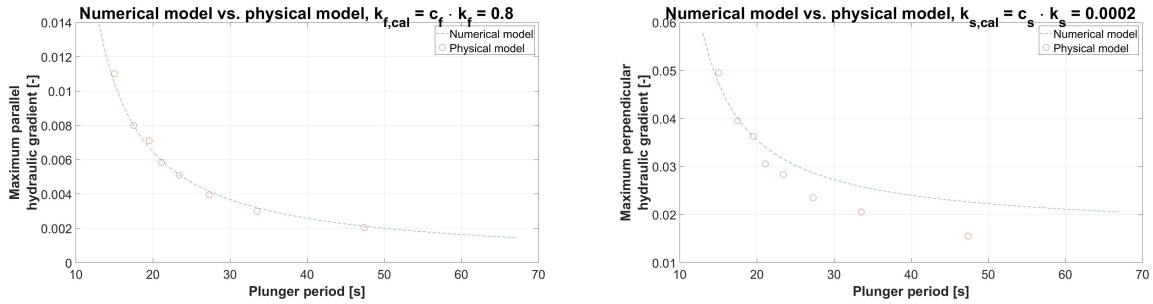

(a) Plunger period versus parallel hydraulic gradient.

(b) Plunger period versus perpendicular hydraulic gradient.

Figure 5.14: The maximum hydraulic gradients measured in the physical model test plotted with the numerical determined ones. The gradients are plotted against the plunger period, the parameter altered during the test to increase the hydraulic gradient.

5.7. Conclusion

Various parameters and phenomena influenced the hydraulic gradient induced in the model, as given in Appendix B.2. Practical examples are (1) the sorting and placement of the stones in the filter layer and sand in the base layer influencing the permeability of the layers, (2) the placement of the bottom cells and division screens influencing the volumes per compartment and therefore the water level fluctuations, (3) bend out of the wire mesh could enlarge the filter layer, reducing the volumes of the outer compartments, as illustrated in Figure 5.15. All these factors will result in a different forced gradient per test. Comparing the numerical model with the physical model for the configurations leads to the conclusion that the results are not fully identical but nevertheless satisfactorily. The simplification to program the porous flow fully laminar did not influence the results negatively. For the parallel configuration, a model factor (c_f) of 5.3 and 5.4 was determined during calibration for the parallel and combined set-up. This model factor is probably the results of water bypassing the pores of the gravel, increasing the average permeability of the filter layer. For the perpendicular flow in the combined set-up, the numerical and physical model agreed. Therefore, it is concluded that the numerical model could be used to design the new physical model in Chapter 6 and plot accessory design graphs in Paragraph 6.5.

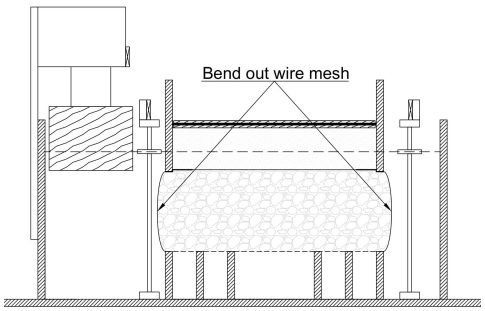

Figure 5.15: Bend out of the wire mesh of the division screen.

6

New physical model design for superimposed load and inclined filter tests

A new physical model was designed and constructed. Using this model, inversed granular filter tests with a superimposed load to mimic the sand columns on top of a filter layer and inclined filters shapes could be performed. The principle of the model is comparable to the model described in Chapter 3 and 5, but scaled up and strengthened to cope with the superimposed load. The final design of the physical model was the result of multiple iterations and designed in cooperation with DEMO, the electronic and mechanical support division of the TU Delft. Unfortunately, due to the time consuming process of designing and constructing the model, and the imposed restrictions by the government due to the worldwide COVID-19 pandemic, it was not feasible to conduct any tests in the new model.

In this chapter, the design of the new physical model is captured. First of all, the goal of the new model is discussed with the corresponding model requirements. Subsequently, the main model dimensions are set and the loads exerting on the model are treated. Thirdly, the design and various features of the model are given. Lastly, design graphs of the new physical model are plotted.

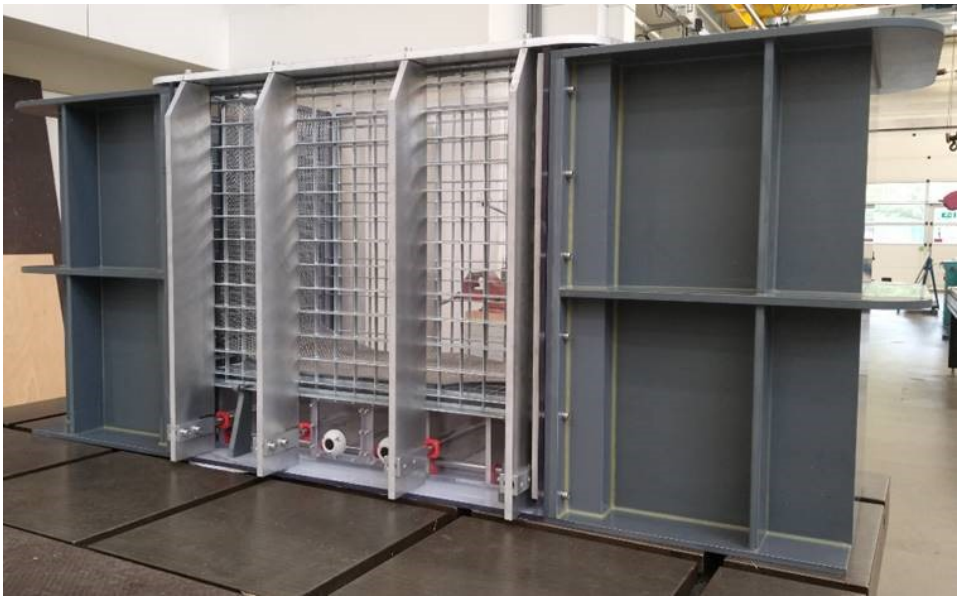

Figure 6.1: The new physical model for superimposed load and inclined filter tests.

6.1. Model goal and requirements

The goal of designing and constructing a new physical model was to facilitate a model to the research line that can cope with an external load corresponding to 10 meters of sand column and to provide room for inclined filter tests. The requirement to design the model were:

1. The front and back of the model must be transparent to detect erosion;
2. The model must be fully watertight;
3. The model and model components need to be able to withstand a superimposed load mimicking the vertical earth pressure, with a maximum of 10 [m] sand column;
4. The flow through the compartments need to go in one line, in other words, inner walls need to be aligned;
5. The grid at the bottom used to divide the filter layer and the bottom cells needs to be removable;
6. It must be possible to seal off the top of Compartment B for the parallel configuration. The model compartments A, B and C are discussed in Paragraph 3.1;
7. It must be possible to close of Compartment B from C, or Compartment C should be able to disconnect for the perpendicular set-up;
8. The model needs to be transportable;
9. The cables of the load cells that could be used at the bottom of the model, preferably exit the model trough the back of the model to reduce wall effects along the cable. This exit needs to be watertight (e.g. a swivel);
10. Inclined model tests should be possible in the same model;
11. The model needs to be larger than the concept model discussed in Chapter 3. In this way, any scale effects could still be noted since the model is designed for a scale of 1:1. Moreover, this makes the model more suitable for future tests, of which the whereabouts are unknown at this moment. However, manageability of the model should be kept in mind.

6.2. Main model dimensions

The first step of the model design was the determination of the outer dimensions of the three compartments A, B and C. The following dimensions were determined:

- **Height of the working section of Compartment B = 600 [mm]**
  This height was based on the average length of an arm. If the model was designed higher, the model will be less manageable during the set-up phase and cleaning the model.
- **Total height of the model = 760 [mm]**
  A height of 160 [mm] was designed at the bottom of Compartment B to ensure room for any load cells and visual erosion detection. Therefore, the total height of the model is 760 [mm].
- **The length of Compartment A = 400 [mm]**
  This length was chosen after altering various values in numeric model, described in the Chapter 5. Moreover, this length leads to more room around the plunger which in their turn will results in less waves induced by the plunger movement.
- **Height-length ratio of Compartment B is set to 1:1.5**
  This ratio ensured room for inclined filter structure tests.
- **Length of Compartment B = 750 [mm]**
  Keeping the subsidence of the stamp in Compartment B into account (100 [mm]), the height of the filter structure is 500 [mm]. Therefore, the width of Compartment B was set to 750 [mm] by the use of the height-length ratio of Compartment B.

- **The length of Compartment C = 400 [mm]**
  Compartment C was set equal to Compartment A because of manufacture-ability benefits. The volume of the compartment could be reduced by the use of Styrofoam.

- **The width of the model = 350 [mm]**
  The width was set as a compromise between the superimposed load, which increases with the width, and a significant width to reduce model effects.

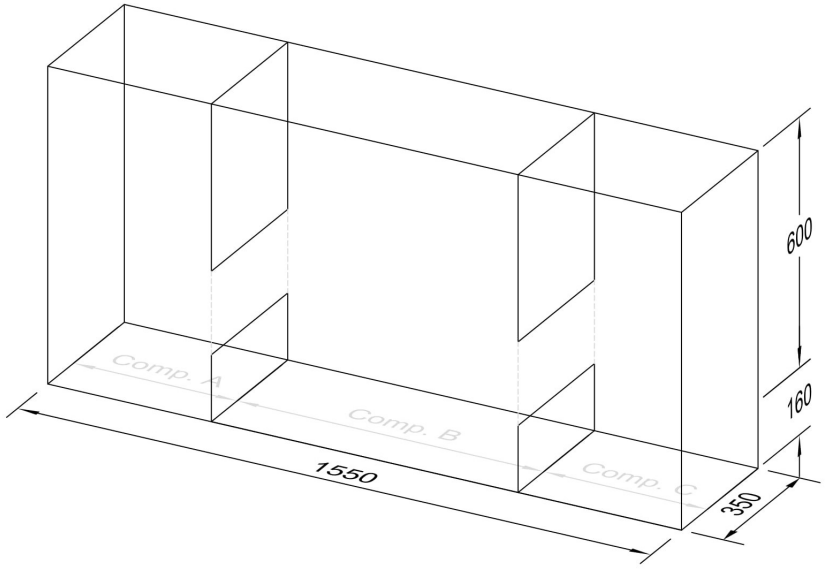

Figure 6.2: The outline of the new physical model. The lengths of the compartments are 400, 750 and 400 [mm] in alphabetical order. All dimensions are given in millimeters.

6.3. Loads

In this section, the loads on the physical model in Compartment B are discussed. First of all, the vertical loads, consisting of the superimposed load, effective soil pressure, and pore water pressure. Secondly, the horizontal load is treated. The latter is the lateral earth pressure induced by the vertical loads. The strength of the physical model needs to be sufficient enough in order to hold these loads and minimize deflections of the model since this could result in leakage and damage.

6.3.1. Superimposed load

The superimposed load (q_{sl}) is the load transmitted by the stamp that mimics the sand column on top of the filter structure. Assumed was that:

- Sand column height = 10 [m];
- Specific density of saturated sand = 20 [kPa].

This resulted in the following vertical load on the model induced by the stamp:

$$q_{sl} = 20 \cdot 10 = 200 \text{ [kPa]}$$

6.3.2. Effective soil pressure

Compartment B consists of the following layers, from top to bottom:

- 100 [mm] room for the stamp;
- 100 [mm] of dry sand a 16 [kN/m^3];
- 200 [mm] of saturated sand a 20 [kN/m^3];
- 200 [mm] of saturated gravel a 20 [kN/m^3];
- 160 [mm] room for load cell(s).

The specific density of water was set to 10 [kN/m^3]. The layers of interest for determining the effective soil pressure (σ'_{zz}) are highlighted yellow in Figure 6.3. This resulted in the following effective soil pressure:

$$\sigma'_{zz} = 0.1 \cdot 16 + (0.2 + 0.2) \cdot (20 - 10) = 5.6 \text{ [kPa]}$$

6.3.3. Pore water pressure

Pore water pressure (p) occurs in the saturated sand and gravel layer, as illustrated in blue in Figure 6.4. The layer for load cells was neglected since no effective soil pressure is present in this area. This gave a total pore water pressure of:

$$p = (0.2 + 0.2) \cdot 10 = 4 \text{ [kPa]}$$

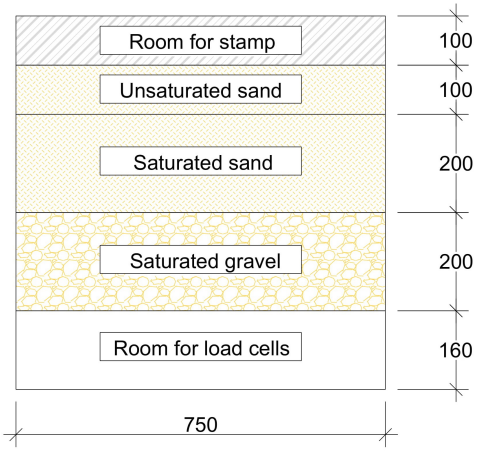

Figure 6.3: Model layers of interest for the effective soil pressure, highlighted in yellow.

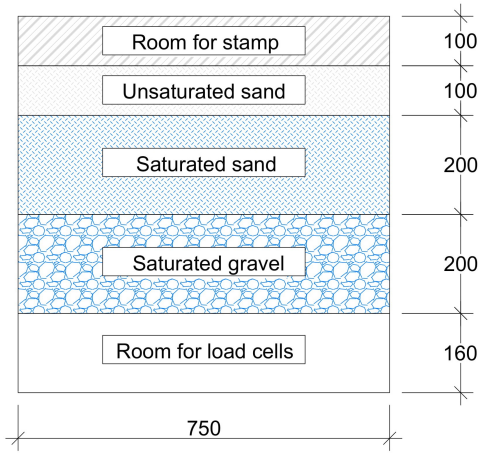

Figure 6.4: Model layers of interest for the pore water pressure, highlighted in blue.

6.3.4. Total vertical pressure

The total vertical pressure (σ_{zz}), including a safety factor of 1.2:

$$\sigma_{zz} = (q_{sl} + \sigma'_{zz} + p) \cdot 1.2 \approx 250 \text{ [kPa]}$$

6.3.5. Lateral earth pressure

The pressure that is exerted by the superimposed load and the soil pressure in the horizontal direction (σ_{xx}) is by definition a factor of the effective vertical pressure plus the pore water pressure. This reduction factor, the coefficient of earth pressure at rest (K_0) is between 0.6 and 0.7 (Verruijt, 1999). Again, a safety factor of 1.2 is used to hedge the uncertainties of K_0.

$$\sigma_{xx} = p + (\sigma'_{zz}) \cdot K_0 \cdot 1.2 \approx 176 \text{ [kPa]}$$

6.4. Final model design

The final model was designed and manufactured in cooperation with DEMO. In this section, model components of interest are listed. These components are indicated in a bird view (Figure 6.5), a front view (Figure 6.6), and a longitudinal cross-section (Figure 6.7).

- **Polyvinyl-chloride**
  Compartment A and C were made of polyvinyl-chloride (PVC). The PVC compartments are shown in Figure 6.8.

- **Poly-carbonate**
  Poly-carbonate was used to enclose Compartment B. This material was chosen as front and back of the model because of the transparent and strong material characteristics. In order to make the model water tight, the same material was used for the sides of Compartment B and glued to the front and back. Water cutting was used to create two openings at one side of Compartment B and one opening at the other side. The side openings are able to be closed in order to set-up an inclined or horizontal test set-up. At the bottom, two openings were made to access the bottom and load cells. The poly-carbonate box is shown in Figure 6.9.

- **Mesh grid**
  Mesh grids were used around the poly-carbonate of Compartment B to cope with the lateral earth pressure. Moreover, the grid allows a view through the front and back of the model and allows water to flow through the sides of the compartment.

- **Column strips**
  Column strips were used around the mesh grid to cope with the lateral earth pressure and reduce deflection while blocking the view as little as possible. At the sides of Compartment B, a beam strip was used for the same reasons.

- **Flange**
  A rectangular flange was manufactured and constructed at the top of Compartment B. The flange copes with the lateral earth pressure transferred by the column strips while leaving room for the stamp to be placed and removed.

- **Tensile bars**
  Tensile bars were constructed through the bottom cells in longitudinal and transversal direction to cope with the lateral earth pressure transferred by the column strips.

- **Stamp**
  The stamp was used to transmit the superimposed load from the hydraulic press to Compartment B. The bottom of the stamp was perforated to avoid water pressure to build up. It is advised to use a geotextile underneath the stamp to block sand passing upwards through the stamp.

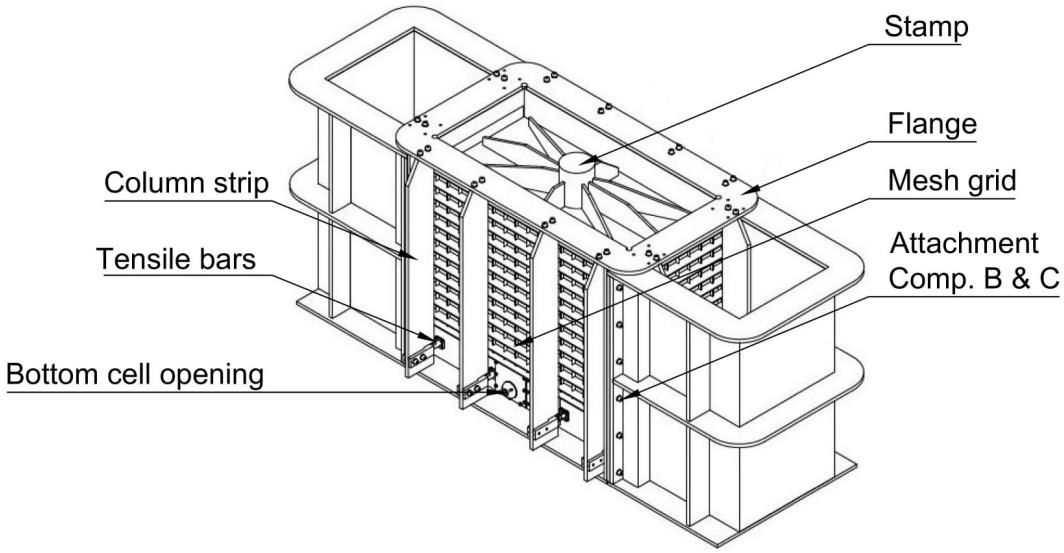

(a) Model design.

(b) Photo of the model.

Figure 6.5: Bird view.

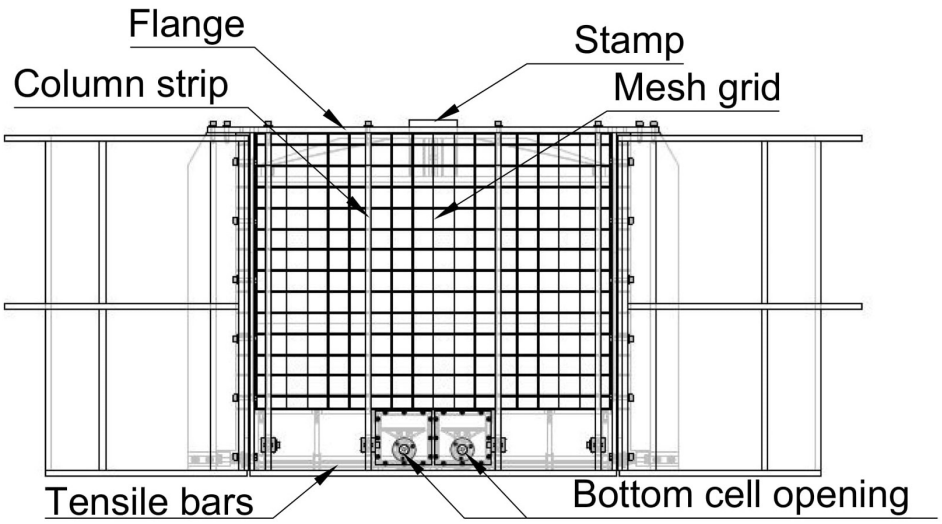

(a) Model design.

(b) Photo of the model.

Figure 6.6: Front view.

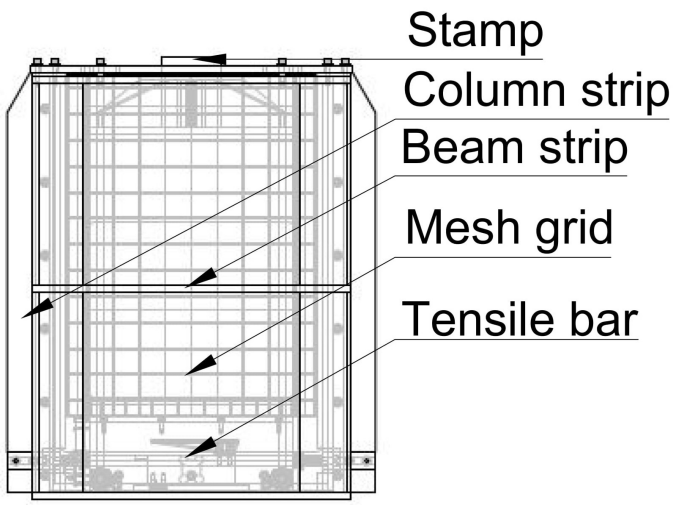

(a) Model design.

(b) Photo of the model.

Figure 6.7: Side view.

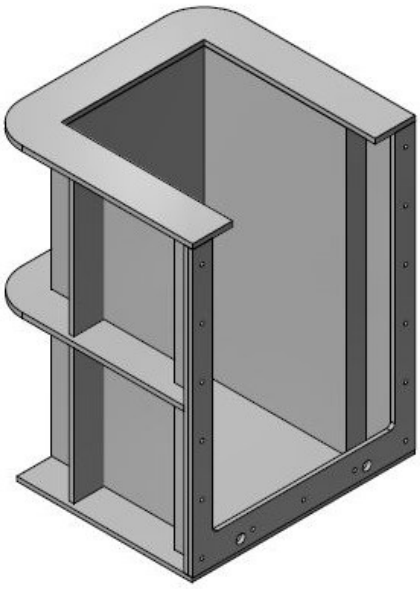

Figure 6.8: Compartments A and B, made of PVC.

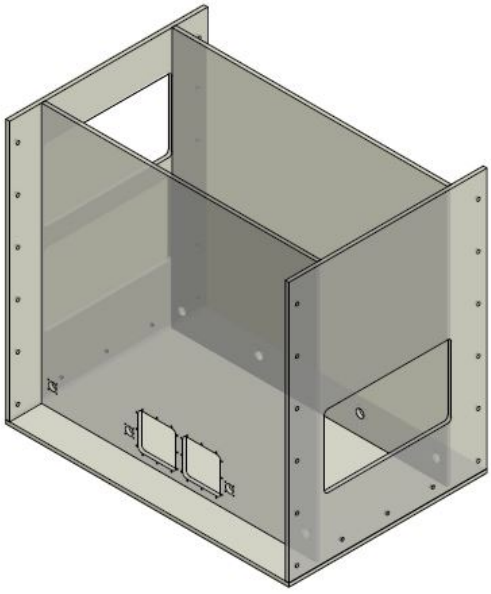

Figure 6.9: The inner part of Compartment B, made of Polycarbonate.

6.5. Design graphs

In this section, the design graphs of the new physical model are plotted for the parallel, perpendicular and combined set-up. Based on these graphs, one could indicate the correlation expected between the plunger period and the forced hydraulic gradient for various soil types. The plunger size was increased over the graphs and indicated as a percentage of Compartment A. The following waiting times were used for the plunger signal:

- Parallel configuration: 1 [s]
- Perpendicular configuration: 3 [s]
- Combined configuration: 3 [s]

Furthermore, the following variables are used to create the design graphs:

- Filter height = 200 [mm]
- Length Compartment C = 400 [mm]

6.5.1. Parallel configuration

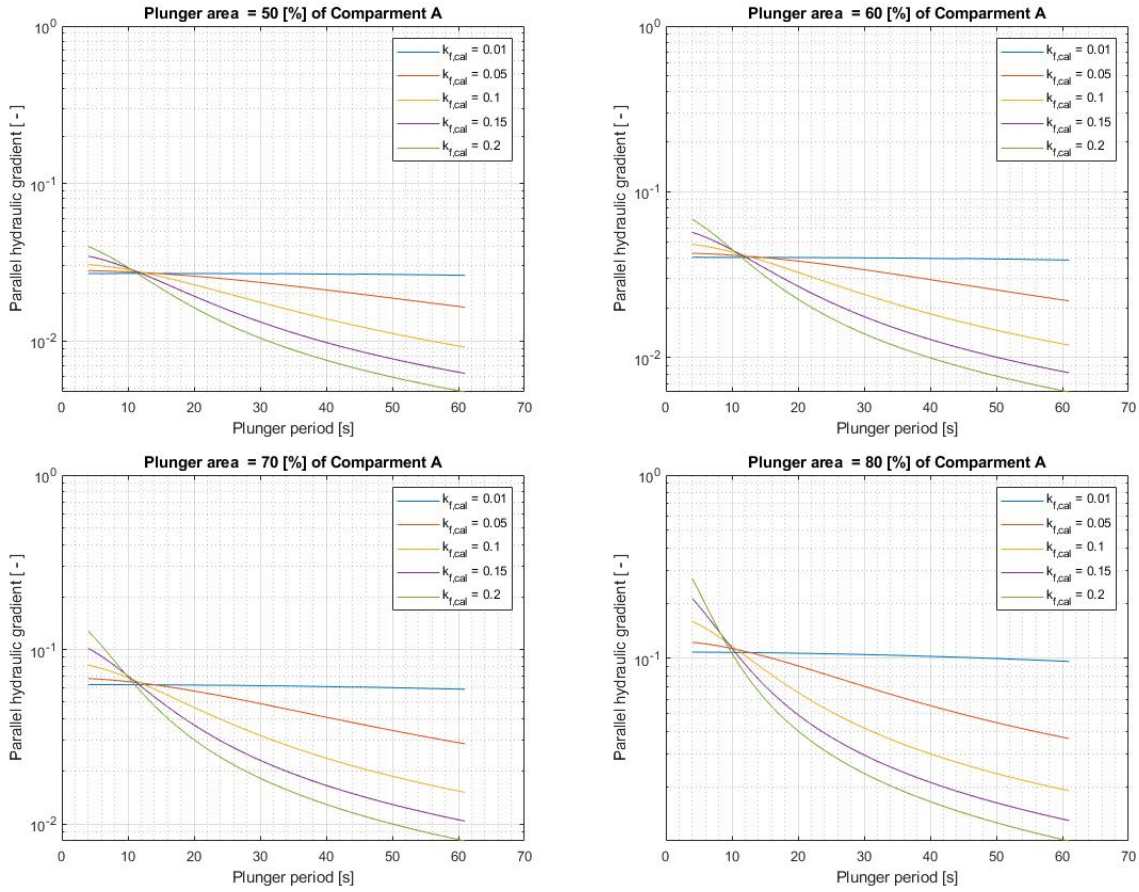

Figure 6.10: Design graphs of the parallel configuration.

6.5.2. Perpendicular configuration

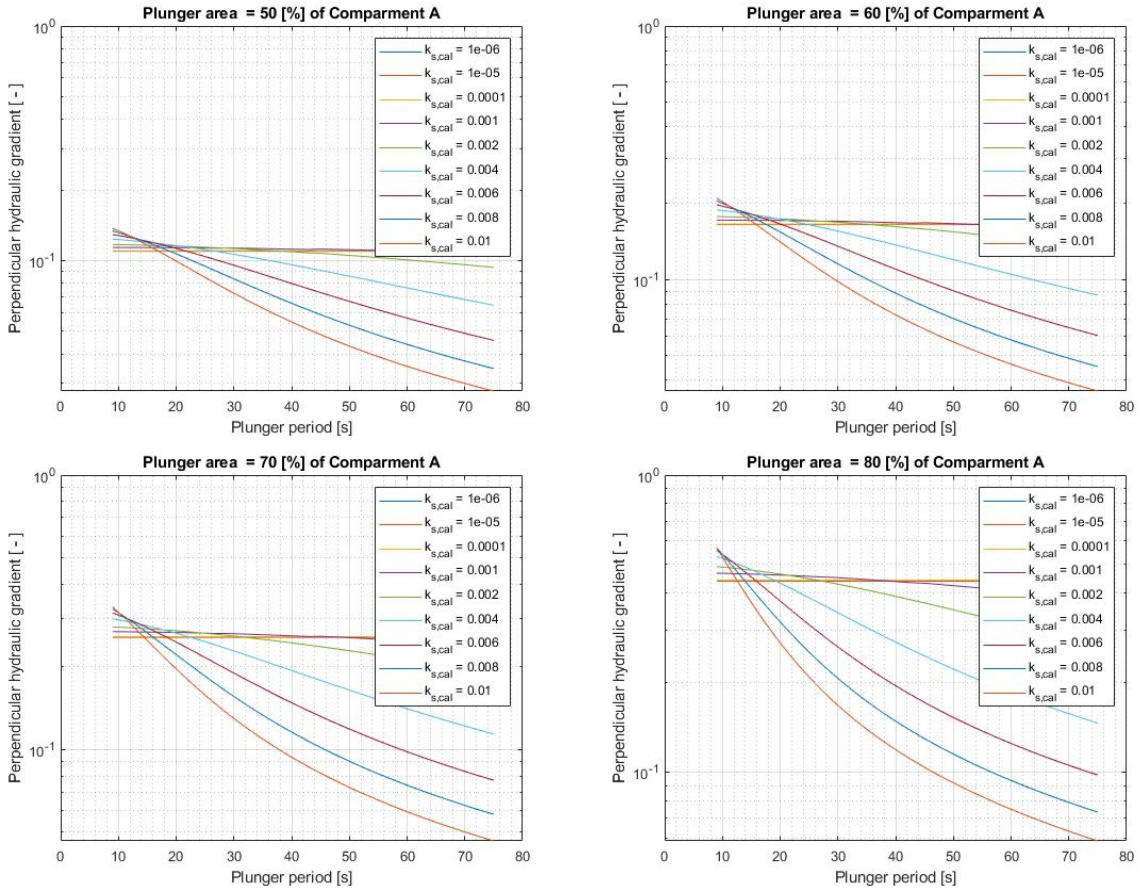

Figure 6.11: Design graphs of the perpendicular configuration.

6.5.3. Combined configuration

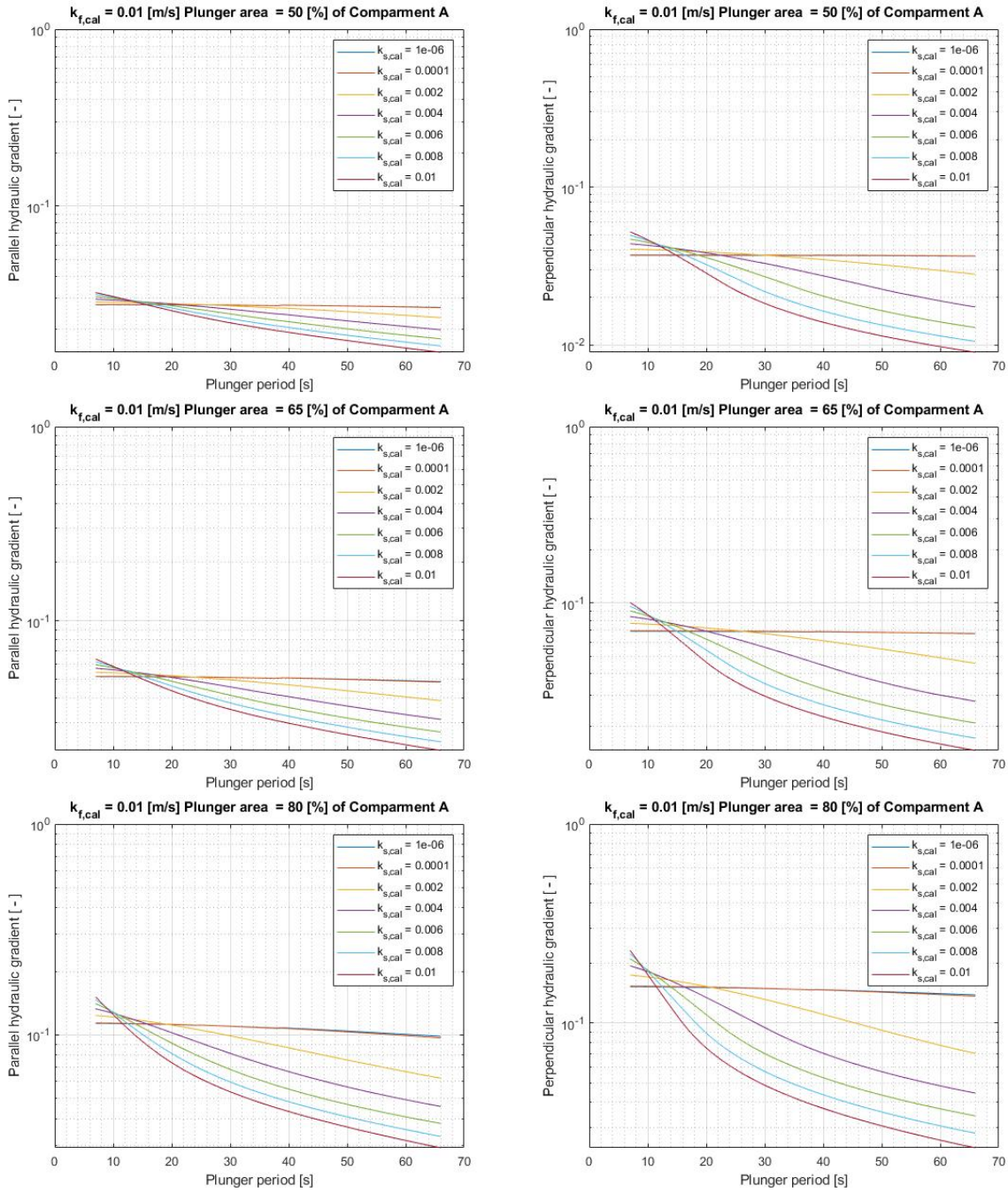

Figure 6.12: Design graphs of the combined configuration with a filter permeability of 0.01 [m/s].

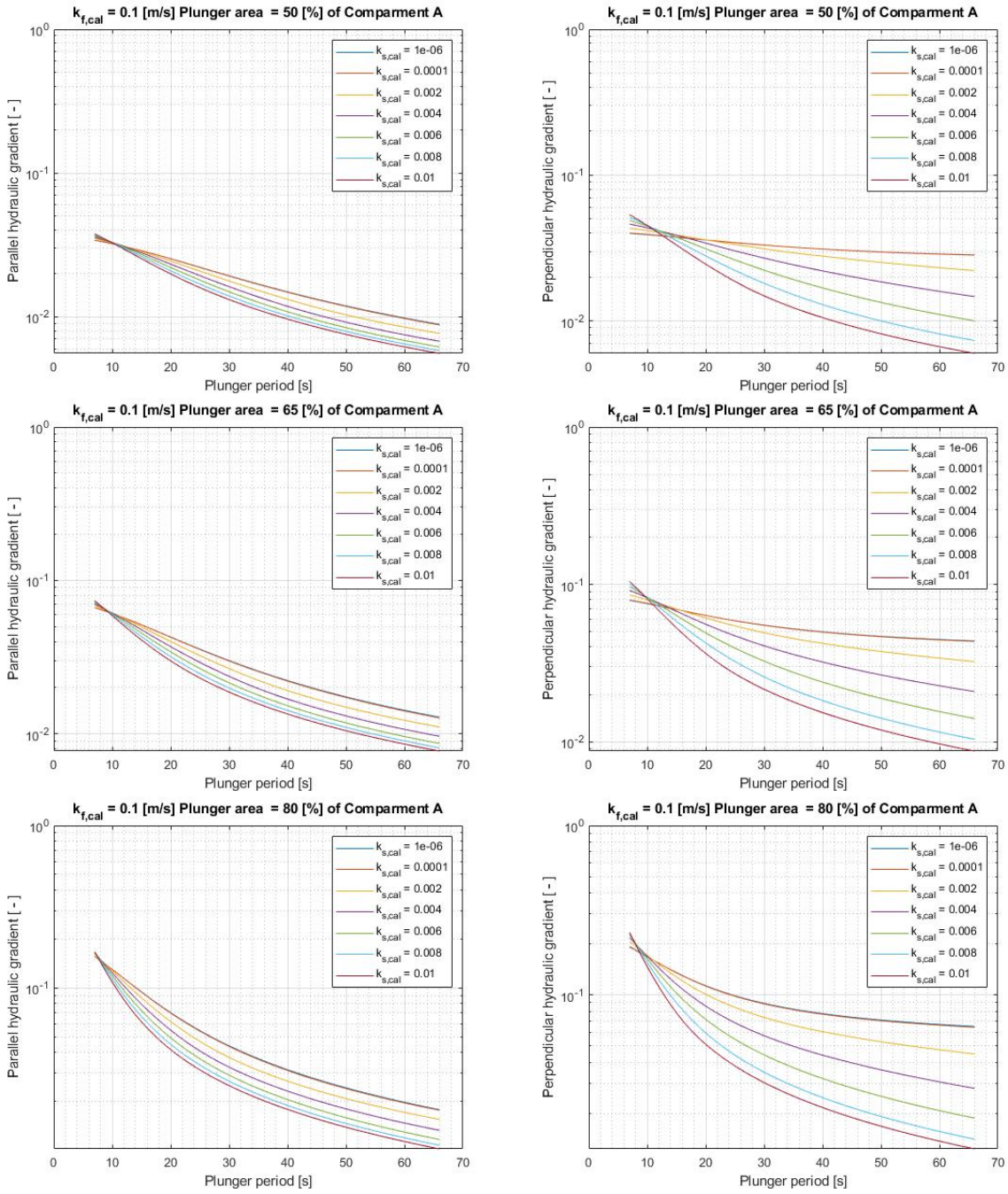

Figure 6.13: Design graphs of the combined configuration with a filter permeability of 0.1 [m/s].

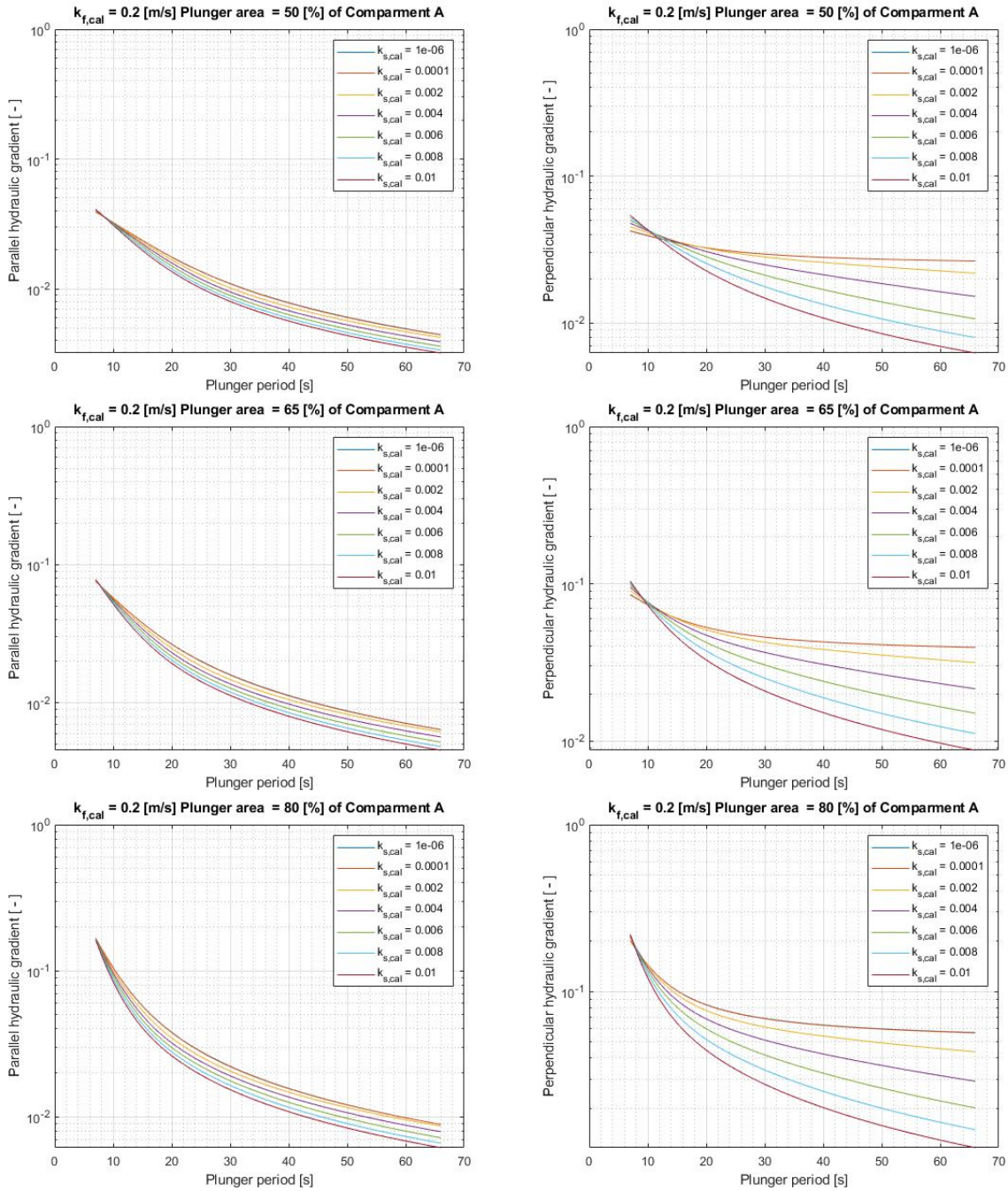

Figure 6.14: Design graphs of the combined configuration with a filter permeability of 0.2 [m/s].

7

Discussion, conclusion and recommendations

In this chapter, the uncertainties and limitations of the approach and the progress of the research line are discussed, the final conclusions of the study are presented and recommendations for further research are proposed.

7.1. Discussion

In this paragraph, the uncertainties and limitations of this study are discussed whereafter the progress of the research line is treated.

7.1.1. Uncertainties

In this section, the main uncertainties are discussed and the uncertainties of minor influence are briefly listed in alphabetical order.

Main uncertainties

- **Closure of the top seal**
  A top seal was used in Compartment B to form a closed boundary. Despite that the seal was finished with a rubber edge and fastened to the model with glue clamps, full air-tightness was not achieved. Air could leak through small openings, especially near the division screen since the latter tended to bend outwards. This resulted in a flow that was not purely parallel. As discussed in Paragraph 4.3.3, the combined flow regime resulted in lower i_{cr}. Therefore, this uncertainty could have lead to an underestimation of the determined $i_{cr,\parallel}$.

- **Placement of the base layer**
  By installing the base layer on top of the filter layer, there was a significant difference in initial infall between doing this dry and wet. This could have affected the results achieved and should therefore be seen as a uncertainty of this study.

- **Point of erosion**
  The i_{cr} was linked to the moment in which the first erosion was visible in the bottom cells. However, little is known about how the erosion evolves afterwards, an important item in designing and constructing the structure in reality. For example, if a structure reaches a new equilibrium after the first erosion, a design based on the i_{cr}-definition of this study could be overdimensioned. On the other side, if the i_{cr} is a type of tipping point – resulting in continuous erosion after the fist erosion began – a design based on the i_{cr}-definition of this study could be risky.

Uncertainties of minor influence

- **External influences**
  External influenced like vibration and temperature differences in the Hydraulic Laboratory could have influenced the experiments.
- **Instrument calibration inaccuracies**
  Visual measurement inaccuracies could have influenced the calibration of instruments.
- **Settling of pressure sensors during a test**
  This could have lead to slightly inconstant measurements during a single test.

7.1.2. Limitations

The limitations of the physical model test are split up into limitations of the physical and numerical models used and the limitations compared to the situation in reality.

Limitations of the model

- **Continuous measurement of erosion**
  An aim of this study was to measure the erosion continuously by the use of a watertight load cell. Unfortunately, this cell broke during testing and the erosion was fully measured optically.
- **Hydraulic gradient signal**
  It was aimed to induce the hydraulic gradient in such a way that the maximum value was kept constant for a period of time. However, due to limitations of the plunger amplitude and the model dimensions, this was not possible for the higher gradients. Therefore, the hydraulic gradient forced in a certain segment was determined to be the average of the maximum values per period of the smoothened signal. The smoothened signal neglected gradient peaks as a results of waves created by the plunger in Compartment A.
- **Maximum of forced hydraulic gradient**
  The maximum hydraulic gradients induced by the model was restricted by the plunger, limiting the knowledge gathering to a specific range of the critical hydraulic gradients for lower stability ratios.
- **Number of sensors**
  A limited number of sensors could be used in the set-up because of a shortage of data acquisition modules and instrument amplifiers. Because of this shortage, is was not possible to place a grid of pressure sensors in the base layer during a combined test. Therefore, the perpendicular flow pattern is not analyzed.
- **Numerical model**
  The porous flow in the numerical model was determined laminar. This was a simplification and neglects the turbulent and inertia terms for the upper segment of hydraulic gradients. Besides, the model assumed that the parallel flow was constant over the height of the filter layer and that the perpendicular flow was constant over the width of Compartment B. This flow pattern could differ to the pattern in the physical model.

Limitations of applying the physical model to reality

- **Filter inclination**
  A rubble mound sand retaining structure has a slope in an order of magnitude of 2:3. The filter studied is leveled horizontally resulting in a more symmetrical flow pattern.
- **Flow pattern**
  The flow in the model was forced symmetrically parallel or combined. In a breakwater, flow patterns are rather unpredictable. Therefore, an asymmetrical pattern with a dominant direction is evident.
- **Longshore current**
  In reality, waves attack the breakwater under an angle. Oblique waves result in lower hydraulic gradients compared to perpendicular incoming waves since the penetration length increases. Besides, the oblique waves induce a longshore current. Furthermore, currents are induced by e.g. tides. A current could influence the stability of the filter by strengthening or breaking the arching effect, dependent on the current direction.

- **Storm duration**
  During the physical model test, the duration of test segments with different plunger velocities was kept equal. This means that more waves were induced in the segments with higher plunger velocities. The influence of the number of waves was not studied.

- **Superimposed load**
  The load on the inversed filter structure imposed by the own weight of the reclamation could positively affect the stability of the filter. A new model was designed and constructed to determine this influence. Unfortunately, the construction of the model took a significant period of time, making it unable to study the influence of the superimposed load in this report.

7.1.3. Progression of the research line

This study was part of a master thesis research line. A reflection to the other studies is given in this paragraph.

- **Tutein Nolthenius (2018)**
  The first master thesis of this research line was written by Tutein Nolthenius (2018). During that study, the shortening of a geotextile was investigated for the same type of breakwater. The absence of a filter resulted in infiltration of the base material into the breakwater core forming a new interface. It was investigated which stability ratio resulted in a stable situation in the breakwater core. Higher gradients were expected since the longitudinal distance to the new interface was shortened. A stability ratio of approximately 8 showed promising results, however, only one test was performed. In that study, knowledge of the stability ratios versus critical hydraulic gradients was broadened.

- **Van de Ven (2019)**
  The second study focused on the possibility to create a stable boundary between a breakwater core and a land reclamation by the use of a single granular geometrically open filter layer. Numerical modeling was done to estimate hydraulic gradients occurring in a breakwater and physical model tests were conducted to determine critical hydraulic gradients for multiple stability ratios. Multiple recommendations of Van de Ven (2019) were included in this study. Most of the stability ratios tested in the parallel configuration in this study were stable compared to the numerical gradients determined by Van de Ven (2019) in OpenFOAM. All perpendicular gradient components were unstable. Furthermore, the critical gradients determined in this study were higher compared to the gradients determined by the physical modeling of Van de Ven (2019).

7.2. Conclusion

This thesis focused on broadening the knowledge of inversed geometrically open granular filter structures and provided a new physical model to the research line in order to study the influence of a superimposed load and the inclined filter shape in the near future. The main question asked was to what extent an inversed geometrically open granular filter layer capable is to preventing erosion of a land reclamation in rubble mound sand retaining structures. To answer this question, various sub-questions were formulated.

7.2.1. The influence of the stability ratio on the critical hydraulic gradient

The sub-question evaluated in this section is about the influence of the stability ratio (SR) of the inversed geometrically open granular filter structure on the critical hydraulic gradient.

The influence of SR, defined as the sieve diameter for which 15% of the mass of the filter material is smaller divided by the sieve diameter for which 85% of the mass of the base material is smaller $\left(\frac{d_{15,f}}{d_{85,b}}\right)$, was studied by the use of physical modeling. The model of Van de Ven (2019) was improved by (1) increasing the height of the bottom cells to make for the load cell, which unfortunately broke down, (2) adding custom made floaters to measure the water level fluctuations in the outer compartments and (3) fastening the pressure sensors to a custom made bar. Parallel and combined load conditions were tested. For both tests, the SR influenced the i_{cr} in an inversely proportional manner.

Furthermore, a new phenomenon influencing the i_{cr} was observed during this study, which was not included in the research line yet. This was the influence of the initial sand saturation of the filter layer lowering the determined i_{cr}. For the unsaturated parallel configuration, stability ratios of SR = 5.7, 6.7, 12.9 and 13.1

were tested in order to find a critical hydraulic gradient (i_{cr}) causing erosion. Results were found for the upper two values. For the lower *SR*, no erosion was detected resulting in a bottom limit of i_{cr}. The partly saturated parallel tests resulted in reduced i_{cr} up to a minimum of 73%. This could been caused by (1) the erosion detected was initial infall or (2) the initial saturation lowered the i_{cr} of the total filter structure by e.g. reducing the arching effect and inducing tunneling effects. The results of the parallel tests are given in Figure 7.4.

Three unsaturated combined tests were conducted with $SR = 6.7$ and 12.9. Erosion was detected twice for SR = 12.9, once in the first test segment – resulting in an upper limit for (i_{cr}) – and once in the second test segment. No erosion was visible for the $SR = 6.7$ test. The results of the combined tests are given in Figure 7.4 and 7.5.

7.2.2. The influence of the characteristic grain size of the base material

The sub-question evaluated in this section is about the influence of the characteristic grain size of the base material on the critical hydraulic gradient if a constant ratio between the characteristic grain sizes of the filter and base material is taken, as proposed by De Graauw et al. (1983) for classic open granular filters. This topic was studied by testing two groups with an approximately equal stability ratio but consisting of different granular materials. For the group $SR = 6 - 7$, not many conclusions could be drawn since no erosion was detected. The other group was:

$$SR = \frac{d_{15,b}}{d_{85,f}} = \frac{3.29}{0.25} = 13.1, \qquad i_{\parallel,cr} = 0.057$$

$$SR = \frac{d_{15,b}}{d_{85,f}} = \frac{7.95}{0.62} = 12.9, \qquad i_{\parallel,cr} = 0.051$$

The found i_{cr} for the filter structure with the largest base material was slightly lower compared to the filter with smaller base material. However, Figure 7.4 shows that the range bars overlap. Therefore, it was concluded that the grain size of the base material did not (significantly) influence the critical hydraulic gradient if a constant stability ratio was taken.

7.2.3. Comparison of the parallel and the combined load condition

The sub-question evaluated in this section is about the differences between the parallel and the combined load conditions. To compare the two set-ups that were tested in this study, the parallel component of the combined tests are plotted with the parallel tests and the results of Van de Ven (2019) in Figure 7.4. Visible is that the critical parallel hydraulic gradients of the combined tests are significantly lower (about 93%) compared to the parallel tests for $SR = 12.9$. This could be due to (1) the difference in flow pattern between the two configurations and (2) to the way the combined model was installed, leading to more initial infall.

Furthermore, the critical gradients determined in this study were put into perspective by comparing them to the 2% highest gradients occurring in a breakwater, determined in OpenFOAM by Van de Ven (2019), given in Figure 7.1 and 7.2. For the parallel hydraulic gradient, all parallel tests and the combined Test 12 form a stable system. Test 10 and 11 could be stable, depending on the depth of the filter. For the perpendicular component of the hydraulic gradient, no stable system was found.

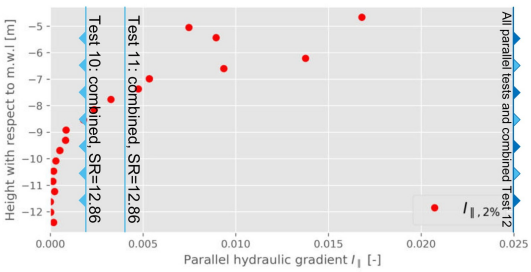

Figure 7.1: The critical parallel hydraulic gradients of the parallel tests (dark blue) and the parallel component of critical gradient the combined tests (light blue), determined in this study compared to the gradient occurring in a breakwater, estimated by Van de Ven (2019) in OpenFOAM.

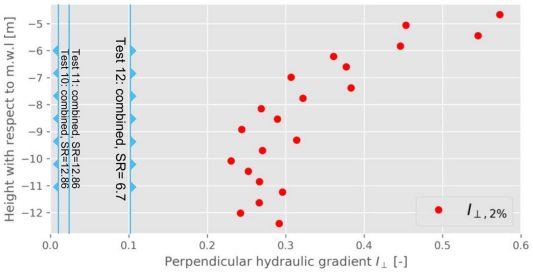

Figure 7.2: The perpendicular component of the critical parallel hydraulic gradients determined by the combined tests in this study compared to the gradient occurring in a breakwater, estimated by Van de Ven (2019) in OpenFOAM.

7.2.4. The new physical model

The sub-question evaluated in this section is about the possibility to test the influence of the superimposed load, resulting from the own weight of the reclamation, on the stability of an inversed geometrically open granular filter layer.

A new model has been designed to perform inversed granular filter tests under a superimposed load to mimic the own weight of the backfill. The possibility of performing inclined filter tests was included in the design. The model was constructed at DEMO. Besides, a newly developed numerical model has been made to plot design graphs for this new model. The model is shown in Figure 7.3.

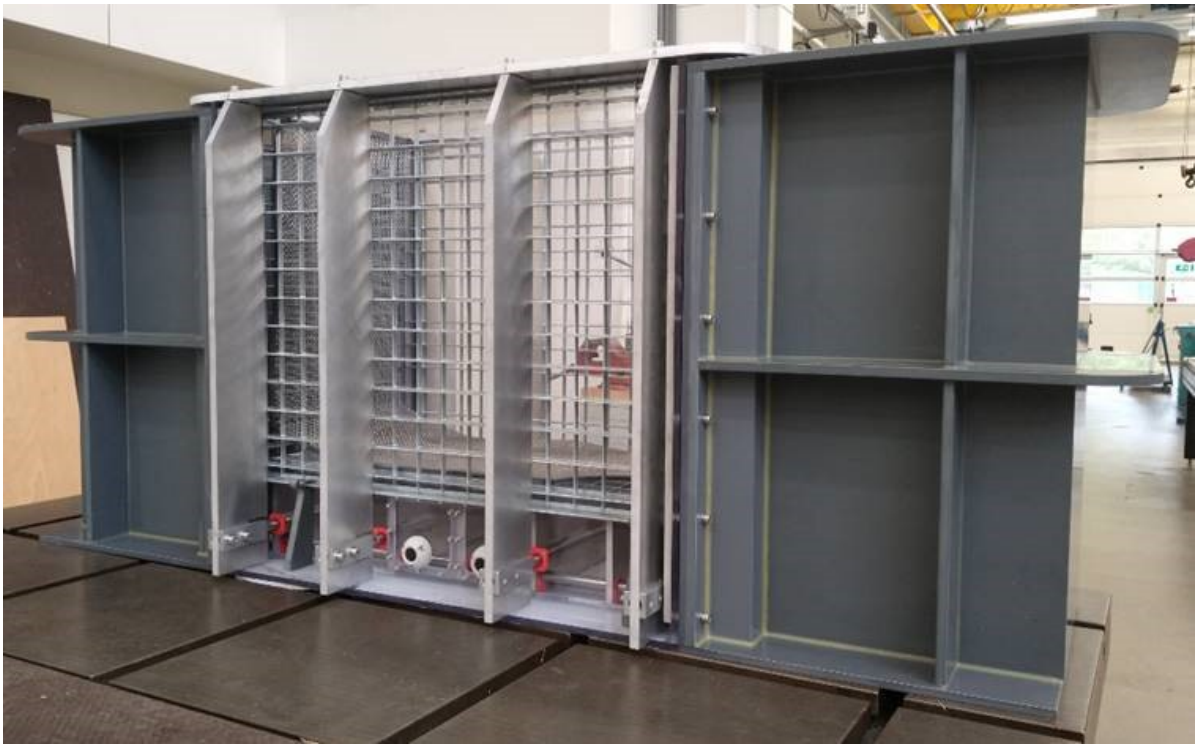

Figure 7.3: The new physical model for superimposed load and inclined filter tests.

7.2.5. Conclusion to the main research question

The main question of this study was to what extent an inversed geometrically open granular filter layer capable is of preventing erosion in a rubble mound sand retaining structure. First of all, in line with the study by Van de Ven (2019), it was possible to create an inversed open granular filter layer that prevents erosion of a land reclamation. Moreover, it was concluded that the filter structure was even more stable than Van de Ven (2019) concluded. To which extent this stability was, depended on both the load exerted on the filter layer and the filter layer itself. The load is mainly controlled by the local wave climate and the capability of the rubble mound breakwater to reduce the porous flow over the longitudinal axis. Based on the filters studied in this study, decreasing the stability ratio has a positive influence on the stability of the filter. No significant results had been found to conclude that the characteristic grain size of the base material influences the critical hydraulic gradient.

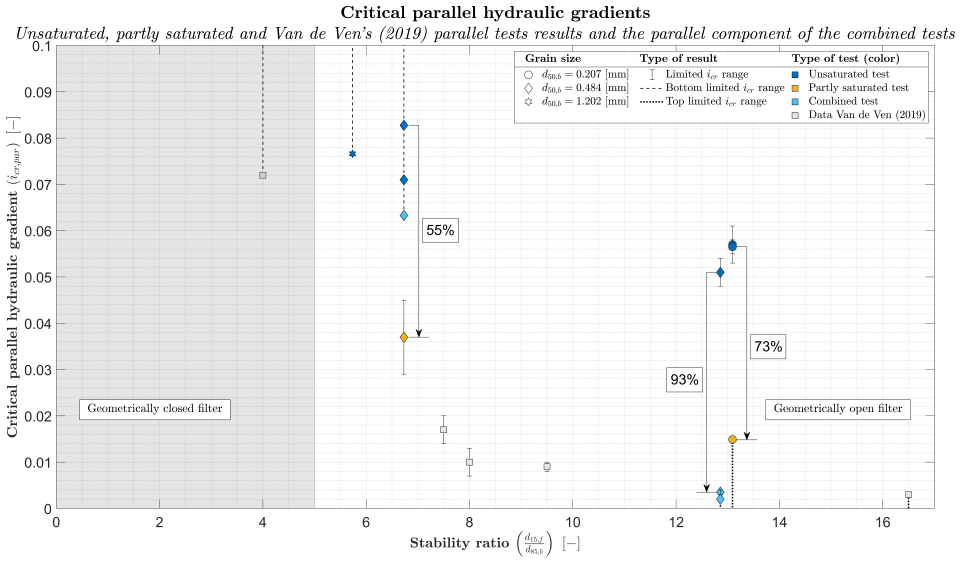

Figure 7.4: The results of the unsaturated and partly saturated parallel tests are plotted with the parallel component of the combined test results and the parallel test results of Van de Ven (2019).

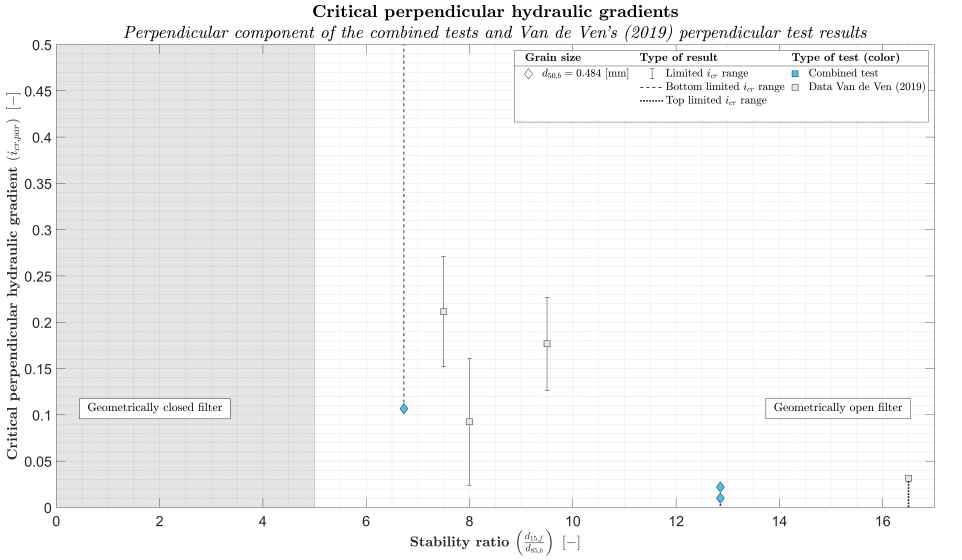

Figure 7.5: The perpendicular component of the combined test results are plotted together with the perpendicular test results of Van de Ven (2019).

7.3. Recommendations

A next step has been taken in the study on inversed open granular filter structures, a type of filter with economical and constructional benefits compared to granular closed filters and geotextiles. Since the results were promising but limited, recommendations are proposed for further research. Firstly, suggestions to broaden the knowledge on the topic are discussed. Secondly, suggestion to improve the results of the physical model are listed.

7.3.1. Broadening the knowledge

The following recommendations are made for further research to broaden the knowledge of an inversed granular open filter:

- **New model**
  The main recommendation of this study is to use the new model. The influence of the superimposed load and an inclined filter shape are the new aspects that could be studied in this model. Moreover, since the new model is larger compared to the physical model used in this study, the assumption that no scaling laws were applicable because the model is a cut-out of the real structure, could be examined. The topics investigated and recommended in this study could also be tested in the new model.

- **Sand saturation of the filter layer**
  During this study, it was observed that the initial saturation of the filter layer influenced the critical hydraulic gradient determined in the test. Projecting this effect into reality could have a significant influence on the stability of a structure. Therefore, it is recommended to investigate this phenomenon thoroughly.

  The lowering of the found i_{cr} could have been due to (1) that the erosion detected in the bottom cells, strictly consisted of sand grains that were initially present in the filter layer and had a lower critical gradient to erode into the bottom cells compared to sand originating from the base layer, by for instance arching of the base layer and differences in packing, or (2) that the sand present in the filter layer reduced the critical hydraulic gradient for the total inversed granular filter structure by forming channels for the base material to erode. This statements could be examined by:

  1. A test with a known volume of sand mixed into the filter layer. One could gradually increase the hydraulic gradient until erosion is present whereafter the gradient is kept constant until the erosion ends. By comparing the volume of sand in the bottom cells at the end of the test with the known sand volume initially present in the filter layer, statement (1) could be examined.
  2. An unsaturated test in which the plunger period is decreased until erosion is visible. Now the filter layer is partially saturated, one could increase the plunger period again, resulting in a lower hydraulic gradient. If the erosion continues, one could conclude that the critical hydraulic gradient for a saturated filter is smaller compared to an unsaturated filter.

- **Wet placement**
  A possible explanation of the difference between the parallel and combined results is the way the base layer was installed. Wet placement of the base layer on top of the filter layer could have resulted in lower critical hydraulic gradients compared to dry placement. Moreover, the wet placement could be more realistic to the reality. It is advised to perform tests to determine the influence of the wet placement.

- **Permeability granular material**
  It is recommended to determine the permeability of the granular material used during physical modeling, by for instance the permeability test given in Appendix A.1. Based on known permeabilities, a more solid numerical model calibration is reached.

- **Flow pattern through the model**
  The pattern of the porous flow in the combined configuration was quite uncertain and could be a reason for the difference in results between the parallel and the combined tests. By placing multiple pairs of pressure sensors in the base layer, one could determine how the hydraulic gradient evolves over the length of Compartment B. Furthermore, it is recommended to conduct a test with dye in the water, to observe the flowpattern through the filter layer visually.

- **Stability ratio**
  By testing various stability ratios, a more comprehensive relationship between the ratio and the critical hydraulic gradient could be determined.

- **Characteristic grain size base layer**
  To increase the knowledge on the effect of the characteristic grain size of the base material on the critical hydraulic gradient, it is recommended to perform more tests with constant stability ratios, for various stability ratios.

- **Filter layer thickness**
  In this study, it seemed that the filter layer thickness did not influence the i_{cr} determined. However, it is advised to investigate this topic more thoroughly. Furthermore, a thinner filter layer results in higher induced hydraulic gradients and provides less room for initial saturation.

- **Analysis of the arching effect**
  The arching effect is seen as one of the main stabilizing factors of the inversed filter. However, this phenomena is not studied in this research line yet. It is advised to analyze the deformation patterns of the base layer in the model tests. This could be done by for instance using the Particle Image Velocimetry (PIV) technique or Digital Image Correlation (DIC) technique.

- **Storm duration**
  The number of periods could influence the results. Furthermore, the erosion could stop after a while. It is recommended to look into the influence of the number of waves on the erosion.

7.3.2. Improving the model results

The following recommendations are made to improve the physical model results:

- **Increasing the forced hydraulic gradient**
  It is recommended to increase the hydraulic gradient forced by the plunger. This could be done by various measures, for example:

  - Adjust model dimensions;
  - Increase the velocity of the plunger;
  - Increase the dimensions of the plunger;
  - Decrease the filter height.

- **Bottom mesh grid**
  As discussed in Paragraph 5.6, the bends in the double mesh grids placed on top of the bottom cells, probably increased the filter permeability. It is advised to use a single mesh grid and to check whether the grid is flat placed on the of the bottom cells.

- **Continuous measurement of erosion**
  In this study, it was tried to measure the erosion continuously by the use of a load cell. Even though this failed, it is still recommended. This could be done for instance by the use of a proper load cell or an instrument that measures suspended sediments. Moreover, the erosion could be quantified and different stages of erosion could be analyzed.

- **Improvement of visibility**
  Unfortunately, a single webcam was available during model testing. The use of multiple cameras minimizes blind-spots, especially at the back of the model.

- **Pressure sensors fixed to model**
  The use of bars to fix the distance between the pressure sensors used in the base and filter layer greatly improved the consistency of the determined hydraulic gradients. Further improvement could be realized by fixing the location of the bars with respect to the model. This will obstruct the pressures sensors to move during a test and assures that the pressure sensors are located equally over various tests.

- **Pressure sensors in base layer**
  It is recommended to place pressure sensors in the base layer for every test, including the parallel test. Based on the output of these sensors, it could be checked if the configuration was strictly parallel or that any type of leakage was present at the top seal.

- **Top seal**
  The rubbers of the top seal were renewed before the first test. However, air could leak through small openings, especially along the division screens. Improvement of the top seal is recommended.

- **Plunger**
  To induce a constant hydraulic gradient, not only for the lower values, but also for the higher ones, it is recommended to modify the plunger in order to increase the amplitude.

Nomenclature

Acronyms

KC	Keulegan-Carpenter number	[−]
Re	Reynolds number	[−]
SAR	Soil arching ratio	[−]
SR	Stability ratio	[−]

Greek Symbols

α	Non-dimensional coefficient in coefficient a (Forchheimer equation)	[−]
β	Non-dimensional coefficient in coefficient b (Forchheimer equation)	[−]
γ	Non-dimensional coefficient in coefficient c (extended Forchheimer equation)	[−]
γ_w	Volumetric weight of water	[kN/m^3]
κ	Intrinsic permeability	[m^2]
ν	Kinematic viscousity	[kg/ms]
ϕ	Angle of repose	[−]
Ψ	Shields parameter	[−]
ρ_s	Density of the soil	[kg/m^3]
ρ_w	Density of the water	[kg/m^3]
σ_v	Average vertical pressure acting on the trapdoor	[Pa]

Latin Symbols

A	Area	[m^2]
a	Coefficient in Forchheimer equation	[s/m]
b	Coefficient in Forchheimer euation	[s^2/m^2]
c	Coefficient in extended Forchheimer equation	[s^2/m]
d	Grain size	[m]
d_n	Nominal grain size	[m]
F_s	Shape factor	[–]
g	Gravitational acceleration	[m/s^2]
H	Height of soil mass above the trapdoor	[m]
h	Waterdepth	[h]
i	Hydraulic gradient	[i]
k	Permeability in porous flow	[m/s]

L	Length over which the pressure drop is taking place	[m]
n	Porosity of the soil	[−]
Q	Discharge	[m^3/s]
q	Specific discharge	[m^2/s]
q_s	Superimposed load on the surface	[Pa]
R	Hydraulic radius	[m]
T	Period of oscilation	[s]
u_f	Filter velocity	[m/s]
u_{*cr}	Critical Shear Velocity	[m/s]
u_*	Shear Velocity	[m/s]
V	Amplitude of flow velocity oscilation	[m/s]
W	Grain weight	[kg]
V_P	Volume of pores	[m^3]
V_T	Total volume of soil	[m^3]

Bibliography

Ali Ahmadi and Ehsan Seyedi Hosseininia. An experimental investigation on stable arch formation in cohesionless granular materials using developed trapdoor test. *Powder Technology*, 330:137–146, 2018. ISSN 1873328X. doi: 10.1016/j.powtec.2018.02.011. URL https://doi.org/10.1016/j.powtec.2018.02.011.

Mahdi Al-Naddaf, Jie Han, Chao Xu, Saif Jawad, and Ghaith Abdulrasool. Experimental Investigation of Soil Arching Mobilization and Degradation under Localized Surface Loading. *Journal of Geotechnical and Geoenvironmental Engineering*, 145(12):1–17, 2019. ISSN 10900241. doi: 10.1061/(ASCE)GT.1943-5606.0002190.

K. J. Bakker, H. J. Verheij, and M. B. de Groot. Design Relationship for Filters in Bed Protection. *Journal of Hydraulic Engineering*, 120(9):1082–1088, 1994.

CBS. Bevolkingsontwikkeling; regio per maand, 2020. URL https://opendata.cbs.nl/statline/{#}/CBS/nl/dataset/37230ned/table?ts=1593504946174.

Chee Nan Chen, Wen Yen Huang, and Cheng Tsung Tseng. Stress Redistribution and Ground Arch Development During Tunneling. *Tunnelling and Underground Space Technology*, 26(1):228–235, 2011. ISSN 08867798. doi: 10.1016/j.tust.2010.06.012. URL http://dx.doi.org/10.1016/j.tust.2010.06.012.

B. Chevalier, G. Combe, and P. Villard. Experimental and Discrete Element Modeling Studies of the Trapdoor Problem: Influence of the Macro-mechanical Frictional Parameters. *Acta Geotechnica*, 7(1):15–39, 2012. ISSN 18611125. doi: 10.1007/s11440-011-0152-5.

Soon Hoe Chew, Hai Tian, Siew Ann Tan, and G. P. Karunaratne. Erosion Stability of Punctured Geotextile Filters Subjected to Cyclic Wave Loadings - A Laboratory Study. *Geotextiles and Geomembranes*, 21(4):221–239, 2003. ISSN 02661144. doi: 10.1016/S0266-1144(03)00027-X.

CUR. *The Rock Manual. The use of rock in hydraulic engineering*. 2007. ISBN 0860176835.

CUR. Interface Stability of Granular Filter Structures. *Report 233*, 2010.

A.F. De Graauw, T. Van der Meulen, and M.R. Van der Goes de Bye. Granular Filters: Design Criteria. *Journal of Waterway, Port, Coastal and Ocean Engineering*, 110(1):80–96, 1983.

H. den Adel. Re-analysis of permeability measurements using Forchheimer's equation. *Report C0-272550/56, Delft Geotechnics*, 1987.

F. Engelund. On the laminar and turbulent flow of ground water through homogeneous sand. *Trans. Danish academy of Technical sciences*, Vol. 3, 1953.

G. Enstad. On the Theory of Arching in Mass Flow Hoppers. *Chemical Engineering Science*, 30:1273–1283, 1975. ISSN 00092509. doi: 10.1016/0009-2509(75)85051-2.

Sabri Ergun. Fluid flow through packed columns. *Chemical Engineering Progress*, 1952.

P. Forchheimer. Wasserbewegung durch Boden (Water movement through soil). Translated by Parker D. Trask. *Zeitschrift des Vereines Deutscher Ingenieure*, 1901.

George F.W. Hauck. Structural Design of the Pont du Gard. *Journal of Structural Engineering*, 112(1):105–120, 1986.

Michael H Heibaum. Geotechnical Filters - the Important Link in Scour Protection. *2nd International Conference on Scour and Erosion*, (February):13–28, 2004. URL http://vzb.baw.de/publikationen/tc213/0/key2.pdf.

O Jenck, G Combe, F Emeriault, and A de Pasquale. Arching Effect in a Granular Soil Subjected to Monotonic or Cyclic Loading: Kinematic Analysis. *8th International Conference on Physical Modelling in Geotechnics*, 2(January):1243–1249, 2014.

T. C. Kenney and D. Lau. Internal stability of granular filters. *Canadian Geotechnical Journal*, 1985. ISSN 00083674. doi: 10.1139/t85-029.

M. Klein Breteler. Zandtransport in Granulaire Filters, Horizontale Stationaire Stroming (Dutch). *Delft Hydraulics Laboratory*, 1989.

M. Klein Breteler, H. den Adel, and M.A. Koenders. Taludbekledingen van Gezette Steen, Ontwerpregels voor het Filter. *Delft Hydraulics & Geo Delft*, 1992.

M.A. Koenders. Hydraulic criteria for filters. *Estuary physics*, 1985.

G.J. (Rijkswaterstaat Dienst Weg-en Waterbouwkunde) Laan. De relatie tussen vorm en gewicht van breuksteen. *Rapport MAW-R-81079*, 1981.

B.K. Low, S.K. Tang, and V. Choa. Arching in Piled Embankments. *Journal of Geortechnical Engineering*, 120 (11):1917–1938, 1995.

J.W. McNulty. An Experimental Study of Arching in Sand. Technical report, 1965.

K. H. Paik and R. Salgado. Estimation of Active Earth Pressure Against Rigid Retaining Walls Considering Arching Effects. *Geotechnique*, 53(7):643–653, 2003. ISSN 00168505. doi: 10.1680/geot.2003.53.7.643.

Andrea Polidoro, William Allsop, and Tim Pullen. Exploring the Need for Geotextile Filters for Rubble Bunds Retaining Sand-Fill Islands. In *Coastal Structures and Solutions to Coastal Disasters 2015: Resilient Coastal Communities - Proceedings of the Coastal Structures and Solutions to Coastal Disasters Joint Conference 2015*, 2015. ISBN 9780784480304. doi: 10.1061/9780784480304.080.

P. Ya. Polubarinova Kochina. Theory of Ground Water Movement. Translated from the Russian edition by J. M. Roger de Wiest. *Princeton University Press*, 1962. ISSN 0036-8075. doi: 10.1126/science.139.3557.820-a.

G .J. Schiereck and H.J. Verhagen. *Bed, bank and shore protection*. VSSD, Delft, second edition, 2012. ISBN 978-90-6562-306-5.

A. Shields. Application of Similarity Principles and Turbulende Research to Bed-Load Movement (Translated). *PreuSSischen Versuchsanstalt für Wasserbau*, 1936.

K. Terzaghi. *Theoretical Soil Mechanics*. 1943. doi: 10.1002/9780470172766.

K. Terzaghi and R. Peck. Soil Mechanics in Engineering Practice. Translated by Parker D. Trask. *The Journal of Geology*, 1948. ISSN 0022-1376. doi: 10.1086/625679.

R.C. Tutein Nolthenius. Sandfill-Retaining rubble mound structures. *Msc. Thesis, Delft University of Technology*, 2018.

D. P. Van de Ven. Granular Open Filter in Rubble Mound Sand Retaining Structures. *Msc. Thesis, Delft University of Technology*, 2019.

M. R.A. Van Gent. Stationary and Oscillatory Flow Through Coarse Porous Media. *Communications on Hydraulics, Delft University of Technology, Department of Civil Engineering*, 1993.

Henk Verheij, Gijs Hoffmans, Kees Dorst, and Stefan Vandesande. Interface Stability of Granular Filter Structures Under Currents. *Icse6*, (1):241–248, 2012.

A. Verruijt. *Grondmechanica*. Delft University Press, Delft, 5 edition, 1999. ISBN 90 407 1857 1.

Chao Xu, Xingya Zhang, Jie Han, and Yang Yang. Two-Dimensional Soil-Arching Behavior under Static and Cyclic Loading. *International Journal of Geomechanics*, 19(8):1–14, 2019. ISSN 15323641. doi: 10.1061/(ASCE)GM.1943-5622.0001482.

A

Literature

A.1. Permeability test

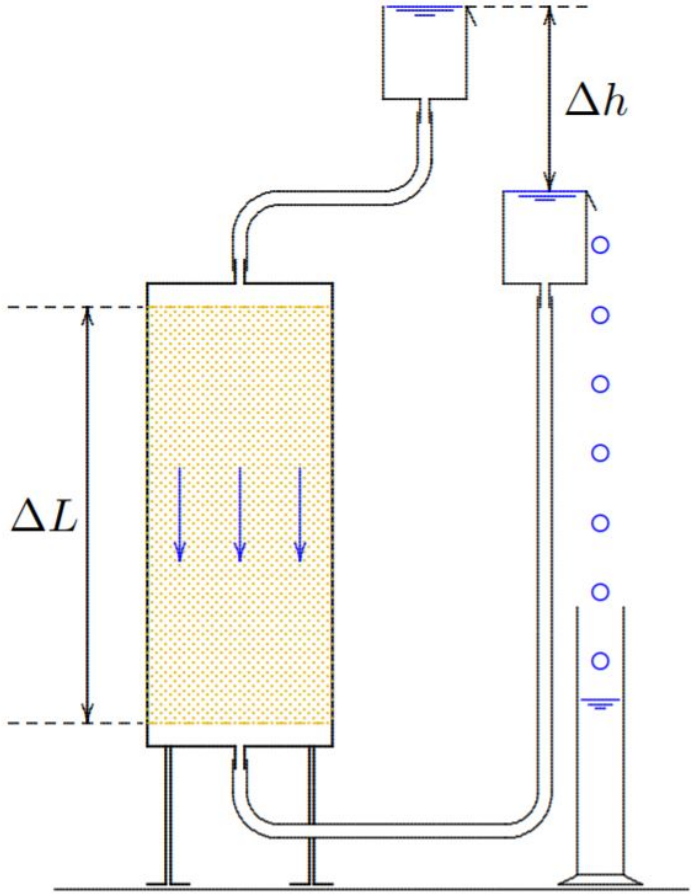

Figure A.1: Permeability test as performed by Darcy (Source: Verruijt (1999)).

A.2. Trapdoor test

To investigate the soil arching phenomenon, Terzaghi (1943) conducted the first trapdoor test to evaluate soil arching above a yielding support (the trapdoor). The principle of this test is simple. A volume of certain granular material is taken and placed in a box above a trapdoor. This trapdoor moves downward and lets the soil pour out after which a stable arch could be formed by the grains over the trapdoor which stops the discharge of soil. An example of a result of this test, executed by Ahmadi and Seyedi Hosseininia (2018) using gravel, is given in Figure A.2. Moreover, the trapdoor could be equipped with a load cell, to measure the load during lowering the trap door. McNulty (1965) used this trapdoor test to express the degree of soil arching by a Soil Arching Ratio (SAR):

$$SAR = \frac{\sigma_v}{\gamma H + q_s} \tag{A.1}$$

in which:

- σ_v: Average vertical pressure acting on the trapdoor [Pa]
- γ: Unit weight of the soil [N/m^3]
- H: Height of the soil mass above the trapdoor [m]
- q_s: Surcharge on the surface [Pa]

Whenever the arching ratio is equal to 1.0, no arching exists, and the actual distribution of pressure should be uniform. Arching is indicated by an arching ration of less than 1.0.

Chevalier et al. (2012) distinguished three phases in the response of material to the trapdoor test, all corresponding to a specific displacement of the trapdoor:

1. A *phase of maximal load transfer* during which the pressure on the trapdoor reaches a minimum value. This phase occurs as soon as the trapdoor moves downward from the initial position;
2. A *transitional phase* during which the pressure on the trapdoor increases with the trapdoor displacement;
3. A *critical phase* during which two vertical shear bands are observed starting at each edge of the trapdoor. During this phase, the pressure on the trapdoor increased continuously with the trapdoor displacement, but at a reduced rate.

Moreover, Chevalier et al. (2012) showed that the load transfer in the arch is a function of macro-mechanical frictional parameters of the soil, such as porosity, grading and particle shape. In line with this conclusion, Ahmadi and Seyedi Hosseininia (2018) found that the unit weight of the materials has much less effect on the soil arching in comparison with the frictional parameters.

Most of the trapdoor studies where carried out using the self weight of the soil or including a uniform static superimposed load. For instance, Al-Naddaf et al. (2019) did an experimental investigation of soil arching mobilization and degradation under localized surface pressure using a trapdoor test and a load cell on a footing. They concluded that localized surface loading degraded soil arching. In line with this conclusion, Xu et al. (2019) state that the application of surface loading caused degradation of soil arching, and cyclic loading had more effect on this degradation. Moreover, a thicker fill section had more resistance to surface loading in the degradation of soil arching. The latter conclusion could be beneficial for the filter situation considered in this thesis since the filter starts at a depth of 4 to 5 meters. However, the load in the study of Xu et al. (2019) is applied on top of the structure, and the load applied in the considered filter structure is on the sand-filter interface. Jenck et al. (2014) analyzed the influence of both monotonic and cyclic loads in a trapdoor-like test. In the monotonic situation, a motor is used to lower the trapdoor with a controlled velocity. A load cell is placed on top on this door to determine the arching effect. As can be seen from Figure A.3a, first the load reduces after which the load increases again but does not reach the initial value. The cyclic situation is created by pumping 320 liters of water into the model, where after emptying it. A complete cycle had a period of 1 hour. Concluded is that the arching effect is smaller after the first unloading (after water emptying), as shown in Figure A.3b.

(a) Trapdoor Test Box With Gravel.

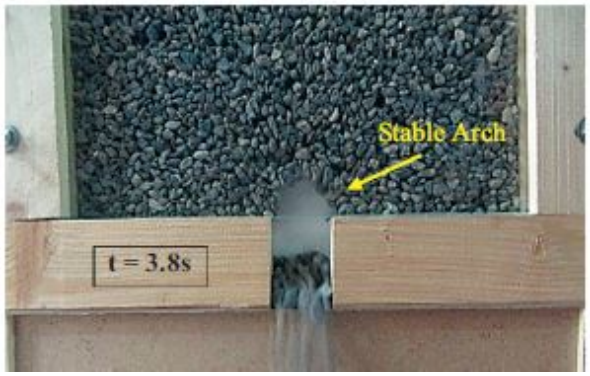

(b) Arch Formed After 3.8 Seconds, with $SAR = 1.0$.

Figure A.2: Trapdoor Test Performed by Ahmadi and Seyedi Hosseininia (2018).

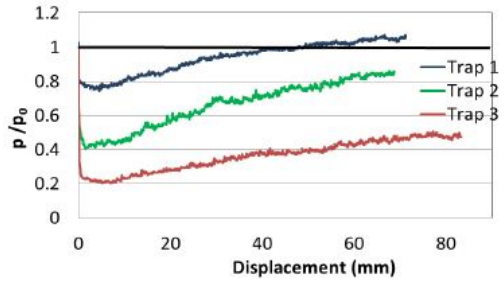

(a) Monotonic Situation, Stress on the Trapdoor Normalized by the Initial Stress. Trap 1: Granular Filter Thickness (h) = 0.1 [m], Trap 2: h = 0.2 [m] and Trap 3: h = 0.4 [m].

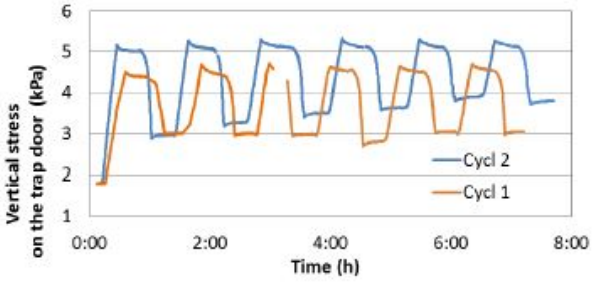

(b) Stress Results under Cyclic Load.

Figure A.3: Arching Effect in a Granular Soil Subjected to Monotonic and Cyclic Loading (Jenck et al., 2014).

B

Model description

B.1. Perpendicular configuration

In the perpendicular configuration, compartment C is disconnected from the model. This forces the flow through the filter and sand layer in compartment B and back. Because the permeability of sand is at least about two orders of magnitude lower than gravel, the hydraulic gradient in the sand layer is depicted as normative. The hydraulic gradient is measured in the sand layer by vertically aligned pressure sensors. The perpendicular configuration in illustrated in Figure B.1.

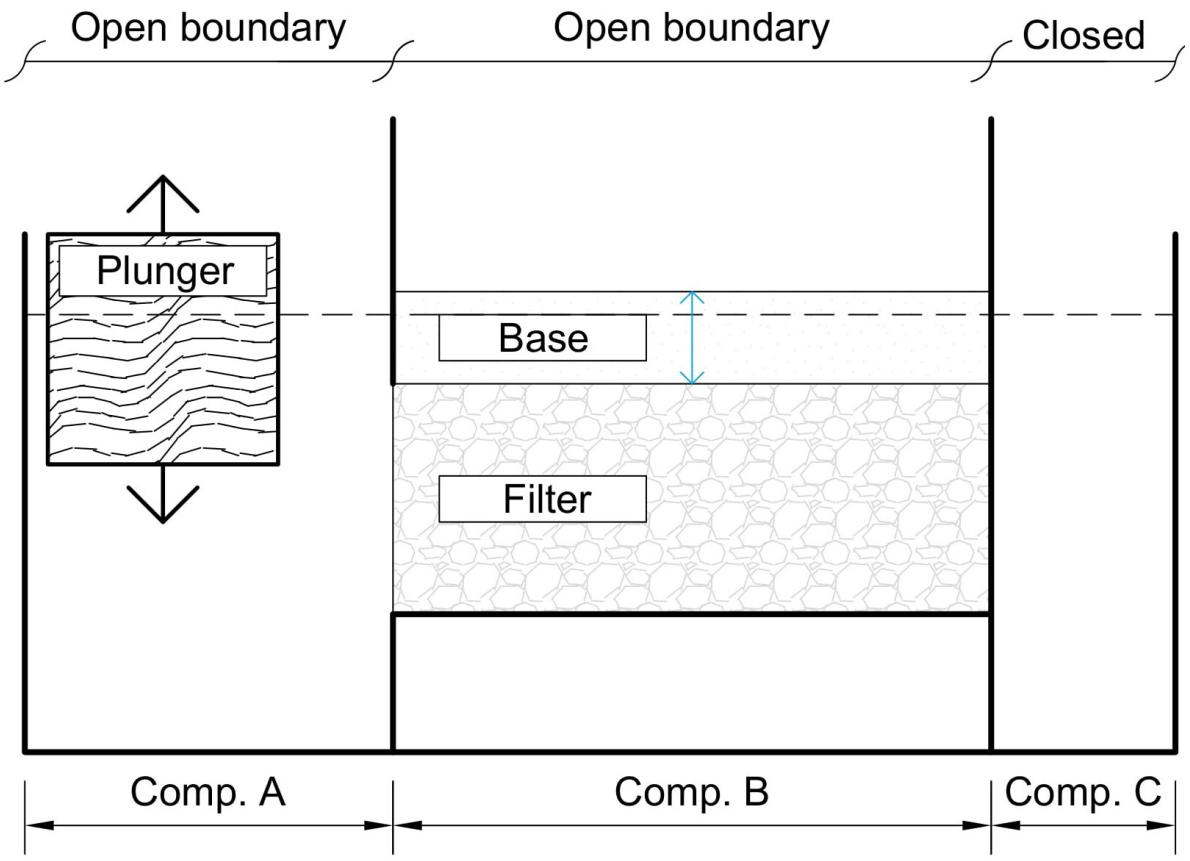

Figure B.1: Perpendicular configuration

B.2. List of parameters influencing the hydraulic gradient in the model

The model:

- Length of the compartments;
- Width of the model;
- Initial water level;
- Filter height;
- Height of the bottom cells;

Granular material:

- Permeability of the base and filter layer. On it turn dependent on:
  - Grain diameter
  - Sorting of the material
  - Porosity
  - Connection of the pores
- Porosity of the base layer, influences the ground water fluctuations in Compartment B;

Plunger:

- Plunger area;
- Plunger velocity;
- Plunger amplitude;
- Waiting time

B.3. Equipment

More information on the equipment used in the test set-up is given in this section.

B.3.1. Lasers

Three Micro-Epsilon lasers of the type optoNCDT 1302 (Figure B.2a) are used during the physical modeling. The sensor projects a modulated point of light onto the surface of interest. An optical element positioned at a certain angle to the optical axis of the laser beam receives the reflection of the light spot onto a high-sensitivity resolution element, dependent on the distance.

Range

The range of the three lasers is from 6 [mm] to 26 [mm].

Placement

One laser is attached to the stationary compartment above the plunger and projects the light point on top of the plunger, as shown in Figure 3.7a. This surface should be emerged at all time in order to achieve accurate output.

The other two lasers are attached to a self-designed floater, shown in Figure B.2b. This floater, consists of two base elements to keep the two vertical bars parallel aligned. Guided by these bars, a block of styrofoam floats on the water surface. A laser projects the light spot on top of the foam through an opening in the top base element hence the water level fluctuations are measured, as could be seen in Figure 3.7b.

Calibration
Because of the fixed position of the lasers, they are only calibrated once before the first test by plotting a regression line of the output versus the corresponding plunger position c.q. water levels.

As could be seen in Figure B.2c, the regression lines of the two lasers used on the floaters are more or less equal. The plunger laser has the same slope but is projected some centimeters higher than the other two. This is due to the face that the height of the plunger is measured from the bottom of the model to the bottom of the plunger, and the laser projects his light spot on top of the plunger. In other words, the height of the plunger is subtracted from the laser output signal.

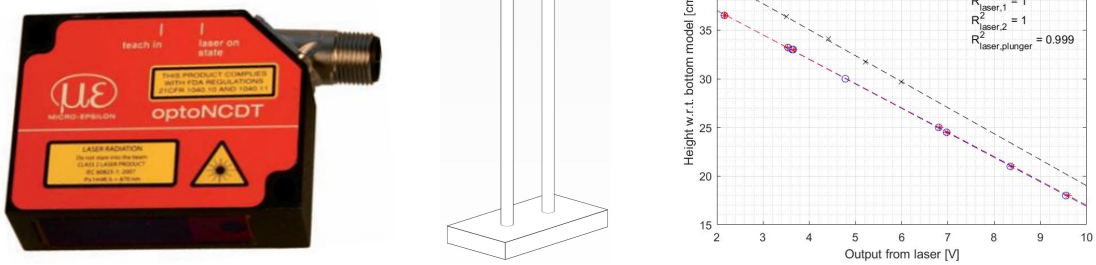

(a) A Micro-Epsilon optiNCDT 1302 laser. (b) Floater design. (c) Calibration of the lasers.

Figure B.2: Lasers used.

B.3.2. Differential pressure sensors

Adjustments
To make the sensors suitable for placement in the filter and base layer, some adjustments are made. Firstly, the left tube in Figure 3.8a is cut off, resulting in a surface with in the middle a little opening to the membrane. This part of the differential sensor will now be for the water pressure at the location of placement. To decrease the volume in this chamber in which air could be trapped and therefore could influence the output of the signal, the small opening is drilled into a funnel shape. Hereafter, a silicone hose is connected to the other tube of the sensor. This hose will be guide out of the model into the atmosphere. Lastly, the sensor is put into a PVC tube and filled with resin in order to make the sensor watertight. Figure 3.8b shows two differential pressure sensors suitable for underwater practice.

Range
The maximum pressure reading of this instrument is 0.5 [psi], which corresponds to a water column of about 35 [cm]. However, by screwing back the instrument amplifyer that is connected to the sensor, this range could be doubled to about 70 [cm].

Placement
The sensors are always placed in the way that the opening of the chamber that is connected to the water is facing downwards in order to reduce the influence of sand grains eroding downwards.

Calibration
Firstly, a test is done for every pressure sensor to determine if the sensor functions properly. In this calibration, the sensors are fixed in the model, using the rack shown in Figure 3.8c. The water level in this compartment is increased in a controlled manner (while measured by a laser as explained in the next subsection) and the corresponding output of the pressure sensor is noted. In Figure B.3a, the optical measured water levels

are compared with the laser output since the latter is more accurate. The linear regression line is used to adjust the optical measured water levels, which are in their turn plotted against all the available pressure sensor outputs in Figure B.3b. In this figure, the subscript matches the name or number of the particular sensor, one sensor had no number (denoted with NN). In every set-up, two sensors were calibrated simultaneously indicated by the same marker. Standing out from this figure is that PS_3 has the highest correlation. However PS_11 has the lowest R^2-value, the correlation is still almost perfectly linear. Moreover, while every pressure sensor's regression line is negative correlated and about parallel to another, PS_{104} is positively correlated. This is due to that the chambers of the sensor are connected vice versa compared the others.

Secondly, the pressure sensors are calibrated before and during each test, as described in Paragraph 3.2.3.

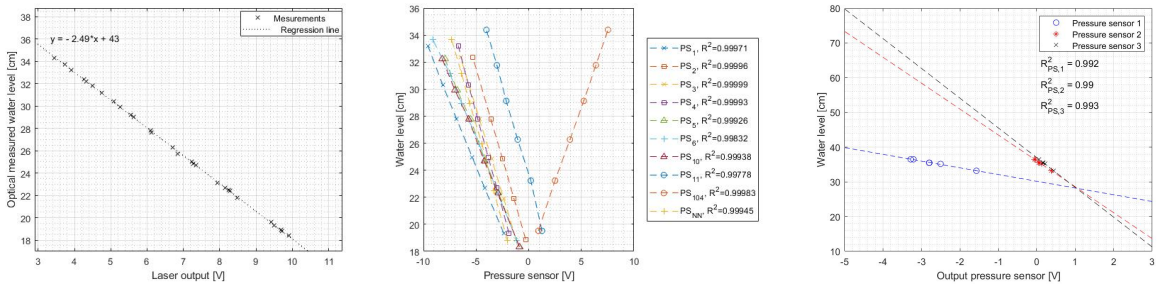

(a) Optical measured water level vs. laser output. (b) Pressure sensor output vs. water level. (c) Calibration of sensors in saturated soil.

Figure B.3: Calibration graphs pressure sensors.

B.3.3. Load cell

A double bending beam load cell of the type UTICELL model 190i is used during the tests (Figure B.4a). This cell is hermetically sealed and fully welded in order to use it in submerged settings. Because of the double bending, it should be prevented that the part of the bottom that is not mounted to the model touches the ground, and therefore influences the output of the device. A polyethylene stand is manufactured to avoid this. Moreover, a steel scale is manufactured. The bottom of the scale is inclined to reduces the possibility of air bubbles underneath it. Plain washers are used as spacer between the scale and the cell to avoid them to touch each other. A front view of the load cell and attributes is given in Figure B.4b, a bird view in Figure B.4c.

(a) UTICELL model 190i

(b) Load cell (front view).

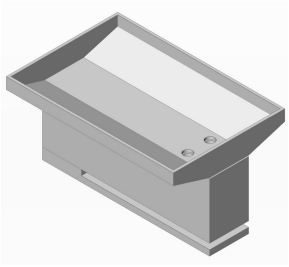

(c) Load cell (bird view).

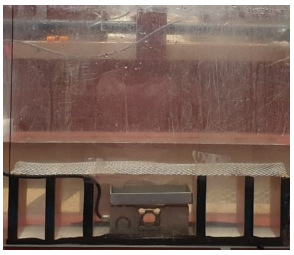

(d) Placement of the loadcell.

Function

The load cell is used in order to detect the starting point of the erosion of base material through the filter layer downwards by measuring continuously during the tests. At the beginning of a test, all the granular material rests on the mesh grid spanned horizontally above the bottom cells of the model. At the moment when erosion starts to occur, the base material falls through this mesh grid and is detected by the load cell. Later on, the output of the load cell will also be used in order to quantify the erosion over time.

Range

The capacity of the load cell is 15 [kg].

Placement

The load cell is place in the middle bottom cell of the model, see Figure B.4d. The cable of the cell is led along the back of the model behind the bubble plastic to reduce model effects.

Calibration

First of all, the load cell is calibrated in the emerged situation to determine if the cell performs as expected. This is done by adding objects on top of the scale with known masses and noting the output. The emerged calibration is shown by the red line in Figure B.5. Secondly, the submerged load cell is calibrated, the black line in the same figure. The blue line is a result of taking the relative density of the objects into account. One could see that the coefficient of determination (R^2) of the relative submerged line is almost 1 resulting in the conclusion that the load cell is useful for submerged measuring.

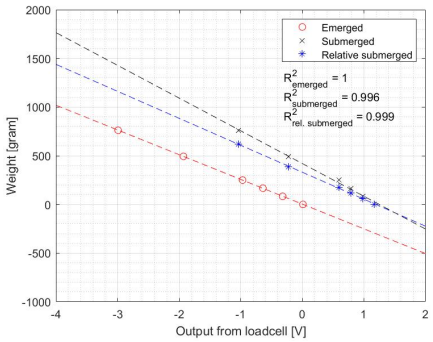

Figure B.5: Calibration of the loadcell.

B.4. Test protocol

(a) Cleaning the filter layer.

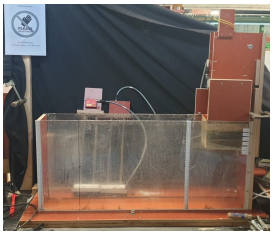

(b) Placement of the bottom cells, load cell and mesh grid.

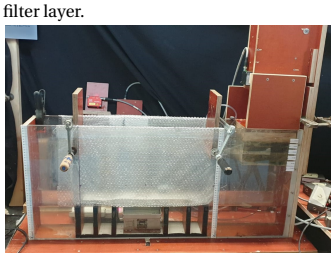

(c) Placement of bubble plastic.

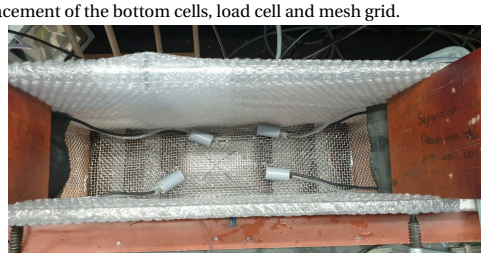

(d) Guiding the PS trough the division screens.

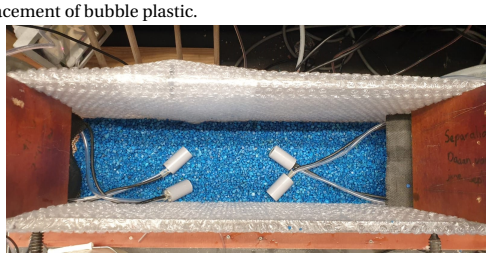

(e) Placement of half the filter layer.

(f) Mounting the PS to the bar.

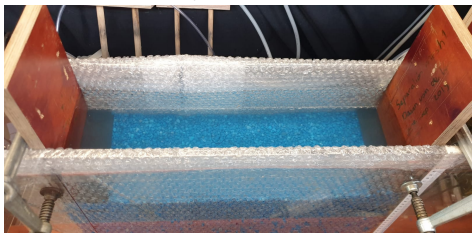

(g) Infill of water, calibrating PS and finishing filter.

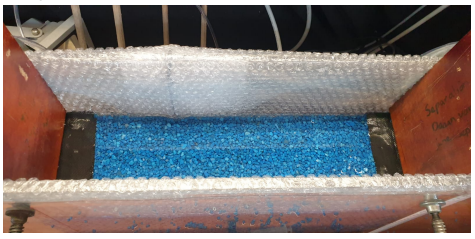

(h) Lowering water level to top filter layer.

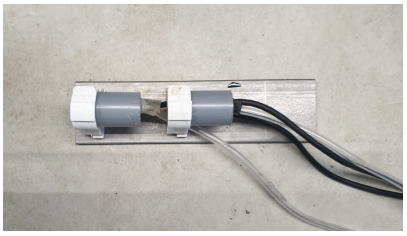

(i) Mounting the PS for the combined set-up.

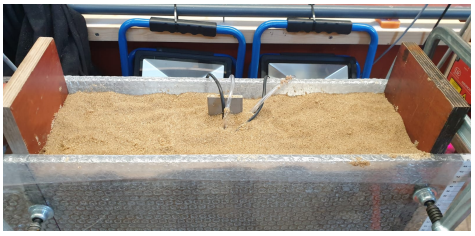

(j) Placement of the base layer and PS for combined set-up.

(k) Placement of the top seal for the parallel set-up.

Figure B.6: Setting up the physical model.

C

Porosity

In order to calibrate the numerical model, the porosity (n) of the gravel was determined. This was done for gravel 3, by the following steps:

1. A known volume of unsaturated (dry) gravel was weighted;
2. Water was added until the gravel was fully saturated;
3. The saturated gravel was weighted again.

The porosity is by definition the volume of the pores (V_p) over the total volume of the soil (V_t):

$$n = \frac{V_p}{V_t} \tag{C.1}$$

The porosity was determined thrice:

	Volume unsaturated soil [liter]	Weight unsaturated soil [kg]	Weight saturated soil [kg]	Volume pores [liter]	Porosity [-]
Test 1	8.5	14.6	18.6	4	0.47
Test 2	10	15.9	20.3	4.4	0.44
Test 3	11.5	17	22.2	5.2	0.45
				Average:	0.45

Table C.1: Porosity tests of gravel 3.

D

Concept design

D.1. Strength

This section is divided into thee different parts of the model:

1. Longitudinal walls, in other words the front and back of the model;
2. Transversal walls, in other words, the sides that separate compartment B from A and C;
3. Bottom.

D.1.1. Longitudinal Walls

A mesh grid is chosen to provide the strength in order to retain the horizontal stresses because it had two advantages. Firstly, a grid does not fully block the view on the granular material and even more important, the cells underneath it to observe erosion. Second of all, the grid is prefabricated and therefore the period of construction is expected to be shorter.

In order to limit the deflection of the grid and to give a beneficial support to the strength of the construction, vertical steel elements are used. Like the grid, blockage of the view, in the center of the model in particular, is unwanted. Therefore, it is chosen to construct two columns, dividing the center part in three equal areas with a width of 250 [mm].

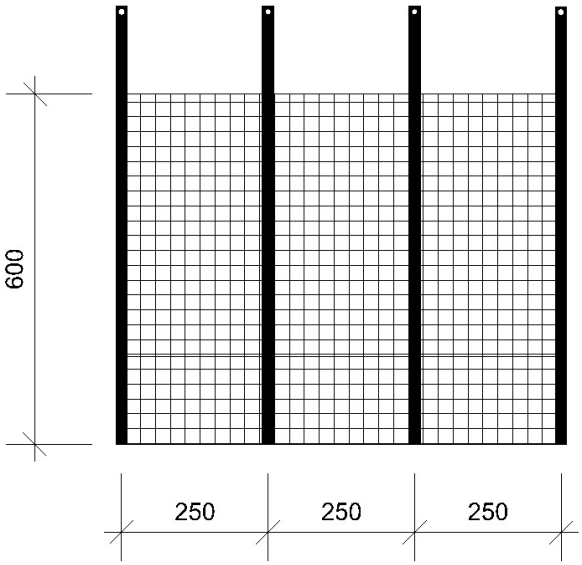

Figure D.1: Front View of the Longitudinal Wall.

Mesh Grid
The needed strength is:

$$\frac{176 \cdot 1000}{10} = \mathbf{17600\ [kg/m^2]}$$

Characteristics of mesh grids (source: Deja, manufacturer) are given below in Table D.1, the grids that satisfy are bold.

Mesh size [mm]	**Length grid [mm]**	**20 x 2**	**25 x 2**	**25 x 3**	**30 x 2**	**30 x 3**	**35 x 3**
33,33	200	13227					
	300	5879	9185	13778	13227	**19840**	**18003**
44,44	200	10317,06					
	300	4586	7164	10747	10317	15475	14042
50	200	9258,9					
	300	4115	6430	9645	9259	13888	12602

Table D.1: Strength of Mesh Grids.

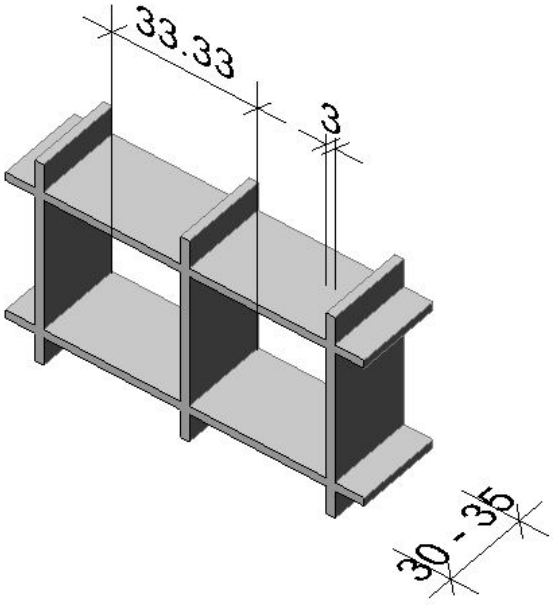

Figure D.2: Dimensions of a Mesh Grid.

When it is assumed that the lateral earth coefficient K_0 all ready included a safety number, a mesh size of 44.44 [mm] should be chosen to improve the viability.

Column
In order to limit the deflection of the mesh grid and to give beneficial support to the strength of the construction, vertical steel elements are used. A simplification of the loads exerting on such an element is shown in Figure D.3.

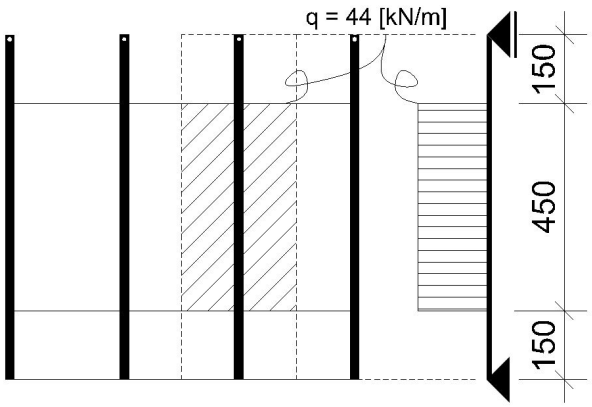

Figure D.3: Dimensions of a Mesh Grid.

1. q-load as point load (conservative):

$$w = \frac{1}{48}\frac{Fl^3}{EI} \tag{D.1}$$

- $q = 176 \cdot 0.25 = 44$ [kN/m]
- $F = q \cdot 0.45 \approx 20$ [kN]
- $E = 210$ [GPa]
- $w = 2$ [mm]

$$I = \frac{1}{48}\frac{Fl^3}{Ew} = \frac{1}{48}\frac{20 \cdot 10^3 \cdot 750^3}{210 \cdot 10^3 \cdot 2} = 4.2 \cdot 10^5 \text{ [mm}^4\text{]}$$

2. q-load over whole length column (optimistic):

$$w = \frac{5}{384}\frac{q_s l^4}{EI} \tag{D.2}$$

- $q = 176 \cdot 0.25 = 44$ [kN/m]
- $q_s = \frac{q \cdot 0.45}{0.75} \approx 26.5$ [kN/m]
- $E = 210$ [GPa]
- $w = 2$ [mm]

$$I = \frac{5}{384}\frac{q_s l^4}{Ew} = \frac{5}{384}\frac{26.5 \cdot 750^4}{210 \cdot 10^3 \cdot 2} = 2.6 \cdot 10^5 \text{ [mm}^4\text{]}$$

Example of rectangular profile:

- Width = 30 [mm]
- Height = 70 [mm]
- Thickness = 4 [mm]
- I = $4.21 \cdot 10^5$ [mm^4]

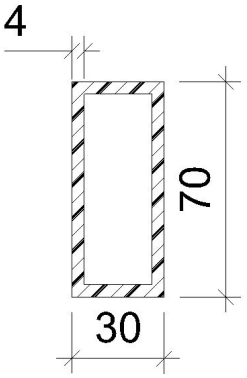

Bolts
Bolts are used to fix the columns to a cross beam. The tensile force is determined in form of a reaction force:

$$V = 0.5 \cdot q \cdot 0.45 = 9.9 \text{ [kN]} \tag{D.3}$$

An overview is given below in Figure D.4.

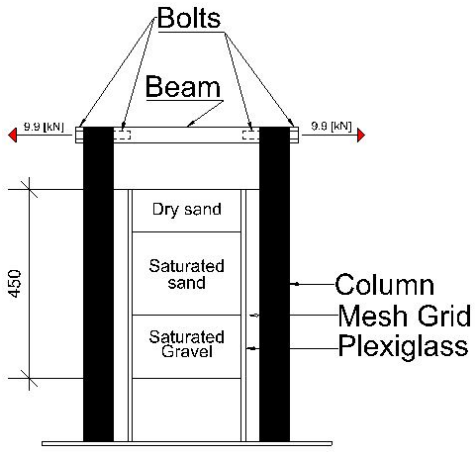

Figure D.4: Side View on Compartment B.

Bolt Type	Min. Yield Strength [N/mm2]	Min. Bolt Area [mm2]	Min. Bolt Radius [mm]
M8	640	15,47	7,0
M10	940	10,53	5,8
M12	1100	9,00	5,3

Table D.2: Bolts.

D.1.2. Transversal Walls

For the lower part of this wall, the same mesh grid in chosen, because water needs to be able to flow through this area. For the upper part, no visibility is needed and to a metal plate will satisfy. A cross beam is supporting the transition.

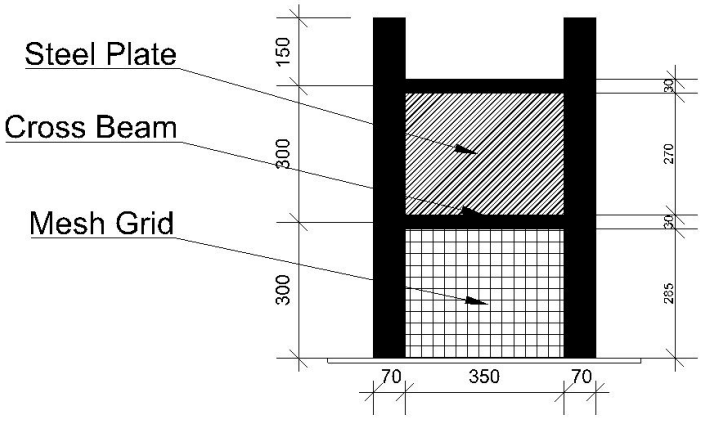

Figure D.5: Front View of the Transversal Wall.

Mesh Grid
The vertical span of the mesh grid is 300 [mm], just like the design span of the longitudinal grid. Therefore, the same grid could be used. However, gravel is not aloud to go through the mesh ($D_{50} \approx 10$ [mm]).

Cross Beam
The cross beam is the beam on the transition of the grid to the steel plate. A q-load over whole length. Assumed is that 150 [mm] above and under the bar rests on the cross beam.

$$w = \frac{5}{384}\frac{q_b l^4}{EI} \tag{D.4}$$

- $q_b = 176 \cdot 0.3 = 53$ [kN/m]
- $E = 210$ [GPa]
- $w = 2$ [mm]

$$I = \frac{5}{384}\frac{q_b l^4}{Ew} = \frac{5}{384}\frac{53 \cdot 350^4}{210 \cdot 10^3 \cdot 2} = 2.5 \cdot 10^4 \text{ [mm}^4\text{]}$$

Therefore, the same profile as for the longitudinal wall will satisfy. However, also a slimmer profile could be chosen.

Example of rectangular profile:

- Width = 20 [mm]
- Height = 40 [mm]
- Thickness = 2 [mm]
- I = $4.45 \cdot 10^4$ [mm^4]

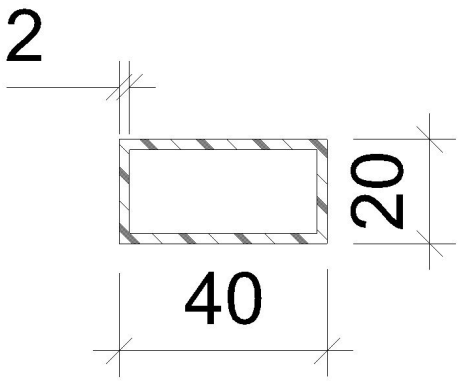

Steel Plate
The span of the steel plate is 350 x 300 [mm^2], so the same moment of inertia as the cross beam is valid.

Example of steel plate:

- Width = 350 [mm]
- Thickness = 10 [mm]
- I = $2.5 \cdot 10^4$ [mm^4]

However, in order for no water leakage, it could be wist to take the same width as the mesh grid.

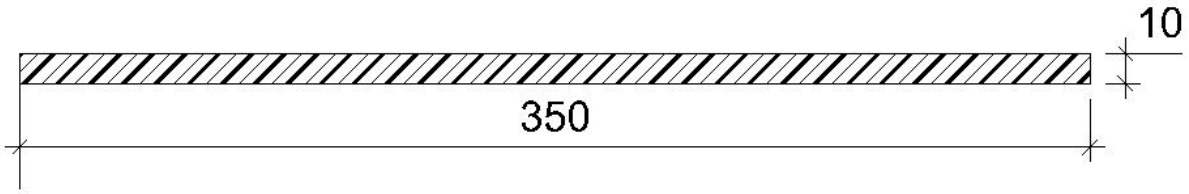

Figure D.6: Steel Plate.

Bolts
Bolts are used to fix the cross beam with the other one at the other end of compartment B. The tensile force is determined in form of a reaction force:

$$V = 0.5 \cdot q \cdot \frac{0.35}{2} = 0.5 \cdot 176 \cdot 0.6 \cdot 0.35 \cdot 0.5 = 9.24 \text{ [kN]} \tag{D.5}$$

Therefore, the same bolts as in the longitudinal wall could be used. However, it could also be chosen to weld the columns to the longitudinal mesh grids to form a solid construction.

Bolt Type	Min. Yield Strength [N/mm2]	Min. Bolt Area [mm2]	Min. Bolt Radius [mm]
M8	640	14,44	6,7
M10	940	9,83	5,6
M12	1100	8,40	5,1

Table D.3: Bolts.

D.1.3. Bottom
As a floor, a mesh grid should be used because it should be able to allow sand erode through it. Also the floor need to be removable for cleaning and other uses of the model. The strength the mesh grid needs is equal to the total vertical pressure: 250 [kPa]. There is no mesh grid in Table D.1 that is strong enough for this load. However the span will be about 150 [mm], which improves the strength of the mesh grid. Also the mesh size needs to be lower because no gravel (D_{50} = 10 [mm]) is aloud to pass the grid.

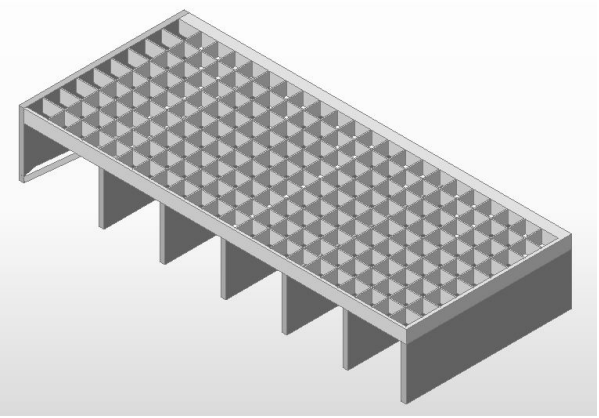

Figure D.7: Floor Grid Attached to Cell Walls.

Figure D.8: Side View. Floor Grid Attached to Cell Walls.

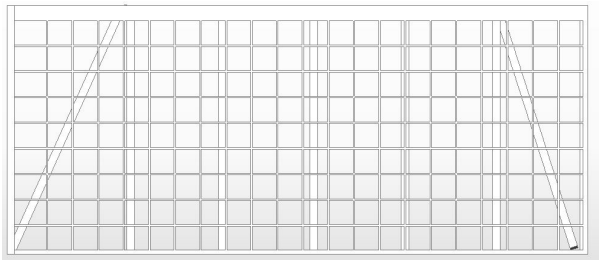

Figure D.9: Floor Grid Attached to Cell Walls.

D.2. Total Design

Also in CAD-file available.

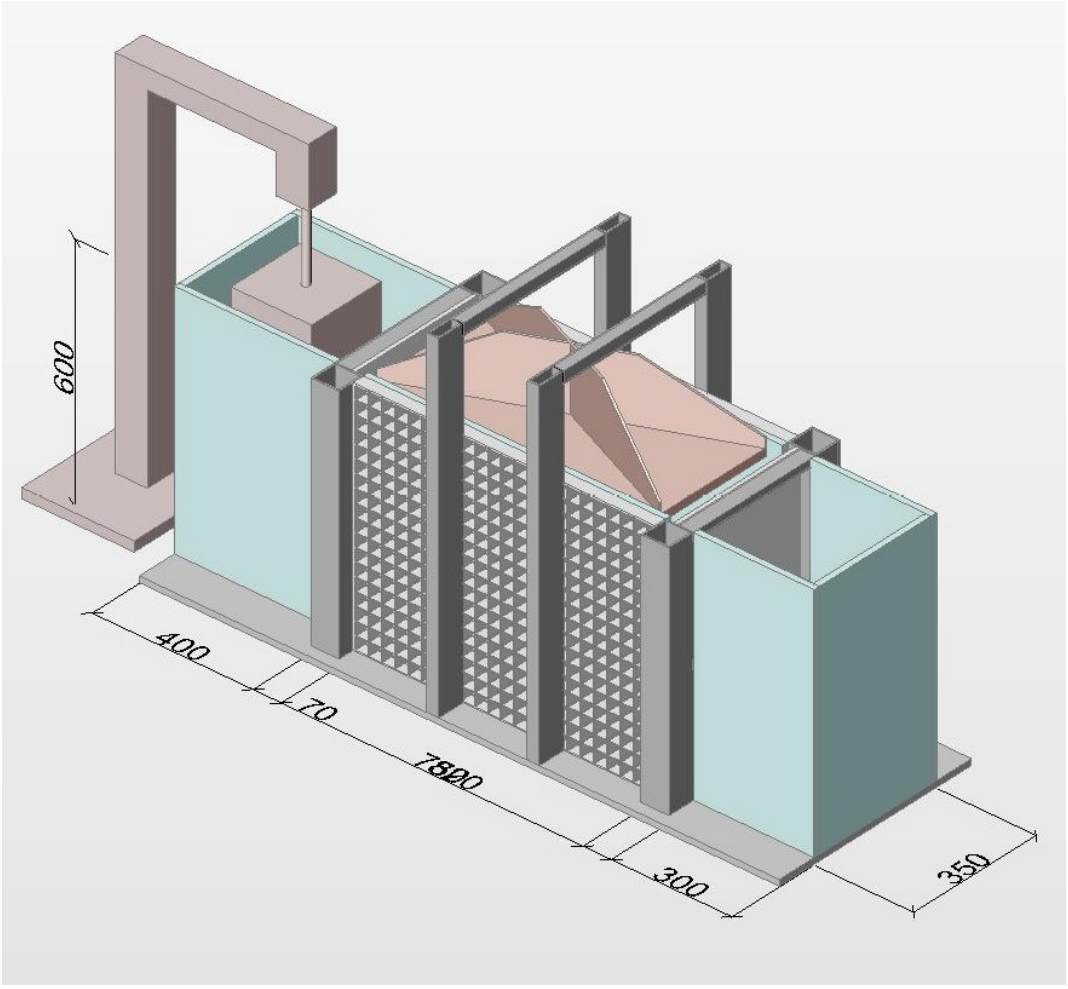

Figure D.10: Total Design.